Dissertation
submitted to the
Combined Faculties for the Natural Sciences and for Mathematics
of the Ruperto-Carola University of Heidelberg, Germany
for the degree of
Doctor of Natural Sciences

Put forward by

Jonathan Manuel Lommen, M. Sc.
Born in Konstanz
Oral examination: 19.12.2017

Probing the microscopic environment of physiological sodium ions through observation of the T_2^* relaxation

Referees: Prof. Dr. Peter Bachert
Prof. Dr. Lothar Schad

Untersuchung der mikroskopischen Umgebung physiologischer Natriumionen durch Beobachtung der T_2^*-Relaxation

Natrium (^{23}Na)-Ionen spielen eine entscheidende Rolle in der Gewebephysiologie und können aufgrund eines Kernspins von 3/2 mittels Magnetresonanztomographie (MRT) nichtinvasiv detektiert werden. Die Wechselwirkung des elektrischen Kern-Quadrupolmoments mit dem externen Feldgradienten bewirkt einen schnellen biexponentiellen Signalzerfall, welcher einen direkten Einblick in die mikroskopische Umgebung ermöglicht. Ziel dieser Arbeit war eine zeiteffiziente In-vivo-Messung der transversalen Relaxationszeiten $T_{2,\mathrm{s}}^*$ und $T_{2,\mathrm{l}}^*$. Dies wurde für Hirnparenchym durch Optimierung der zeitlichen Abtastung und einer neuartigen Hochfrequenzspule erreicht, was eine Steigerung des Signal-zu-Rauschverhältnisses von bis zu 145 % möglich machte. Mit dem optimierten Abtastmuster wurden die Relaxationszeiten in gesunder weißer Gehirnsubstanz zu $T_{2,\mathrm{s}}^*$ / $T_{2,\mathrm{l}}^*$ = 4,2 ± 0,4 ms / 34,4 ± 1,5 ms ermittelt. Im Vergleich zu einer linearen Abtastung konnte die mittlere Unsicherheit um bis zu 29 % reduziert werden. Monte-Carlo-Simulationen zeigten weiterhin eine Verminderung der mittleren Abweichung um 73 %. Ausgehend von den T_2^*-Werten konnte die mittlere Korrelationszeit der Wechselwirkung mit 39,3 ± 2,5 ns abgeschätzt werden.

Probing the microscopic environment of physiological sodium ions through observation of the T_2^* relaxation

Sodium (^{23}Na) ions play an essential role in the physiology of living tissue and can be observed non-invasively due to a nuclear spin of 3/2 via magnetic resonance imaging (MRI). The interaction of the electrical quadrupole moment of the nucleus and the external field gradient causes a rapid biexponential signal relaxation, which represents a direct probe into the microscopic environment. The aim of this thesis was to develop a time-efficient in vivo measurement of the apparent transverse relaxation times ($T_{2,\mathrm{s}}^*$, $T_{2,\mathrm{l}}^*$). This was realized for brain parenchyma by optimization of the temporal sampling and a novel radio frequency coil leading to an increase in signal-to-noise ratio of up to 145 %. With the optimized pattern relaxation times were determined in healthy human white matter to be $T_{2,\mathrm{s}}^*$ / $T_{2,\mathrm{l}}^*$ = 4.2 ± 0.4 ms / 34.4 ± 1.5 ms. Compared to linear sampling, up to 29 % reduction in mean uncertainty was achieved. Monte-Carlo simulations further demonstrated a 73 % decrease in bias. Based on the T_2^* values, the average correlation time of the interaction could be estimated at 39.3 ± 2.5 ns.

Contents

Abbreviations

AC	adaptive combination
CISS	constructive interference in steady state
CSF	cerebrospinal fluid
DA 3D-RAD	sampling-density-adapted 3D radial
FFT	fast Fourier transformation
FID	free induction decay
FOV	field of view
FSL	FMRIB software library
FT	Fourier transformation
GM	gray matter
GRE	gradient echo
^{1}H	hydrogen
HPC	high performance computing cluster
^{39}K	potassium
MPRAGE	magnetization prepared rapid acquisition gradient echo
^{23}Na	sodium
NLLS	non-linear least squares
NMR	nuclear magnetic resonance
nuFFT	non-uniform fast Fourier transformation
MRI	magnetic resonance imaging
PSF	point spread function
RAM	random access memory
RF	radio frequency

ROI	region of interest
SAR	specific absorption rate
SE	spin echo
SNR	signal-to-noise ratio
SOS	sum-of-squares
T_2	transverse relaxation time
T_2^*	apparent transverse relaxation time
$T_{2,\mathrm{l}}^*$	long relaxation time
$T_{2,\mathrm{s}}^*$	short relaxation time
TE	echo time
TE_{min}	minimal echo time
TR	repetition time
T_{RO}	readout time
UHF	ultra-high field
WM	white matter

1 Introduction

Sodium (^{23}Na) ions play an essential role in the physiology of living tissue. Due to a nuclear spin of 3/2, the ^{23}Na ion distribution can be observed non-invasively via magnetic resonance imaging (MRI), which has first been demonstrated in humans by Hilal et al. [1985] at 1.5 T. In biological tissue, the ^{23}Na concentration is precisely regulated by the ^{23}Na-^{39}K-ATPase ("sodium-potassium pump") and pathologies are often manifested in a local concentration change [Boada et al., 2005; Madelin and Regatte, 2013]. To this end, special effort has been put into quantitative mapping of the tissue ^{23}Na content (e.g. [Thulborn et al., 1999b; Lommen et al., 2016a]). Amongst other developments, dedicated acquisition strategies [Konstandin and Nagel, 2014] and higher magnetic field strength [Schepkin et al., 2014; Mirkes et al., 2015] increased the signal-to-noise ratio (SNR) efficiency and allowed ^{23}Na MRI to evolve into a growing tool for clinical research [Madelin and Regatte, 2013].

^{23}Na nuclei experience a strong interaction with local electric field gradients arising from the microscopic environment due to their electric quadrupole moment [Hubbard, 1970; Rooney and Springer, 1991b]. This interaction results in a rapid biexponential decay of the transverse magnetization in the order of a few milliseconds with a short component of $T_{2,\mathrm{s}}^{*} \approx 0.2\,\mathrm{ms}$ to 5.0 ms and a longer component of $T_{2,\mathrm{l}}^{*} \approx 10\,\mathrm{ms}$ to 64 ms (cf. **Table 2.3**). In the case of free ions, a monoexponential decay is observed ($T_2^{*} \approx 60\,\mathrm{ms}$) because the correlation time τ_c of the interaction is short compared to the Larmor frequency ($\omega_0 \tau_c \ll 1$). Right from the beginning, the rapid signal relaxation has been a challenge for ^{23}Na imaging. On the other hand, the strong interaction also provides potentially valuable information about the microscopic tissue structure. This might allow the extraction of additional physiological information which is not contained in concentration quantification or hydrogen (^{1}H) relaxation processes [Rooney and Springer, 1991b; Nagel et al., 2011]. The sensitivity of the ^{23}Na signal decay to motion restriction lead to the idea of separating the signal arising from the extracellular space from intracellular ions. Different approaches have been proposed such as multiple-quantum filtering [Boada et al., 2004; Tanase and Boada, 2005; Fleysher et al., 2010; Matthies et al., 2010], shift reagents [Winter and Bansal, 2001; Gupta and Gupta, 1982], or image contrasts with a weighting towards the intracellular space derived from multi-echo acquisitions [Qian et al., 2015; Stobbe and Beaulieu, 2005; Nagel et al., 2011; Benkhedah et al., 2013b; Madelin et al., 2014]. For a deeper understanding, precise knowledge of the ^{23}Na signal relaxation would be of high value.

1 Introduction

Due to a low tissue abundance in the millimolar range, the SNR of ^{23}Na MRI is by four orders of magnitude lower than the SNR of ^{1}H MRI. Therefore, first in vivo measurements of the apparent transverse relaxation T_2^* were performed by global sampling of the free induction decay (FID) [Nordenskiold et al., 1984; Cope, 1970]. The advances in SNR efficiency then allowed compartment-wise determination [Nagel et al., 2011] and finally spatially resolved maps were presented [Lu et al., 2011]. Nevertheless, the low signal still limits reliability as well as detailed analysis of the signal behavior. This is reflected in the wide variation of reported relaxation times.

The observation of the ^{23}Na signal relaxation faces a trade-off between two main challenges: low SNR and a fast biexponential signal decay in the range of the readout time ($T_{\mathrm{RO}} = 2\,\mathrm{ms}$ to $20\,\mathrm{ms}$ and mostly $T_{\mathrm{RO}}/T_{2,\mathrm{s}}^* \geq 1$). Consequently, the acquisition of sufficient information about the decay dynamics is challenging and often multiple repetitions of a multi-echo measurement are required. Due to the rapid signal decay, center-out FID sampling strategies are used [Boada et al., 1997; Gurney et al., 2006; Nagel et al., 2009]. In this case, the acquisition time of each echo can be shifted arbitrarily to a later time point, which might be useful to capture the specific shape of the signal decay. However, it renders the search for an optimal sample distribution more complicated.

For ^{1}H MRI, the quantification of the transverse relaxation time and dedicated temporal sampling schemes have been under extensive investigation [Poon and Henkelman, 1992; Jones et al., 1996; Anand et al., 2009; Uddin et al., 2013; Linnet and Teilum, 2016]. Acquisition schemes range from linear sampling to logarithmic patterns towards more sophisticated strategies as proposed by Jones et al. [1996]. The latter authors used the Cramér-Rao theory to analytically derive an optimal sampling scheme for a specific T_2 value. However, the transfer of these strategies to ^{23}Na MRI is limited by low SNR and the fast biexponential decay. Common approaches employing signal ratios [Haacke et al., 1999] can only be applied to the long component using late echo times [Fleysher et al., 2009]. Furthermore, conventional fast T_2 sampling schemes [Poon and Henkelman, 1992; Pell et al., 2006] are not applicable to ^{23}Na MRI due to high specific absorption rate (SAR) and increased echo spacings. Therefore, most studies focus on the apparent relaxation T_2^*.

The aim of this work was to establish a reliable in vivo measurement of the T_2^* decay of the ^{23}Na MRI signal. To this end, the sampling efficiency needed to be increased in order to achieve acceptable measurement durations. The main focus was put on the distribution of temporal sampling points which was optimized for the application in brain parenchyma.

2 Theory and background

In this chapter, the basic physical principles used in this work are described. First, nuclear magnetic resonance and the application to magnetic resonance imaging is discussed. Details of relaxation theory with focus on the electric quadrupole interaction are given and measurement methods for the transverse relaxation are described. Some background on image reconstruction from k-space data is provided as well.

2.1 Nuclear magnetic resonance

The phenomenon of nuclear magnetic resonance (NMR) occurs when atoms with a nuclear spin are brought into a magnetic field. This enables absorption and emission of a resonant radio frequency (RF) field. A short introduction will be given on the basis of Slichter [1989].

2.1.1 Zeeman interaction

The nucleus of an atom with spin $\hat{\boldsymbol{I}}$ exhibits a nuclear magnetic moment $\hat{\boldsymbol{\mu}}$. It is connected to the spin via the gyromagnetic ratio γ by

$$\hat{\boldsymbol{\mu}} = \gamma \hat{\boldsymbol{I}} \quad . \tag{2.1}$$

The gyromagnetic ratio is a constant specific to each nucleus. In this work, ^{1}H and ^{23}Na are of interest having values of $\gamma_{^1\mathrm{H}} = 42.58\,\mathrm{MHz/T}$ and $\gamma_{^{23}\mathrm{Na}} = 11.26\,\mathrm{MHz/T}$. The energy eigenvalues of the spin states $|s, m\rangle$ are

$$\hat{\boldsymbol{I}}^2 |s, m\rangle = I(I+1)\hbar^2 |s, m\rangle \quad \text{and} \tag{2.2}$$

$$\hat{I}_z |s, m\rangle = m\hbar |s, m\rangle \quad . \tag{2.3}$$

Here, m is the magnetic quantum number running from $m = [-I, -I+1, \ldots, I]$. If immersed in an external magnetic field $\boldsymbol{B}_0 = B_0 \boldsymbol{e}_z$ in z-direction, the magnetic interaction is described by the Zeeman Hamiltonian

$$\hat{H}_Z = -\hat{\boldsymbol{\mu}} \boldsymbol{B}_0 \quad , \tag{2.4}$$

which, when acting on the state $|s, m\rangle$, has the energy eigenvalues

$$E_m = -\gamma\hbar m B_0 \quad . \tag{2.5}$$

A splitting into $2I + 1$ equidistant energy levels is observed with a difference of

$$\Delta E = \gamma B_0 \hbar \quad . \tag{2.6}$$

2.1.2 Macroscopic magnetization

In a system containing a large number of atoms, a statistical analysis is more practical. The occupation number of a state m is given by

$$p_m = \frac{\mathrm{e}^{-E_m/k_B T}}{Z} = \frac{\mathrm{e}^{-\gamma\hbar m B_0/k_B T}}{Z} \quad , \tag{2.7}$$

with k_B being the Boltzmann constant and T the temperature. The the sum of states Z is defined by

$$Z = \sum_{m=-I}^{I} e^{-E_m/k_B T} \quad . \tag{2.8}$$

Applying the density matrix formalism with

$$\hat{\boldsymbol{\rho}} = \sum_m p_m \, |m\rangle \, \langle m| \tag{2.9}$$

the expectation value can be determined via the trace

$$\langle \hat{\boldsymbol{I}} \rangle = \mathrm{tr}\, \hat{\boldsymbol{\rho}} \hat{\boldsymbol{I}} \quad . \tag{2.10}$$

The macroscopic observable magnetization is the expectation value of the volume average over all atoms in the volume V

$$\langle \hat{\boldsymbol{M}} \rangle = \frac{1}{V} \sum_{i=1}^{N} \langle \hat{\boldsymbol{\mu}}_i \rangle = \frac{1}{V} \sum_{i=1}^{N} \gamma \, \langle \hat{\boldsymbol{I}}_i \rangle \quad . \tag{2.11}$$

Using the high temperature approximation ($E_m \ll k_b T$), this leads to

$$M_0 \approx \frac{N}{V} \frac{\gamma^2 \hbar^2 I(I+1)}{3 k_B T} B_0 \quad . \tag{2.12}$$

Thus, the macroscopic magnetization M_0 is proportional to the main field B_0 and the density of atoms in the volume V. Higher temperature T leads to a decrease in magnetization.

2.1.3 Equation of motion and radio frequency excitation

The temporal evolution of the magnetization can be determined with the von-Neumann equation

$$\frac{\mathrm{d}}{\mathrm{d}t}\langle\hat{\boldsymbol{\mu}}\rangle = \frac{i}{\hbar}\left[\hat{\boldsymbol{H}},\hat{\boldsymbol{\mu}}\right] \quad . \tag{2.13}$$

Applying the knwon commutator relations, this leads to

$$\frac{\mathrm{d}}{\mathrm{d}t}\boldsymbol{M} = \gamma\boldsymbol{M}\times\boldsymbol{B} \quad , \tag{2.14}$$

where classical vectors are used since these are macroscopic observables. In the general case, the magnetization precesses around the magnetic field $\boldsymbol{B}$ with the *Larmor frequency* $\omega_0 = \gamma B_0$. The transverse component $M_\perp$ can be observed by induction. In order to bring the magnetization from the equilibrium into the transverse plane, a resonant RF pulse $\boldsymbol{B}_1 = B_1\exp(-i\omega_{\mathrm{RF}}t)\boldsymbol{e}_x$ is irradiated. In a rotating frame with frequency ω_0, an effective field $\boldsymbol{B}_{\mathrm{eff}}$ is seen and Equation 2.14 is altered to

$$\frac{\mathrm{d}}{\mathrm{d}t}\boldsymbol{M} = \gamma\boldsymbol{M}\times\boldsymbol{B}_{\mathrm{eff}} = \gamma\boldsymbol{M}\times\begin{pmatrix} B_1 \\ 0 \\ B_0 - \frac{\omega_{\mathrm{RF}}}{\gamma}\end{pmatrix} \quad . \tag{2.15}$$

In case of a resonant pulse $\omega_{\mathrm{RF}} = \omega_0$, a rotation around the axis of B_1 occurs. The angle of rotation is dependent on the amplitude $B_1(t)$ and duration t_p of the pulse

$$\alpha = \gamma\int_{t=0}^{t_p} B_1(t)\mathrm{d}t \quad . \tag{2.16}$$

In this work, mostly rectangular pulses without temporal modulation are applied which leads to $\alpha = \gamma B_1 t_p$.

2.1.4 Relaxation of the NMR signal

The observed NMR signal represents an excited state, which decays over time due to different types of interactions of the nuclei with their environment. The time required to dissipate the excitation energy to the environment is described by the time constant T_1, termed *spin-lattice* relaxation time. However, the decay of the measured signal is not only due to T_1 but also the coherence of the whole spin system gradually decreases over time. This loss of phase coherence is characterized by the *spin-spin* relaxation time T_2. An empirical description of the dynamics of the magnetization is given by the Bloch equations [Bloch, 1946], which are in the rotating frame

$$\frac{\mathrm{d}\boldsymbol{M}}{\mathrm{d}t} = \begin{pmatrix} -\frac{1}{T_2} & 0 & 0 \\ 0 & -\frac{1}{T_2} & 0 \\ 0 & 0 & -\frac{1}{T_1}\end{pmatrix}\boldsymbol{M} + \begin{pmatrix} 0 \\ 0 \\ \frac{M_0}{T_1}\end{pmatrix} \quad . \tag{2.17}$$

When defining the transverse component of the magnetization $M_\perp = M_x + iM_y$ and a longitudinal part in the direction of the main field $M_\parallel = M_z$, the signal decay after a resonant RF excitation pulse at time t is described by

$$M_\perp(t) = M_0 \mathrm{e}^{-t/T_2} \quad \text{and} \tag{2.18}$$

$$M_\parallel(t) = M_0 - \left(M_0 - M_\parallel(0)\right) \mathrm{e}^{-t/T_1} \quad . \tag{2.19}$$

In practice, the observed transverse decay is shortened by dephasing caused by local static field inhomogeneities stemming e.g. from susceptibility changes between tissues. This apparent relaxation time T_2^* is connected to the true T_2 through

$$\frac{1}{T_2^*} = \frac{1}{T_2} + \frac{1}{T_2'} \quad . \tag{2.20}$$

The contribution from inhomogeneities of amplitude ΔB_0 can be approximated by a local off-resonance frequency $\Delta\omega = \gamma \Delta B_0 = 1/T_2'$. The apparent relaxation T_2^* is shown as function of the off-resonance frequency in **Figure 2.1**.
The signal relaxation is specific to the microscopic structure of the object under investigation. For medical imaging, the signal relaxation varies over tissues and is altered in pathologies. This allows to obtain the high soft tissue contrast of MRI. For ^{1}H MRI, the dominating relaxation path is the magnetic dipole-dipole interaction between neighboring nuclei due to their magnetic moment. The ^{23}Na NMR dynamics are dominated by a quadrupole interaction of the nucleus with the external electric field gradient as explained in more detail in the following.

Transition probability and spectral density

A description for the relaxation processes of more quantitative nature can be given using the theory developed by Bloembergen et al. [1948]. In case of a stationary perturbation, the expectation value of a transition due to an interaction, such as the dipole-dipole or electric quadrupole interaction, is given by the correlation function $G_{kl}(\tau_c)$. The correlation function is a measure of similarity between the interaction Hamiltonian $\hat{H}_{IA}$ at time t_0 and at time $t = t_0 + \tau_c$. The probability W_{kl} for a transition from state l to state k can then be formulated as

$$W_{kl} = \frac{1}{\hbar^2} \int_{-\infty}^{+\infty} G_{kl} \mathrm{e}^{-i(k-l)\tau} \mathrm{d}\tau \quad . \tag{2.21}$$

The time τ_c is the *correlation time* and describes the average time scale of the interaction. Thus, for two uncorrelated states $G_{kl} = 0$ at all τ_c. Due to diffusion and other processes, nuclei in an NMR experiment exhibit some sort of motion which can be characterized by τ_c.

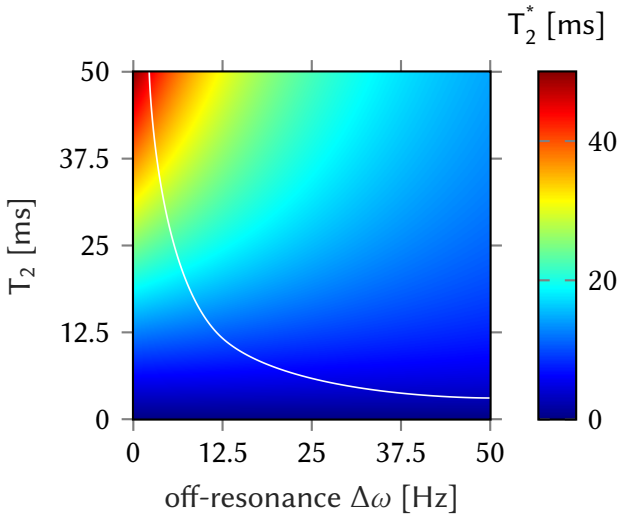

Figure 2.1: Apparent relaxation T_2^* as function of T_2 and off-resonance frequency $\Delta\omega$. The white line indicates a 10 % deviation between T_2 and T_2^*. For higher relaxation times, the relative impact of off-resonances is stronger than for shorter T_2.

In Equation 2.21, the integral resembles a Fourier transform of the correlation function. It is of practical use, to define the *spectral density*

$$J_{kl}(\omega) = \int_{-\infty}^{+\infty} G_{kl}(\tau) \mathrm{e}^{-i\omega\tau} \mathrm{d}\tau \quad , \tag{2.22}$$

which then allows to express the transition probability by

$$W_{kl} = \frac{J_{kl}(k-l)}{\hbar^2} \quad . \tag{2.23}$$

Since the J_{kl} give the probability of the interaction to happen at frequency ω, it is a measure of how likely a transition at this frequency is to happen. Thus, signal relaxation is a function of the amplitude of the spectral density at the resonance $\omega = \omega_0$. If an exponential decay of the correlation function is assumed, the spectral density is given by

$$J(\omega) = \frac{\tau_c}{1 + (\omega\tau_c)^2} \quad . \tag{2.24}$$

From the transition probability, the relaxation constants T_1 and T_2 can be estimated. For the simple case of isotropic liquids they are

$$\frac{1}{T_1} = K\left[J(\omega_0) + 4J(2\omega_0)\right] \quad \text{and} \tag{2.25}$$

$$\frac{1}{T_2} = \frac{K}{2}\left[3J(0) + 5J(\omega_0) + 2J(2\omega_0)\right] \quad . \tag{2.26}$$

The constant K is the coupling constant of the dipole-dipole interaction and $J(0) = \tau_c$. In **Figure 2.2**, the shape of the spectral density for an exponential correlation function is shown for three values of τ_c and the relaxation times following from Equation 2.26 as function of the τ_c. Applying the Bloemberg-Purcell-Pound theory to 3/2 nuclei allows understanding their decay behavior as will be described in the next section.

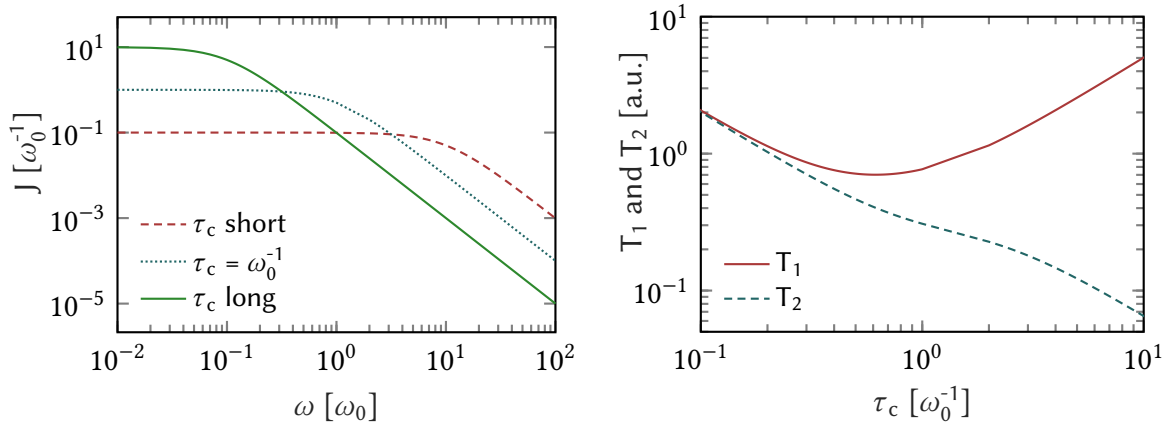

Figure 2.2: Spectral density J and relaxation times T_1 and T_2 for varying correlation times τ_c. The correlation times shown left correspond to the upper and lower limit of the right figure. The spectral density is highest at $\tau_c\omega_0 \approx 1$ and lowest T_1 relaxation is found for τ_c in this range. The T_2 relaxation gradually declines for increasing τ_c. In the extreme narrowing limit $\tau_c\omega_0 \ll 1$, the relaxation times approach each other and $T_1 = T_2$ (right).

Quadrupole interaction

The ^{23}Na nucleus possesses a spin of 3/2 [Rabi and Cohen, 1934] and therefore exhibits a nuclear quadrupole moment. For a description of the ^{23}Na NMR signal relaxation, it is sufficient to consider the quadrupole interaction since it is two to three orders of magnitude stronger than the dipole-dipole interaction [Werbelow, 2007]. A derivation of the quadrupole interaction is given in following based on Slichter [1989].
For nuclei with a spin ≥ 1, the nuclear charge density ρ is not symmetric. The quadrapole moment can be described with the diagonal tensor

$$Q_{\alpha\beta} = \int (3x_\alpha x_\beta - \delta_{\alpha\beta} r^2)\rho(\boldsymbol{r})\mathrm{d}^3 r \quad . \tag{2.27}$$

When located in an external electric field $\phi(\boldsymbol{r})$, the potential energy of a nucleus is given by

$$E = \int \rho(\boldsymbol{r})\phi(\boldsymbol{r})\mathrm{d}^3 r \quad . \tag{2.28}$$

For a step-by-step analysis, E is expanded into a Taylor series

$$E = \phi(0)\int \rho(\boldsymbol{r})\mathrm{d}^3 r + \sum_\alpha \frac{\partial\phi}{\partial x_\alpha}\int x_\alpha \rho(\boldsymbol{r})\mathrm{d}^3 r + \frac{1}{2}\sum_{\alpha,\beta}\frac{\partial^2\phi}{\partial x_\alpha \partial x_\beta}\int x_\alpha x_\beta \rho(\boldsymbol{r})\mathrm{d}^3 r + \cdots \tag{2.29}$$

The first term represents the Coulomb energy of a point charge. The second term is a function of the dipole moment of the nucleus. It can be shown that all contributions except

the quadrupole term vanish. Then, the quadrupole tensor can be substituted into the equation by adding the δ distribution term in the integral of Equation 2.27. In combination with the second derivative of the potential ϕ, this vanishes due to Laplace's equation. The quadrupole Hamiltonian is then given by

$$H_{\mathrm{QP}} = \frac{1}{6} \sum_{\alpha,\beta} \frac{\partial^2 \phi}{\partial x_\alpha \partial x_\beta} Q_{\alpha\beta} \quad . \tag{2.30}$$

Making the transition by replacing classical functions with operators and by applying the known commutation relations, the final quantum mechanical Hamiltonian can be derived to be

$$\hat{H}_{\mathrm{QP}} = \frac{eQ}{6I(2I-1)} \sum_{\alpha,\beta} \frac{\partial^2 \phi}{\partial x_\alpha \partial x_\beta} \left[\frac{3}{2} (\hat{I}_\alpha \hat{I}_\beta + \hat{I}_\beta \hat{I}_\alpha) - \delta_{\alpha\beta} \hat{\boldsymbol{I}}^2 \right] \quad . \tag{2.31}$$

The fact, that the nucleus exhibits a state of certain angular moment can be interpreted classically such that their exists a cylindrical symmetry of the charge density. To this end, only one constant is necessary to described Q. For the ^{23}Na nucleus, it was measured to be $Q = 0.109 \pm 0.003$ barn [Stone, 2011].

If the Zeeman interaction is sufficiently stronger than the quadrupole interaction, the change in the energy levels can be determined via first order perturbation theory leading to the energy levels of

$$E_{\mathrm{m}} = E_0 - \gamma m \hbar B_0 + \omega_{\mathrm{QP}} \hbar \quad , \tag{2.32}$$

where $\omega_{\mathrm{QP}}\hbar$ are the energy eigenvalues of $\hat{H}_{\mathrm{QP}}$. They are determined by the quadrupole frequency

$$\omega_{\mathrm{QP}} = \frac{eQ}{4s(2s-1)\hbar} \left[3m^2 - s(s+1) \right] \left[\frac{1}{2} (3\cos^2\theta - 1) + \frac{1}{2} \eta \sin^2\theta \cos 2\varphi \right] \quad . \tag{2.33}$$

Here, θ and φ are the angles between the electric field gradient and the magnetic field. Furthermore, the asymmetry of the potential was introduced with

$$\eta = \left[\frac{\partial^2 \phi}{\partial x^2} - \frac{\partial^2 \phi}{\partial y^2} \right] \cdot \frac{\partial^2 \phi}{\partial z^2}^{-1} \quad . \tag{2.34}$$

For axial symmetry, $\eta = 0$ and the last term in Equation 2.33 vanishes. As can be seen from Equation 2.33, the shift of the resonance lines due to the quadrupole interacation is proportional to m^2. Thus, the outer $m = \pm 3/2$ and the inner $m = \pm 1/2$ states are shifted by the same amount.
For ^{23}Na in biological tissue, commonly two types of environment are characterized as demonstrated by Rooney and Springer [1991a]. This is first, the *type d* environment where

fluctuations of the electric field gradient occur on such a rapid time scale, that they are averaged out. A monoexponential decay is observed. However, in the case of longer correlation times of the order $\tau_c\omega_0 \gtrsim 1$, a temporal modulation of the energy levels occurs in the order of the resonance frequency (cf. **Figure 2.3**). This leads to a biexponential decay of the transverse magnetization and is named a *type c* environment. For ^{23}Na at a field strength of 7 T, $\omega_0^{-1} = 12.7$ ns.

Transverse relaxation for spin 3/2

For a spin 3/2 system, their exist four eigenstates with regard to the free precession Hamiltonian. In the case of rapid motion, quadrupole interaction is averaged out and three degenerate transitions exist which exhibit the same decay rate. The general case is explained in the following.
The transition probability from state m to n is with the density matrix $\rho_{m,n} = \langle m|\,\hat{\rho}\,|n\rangle$. In the case of a multi-spin system, the Redfield theory [Redfield, 1957] provides the formalism for the calculation of transition probabilities and thereby the relaxation constants can be determined. It states that the elements of the density matrix are related by a set of differential equations of the form

$$\frac{\mathrm{d}}{\mathrm{d}t}\rho_{k,k'} = \sum_{j,j'} R_{kk',jj'} \mathrm{e}^{i(k-k'-j+j')t} \rho^*_{jj'} \quad . \tag{2.35}$$

For the 3/2 system, this has been explicitly determined to be [Jaccard et al., 1986]

$$\begin{pmatrix} \rho'_{1,2} \\ \rho'_{2,3} \\ \rho'_{3,4} \end{pmatrix} = C \begin{pmatrix} -(J_0+J_1+J_2) & 0 & J_2 \\ 0 & -(J_1+J_2) & 0 \\ J_2 & 0 & -(J_0+J_1+J_2) \end{pmatrix} \begin{pmatrix} \rho_{1,2} \\ \rho_{2,3} \\ \rho_{3,4} \end{pmatrix} \quad . \tag{2.36}$$

Here, the spectral densities J_n and the coupling constant C are defined as

$$J_n = \frac{2\tau_c}{1+(n\omega_0\tau_c)} \quad \text{and} \quad C = \frac{1}{40}\left(\frac{e^2qQ}{\hbar}\right)\left(1+\frac{\eta^2}{3}\right) \quad . \tag{2.37}$$

This matrix can be diagonalized leading to three uncoupled equations with diagonal entries R_i and vector elements σ_i

$$R_1 = -C(J_0+J_1) \quad , \quad \sigma_1 = \frac{1}{\sqrt{2}}(\sigma_{12}+\sigma_{34}), \tag{2.38}$$

$$R_2 = -C(J_1+J_2) \quad , \quad \sigma_2 = \sigma_{23}, \tag{2.39}$$

$$R_3 = -C(J_0+J_1+2J_2) \quad , \quad \sigma_3 = \frac{1}{\sqrt{2}}(\sigma_{12}-\sigma_{34}) \quad . \tag{2.40}$$

Since the eigenvectors decay exponentially, the decay times are determined via

$$\sigma_i(t) = \sigma_i(0)\mathrm{e}^{R_i t} \quad . \tag{2.41}$$

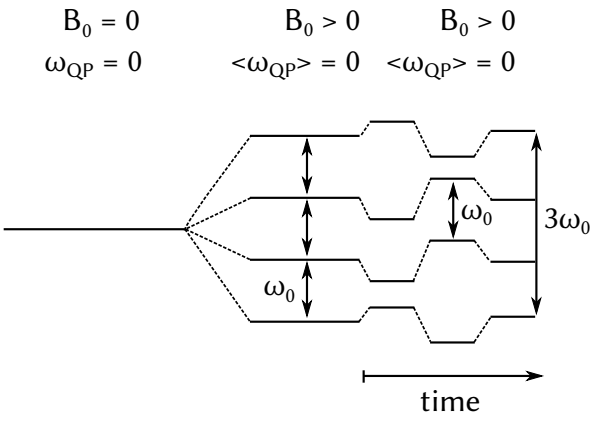

Figure 2.3: Splitting of the energy levels of quadrupole interaction for the fluctuating and static case. For short correlation times, the fluctuations of the electric field gradient are zero in average. For fluctuations with $\tau_c\omega_0 \gtrsim 1$ the outer and inner lines are shifted but the distance is not changed and a biexponential decay is observed.

The outer lines decay with the entries R_1 and the inner component with R_2. In the case of extreme narrowing ($\omega_0\tau_c \ll 1$) and isotropic motion, all spectral densities $J_n = 2\tau_c$ and a monoexpontial is observed with

$$T_2 = \frac{1}{4C\tau_c} \quad . \tag{2.42}$$

For the actual application, the dynamics after a 90° excitation pulse around the y-axis have to be considered. Expressing the Hamiltonian through irreducible tensor operators $T_{l,m}^{S=3/2}$ as in [Müller et al., 1987] and ignoring constant factors

$$\sigma(t=0) = S_x = \sqrt{\frac{5}{2}}(T_{1,-1} - T_{1,+1}) \quad . \tag{2.43}$$

By inserting and only focusing on $p = +1$ coherences, this leads to

$$\sigma(t=0) = \frac{1}{2}\left[\sqrt{3}\,|1\rangle\langle 2| + 2\,|2\rangle\langle 3| + \sqrt{3}\,|3\rangle\langle 4|\right] \quad . \tag{2.44}$$

By a coupled set of equations, this can be transformed into tensor operators

$$\sigma(t) = -\frac{1}{\sqrt{10}}\left[T_{1,+1}\left(3\mathrm{e}^{R_1 t} + 2\mathrm{e}^{R_2 t}\right) + T_{3,+1}\sqrt{6}\left(\mathrm{e}^{R_1 t} - \mathrm{e}^{R_2 t}\right)\right] \quad . \tag{2.45}$$

Only single-quantum coherences are visible in a one-pulse experiment. Thus, the first term describes the transverse relaxation through quadrupole interaction. A biexponential decay is found with contributions of 60 % and 40 %. The relaxation times are the inverse of the rates R_i, being

$$T_{2,\mathrm{s}} = \frac{1}{J_0 + J_1} \quad \text{and} \tag{2.46}$$

$$T_{2,\mathrm{l}} = \frac{1}{J_1 + J_2} \quad . \tag{2.47}$$

By inserting the spectral densities with the assumption of exponentially decaying correlation function, they are in terms of correlation times and resonance frequency

$$T_{2,\mathrm{s}} = \frac{1}{C\left(2\tau_c + \frac{2\tau_c}{1+(2\omega_0\tau_c)^2}\right)} \quad \text{and} \tag{2.48}$$

$$T_{2,\mathrm{l}} = \frac{1}{C\left(\frac{2\tau_c}{1+(\omega_0\tau_c)^2} + \frac{2\tau_c}{1+(2\omega_0\tau_c)^2}\right)} \quad . \tag{2.49}$$

In summary, 60 % of the signal exhibit a short relaxation time with $T_{2,\mathrm{s}}$ and 40 % decay with the longer $T_{2,\mathrm{l}}$. The relaxation times of the two components and their ratio is shown in **Figure 2.4** for varying τ_c. Due to the strength of the quadrupole interaction compared to the dipole-dipole interaction, the relaxation times of ^{23}Na are shorter than those of ^{1}H by one to two orders of magnitude.

2.1.5 Signal reception and NMR sensitivity

The NMR signal can be detected through induction of a voltage in a nearby receive coil. Faraday's law states, that the voltage is proportional to the change in magnetic flux ϕ

$$V_{\mathrm{ind}}(t) = \frac{\partial\phi}{\partial t} \quad . \tag{2.50}$$

In the case of the precessing magnetization $\boldsymbol{M}(\boldsymbol{r})$ at location $\boldsymbol{r}$, this becomes an integral over the complete volume of the object

$$V_{\mathrm{ind}}(t) = -\frac{\partial}{\partial t}\int \boldsymbol{B}(\boldsymbol{r})_1\boldsymbol{M}(\boldsymbol{r},t)\mathrm{d}^3r \quad . \tag{2.51}$$

Here, the $\boldsymbol{B}_1$ symbolizes the sensitivity of the coil at location $\boldsymbol{r}$, which equals the transmit field. Carrying out the derivative, the induced signal amplitude $S(t)$ shows the proportionality

$$S(t) \propto \omega_0 \int M_\perp(\boldsymbol{r})\mathrm{e}^{-t/T_2(\boldsymbol{r})}B_1(\boldsymbol{r})\sin(\omega_0 t)\mathrm{d}^3r \quad . \tag{2.52}$$

The magnetization is proportional to the spin density $\rho(\boldsymbol{r})$ (cf. Equation 2.12) and the Larmor freuency $\omega_0 = \gamma B_0$. From this, an estimate of the NMR sensitivity of different nuclei can be derived. As a result, for ^{23}Na and ^{1}H in human tissue, an about four orders of magnitude weaker signal is observed [Madelin and Regatte, 2013].

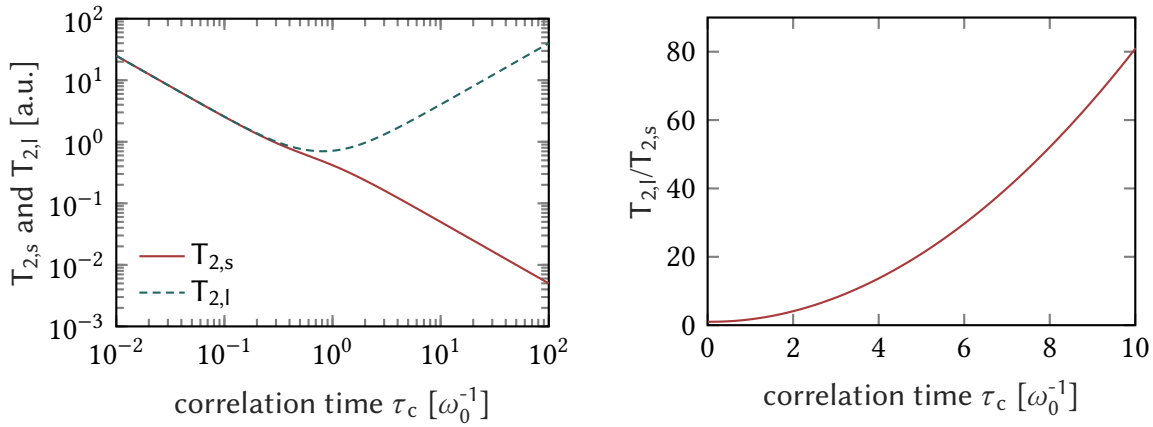

Figure 2.4: Relaxation components of the quadrupole T_2 decay as function of the correlation time τ_c. Left: At $\omega_0\tau_c \ll 1$, a monoexponential decay is observed. At longer correlation times of the order $\omega_0\tau_c \gtrsim 1$, the two components split. Right: For $\omega_0\tau_c \ll 1$, the ratio of the two relaxation times increases with the correlation time.

2.2 Magnetic resonance imaging

In magnetic resonance imaging (MRI), the NMR signal is modulated by linear magnetic field gradients, which enables a spatial resolution of the object via the signal phase. This will be explained in more detail in this section on the basis of [Haacke et al., 1999] and [Bernstein et al., 2004].

2.2.1 Spatial encoding by means of magnetic field gradients

The signal detected by an RF coil (cf. Equation 2.52) is the integral over the full object. The origin of the signal can be resolved by application of additional magnetic field gradients $\boldsymbol{G}$, which are superimposed on the main magnetic field. In case of three independent linear gradients

$$\boldsymbol{G} = (G_x, G_y, G_z)^{\mathrm{T}} \tag{2.53}$$

the local precession frequency is changed

$$\omega(\boldsymbol{r}) = \omega_0 + \gamma \boldsymbol{G}\boldsymbol{r} \quad . \tag{2.54}$$

At time t, the local signal phase at position $\boldsymbol{r}$ is thus

$$\varphi(\boldsymbol{r}, t) = \gamma \int_0^t \boldsymbol{G}(t')\mathrm{d}t'\boldsymbol{r} = 2\pi \boldsymbol{k}(t)\boldsymbol{r} \quad , \tag{2.55}$$

where the spatial frequency $\boldsymbol{k}$ was defined with

$$\boldsymbol{k}(t) = \frac{\gamma}{2\pi} \int_0^t \boldsymbol{G}(t')\mathrm{d}t' \quad . \tag{2.56}$$

Inserting the space-dependent phase into the signal equation (cf. Equation 2.52), the complex valued signal is determined by

$$\boldsymbol{S}(\boldsymbol{k}, t) \propto \int M_\perp \mathrm{e}^{-2\pi i \boldsymbol{k}\boldsymbol{r}} \mathrm{d}^3 r \tag{2.57}$$

Signal relaxation and constant contributions are neglected in this equation. From this relation, it follows that the measured signal is the Fourier transformation (FT) of the magnetization and can be determined by

$$M_\perp(\boldsymbol{r}) \propto \int S(\boldsymbol{k}) \mathrm{e}^{2\pi i \boldsymbol{k}\boldsymbol{r}} \mathrm{d}^3 k \quad . \tag{2.58}$$

The necessary requirements for the sampling of the signal in the so-called k-space are well-known from signal theory and are described in the following section.

2.2.2 Discrete sampling and Fourier reconstruction

It is only possible to sample the signal at discrete points and within a certain band of spatial frequencies k. In classical sampling theory [Nyquist, 1928], the requirements for the recovery of a signal from a final number of discrete, equally spaced samples are determined by the Shannon-Nyquist theorem. For the one-dimensional case, the nominal image resolution Δx and the field of view (FOV) are determined by the highest value acquired in k-space $k_{\max}$ and the sampling width Δk by

$$\mathrm{FOV} = \frac{1}{\Delta k} \quad \text{and} \tag{2.59}$$

$$\Delta x = \frac{1}{2k_{\max}} \quad . \tag{2.60}$$

In general, the k-space can be sampled in an arbitrary fashion as long as the above criteria are fulfilled. Conventionally, cartesian schemes are used, which allow a fast image reconstruction via the fast Fourier transformation (FFT). For ^{23}Na MRI, radial acquisition strategies are employed, where the k-space is sampled by radial center out trajectories, so-called projections. Thus, a sphere with radius $k_{\max}$ is covered. The Nyquist criterion applies in this case in the radial and angular directions, leading to the requirements

$$\Delta k_r = \frac{1}{\mathrm{FOV}_r} \quad \text{and} \tag{2.61}$$

$$N_{\mathrm{proj}} = 4\pi \left(\frac{\mathrm{FOV}}{2\Delta x} \right)^2 \quad . \tag{2.62}$$

The index r stands for the radial direction and N_{proj} is the number of equally space projections. It is noted at this point, that these classical requirements can be loosened by the theory of compressed sensing as shown for the application in MRI by Lustig et al. [2007].

During the acquisition or reconstruction of the MRI data, the k-space is likely to undergo some kind of desired or undesired filtering. Some typical examples occurring for ^{23}Na MRI are shown in **Figure 2.5** with the respective filter function and the reconstructed image. The filter functions are divided into two classes: *step-type* filters and *smooth* filters. Step-type filtering is represented by a filter function consisting of zeros and ones. An examples during the acquisition is the band-limitation leading to a finite resolution. This is shown in (a) and (b) where k-space is sampled up to two different values of k_{max}. For the lower resolution in b), typical *Gibbs ringing* artifacts are visible additionally to the decreased resolution. The higher spatial frequencies, contained in the k-space periphery are shown in (c). The case of radial sampling, where a sphere in k-space is acquired, is shown in d). A loss of resolution is found, due to the missing information from the edges [Rahmer et al., 2006]. In order to minimized the ringing artifacts in low resolution image, a Hamming filter is often applied, which is designed to suppress the side bands of the point spread function (PSF). This is an example of a smooth filter, which continuously modulates the amplitude of the k-space. In (e) and (f), example reconstructions are shown for two base resolutions. It can be seen that the application of the Hamming filter decreases the resolution (e) but also suppresses the ringing (f). Due to the rapid T_2^* decay of the ^{23}Na signal, a damping of higher frequencies occurs dependent on the readout time of the projections (T_{RO}). This effect is demonstrated in (g) and (h) for a biexponential decay with decay times of $T_{2,\text{s}}^* = 5\,\text{ms}$ and $T_{2,\text{l}}^* = 40\,\text{ms}$ and T_{RO} of 10 ms and 5 ms. In the reconstruction of the shorter T_{RO}, a better resolution of small structures can be seen. However, also ringing artifacts are suppressed by this intrinsic filtering.

2.2.3 MRI image contrasts

Different image contrasts can be achieved in MRI since relaxation constants and spin density are characteristic for each tissue. The contrast can be influenced by the acquisition parameters echo time (TE), repetition time (TR), and the flip angle α. For a gradient echo experiment, which can be characterized by subsequent application of excitation and signal readout with perfect spoiling, the signal amplitude is

$$S \propto \rho \frac{1 - \mathrm{e}^{-TR/T_1}}{1 - \cos(\alpha)\mathrm{e}^{-TR/T_1}} \sin(\alpha) \mathrm{e}^{-TE/T_2^*} \quad . \tag{2.63}$$

The flip angle, leading to the most efficient acquisition is the so-called *Ernst angle* [Ernst and Anderson, 1966] and is determined by

$$\alpha_{Ernst} = \arccos(\mathrm{e}^{-TR/T_1}) \quad . \tag{2.64}$$

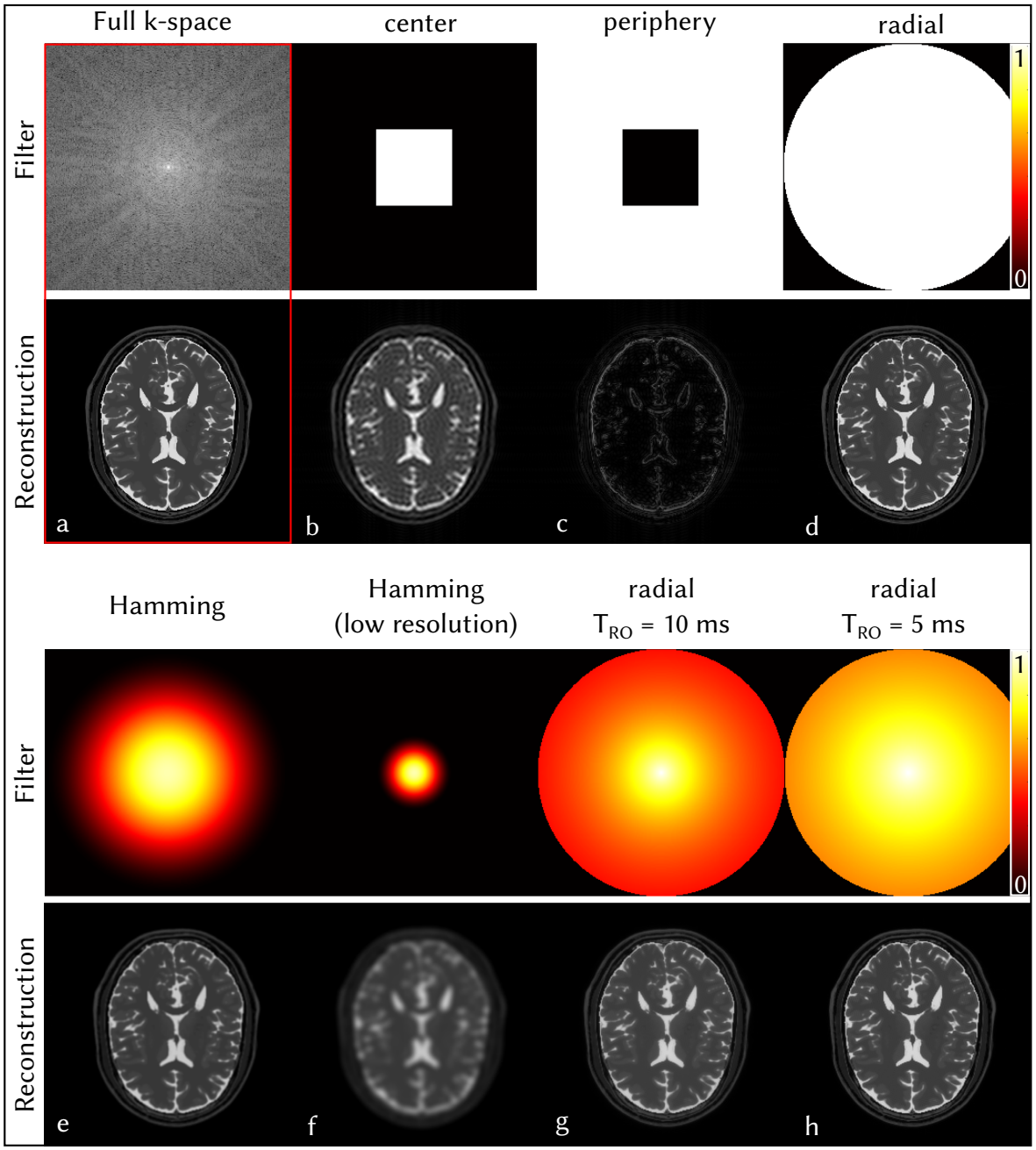

Figure 2.5: Examples for filtering of k-space data. Shown are filter functions and the respective reconstructions. The full k-space and the reconstruction at 1 mm resolution is shown in (a). In (b) and (c) only center or periphery are considered. Spherical coverage is shown in (d). In (e)-(h) four kinds of smooth filters are shown: a) and b) depict Hamming filtering at the resolutions shown in (a) and (b), and (g) and (h) depict filtering by T_2^* decay along radial trajectories for two different readout durations. See text for further description.

2.2.4 Noise in magnitude data

The noise in MRI data has two main sources, the object itself and electronic consisting of the coil and further electronic contributions. It exhibits a complex Gaussian distribution with standard deviation σ_k at every measurement point in k-space. The observed noise variance can be expressed summing up the independent contributions by

$$\sigma_\mathrm{k}^2(\boldsymbol{k}) = \sigma_\mathrm{object}^2(\boldsymbol{k}) + \sigma_\mathrm{coil}^2(\boldsymbol{k}) + \sigma_\mathrm{electronics}^2(\boldsymbol{k}) \tag{2.65}$$

$$\propto 4k_bT \cdot R \cdot BW \quad . \tag{2.66}$$

The noise amplitude is proportional to the temperature T, the effective resistance of the coil R and the readout bandwidth BW. However, for an imaging experiment, the SNR in the image space is most important. Through image reconstruction via the FT, the Gaussian distribution of noise is sustained. Thus, the SNR in image space is defined by the ratio of the signal $S(\boldsymbol{r})$ and the observed noise standard deviation in image space σ_m

$$\mathrm{SNR}(\boldsymbol{r}) = \frac{S(\boldsymbol{r})}{\sigma_\mathrm{m}} \quad . \tag{2.67}$$

Typically, magnitude image data is used which are derived from the complex valued data. This changes the distribution of the noise to a so-called *Rician* distribution [Gudbjartsson and Patz, 1995]. In a region without signal, mean and standard deviation of the Rician distribution are connected to the Gaussian by

$$\sigma_\mathrm{Rice}^2 = (2 - \pi/2)\sigma_\mathrm{Gauss}^2 \quad \text{and} \tag{2.68}$$

$$\bar{S}_\mathrm{Rice} = \sqrt{\pi/2}\sigma_\mathrm{Gauss} \quad . \tag{2.69}$$

The two distributions are compared in **Figure 2.6** for regions with and without signal. The Rician distribution approximates the Gaussian for SNR ≈ 3.

2.2.5 Observation of the transverse relaxation

In the following, basic acquisition schemes for the measurement of T_2 and T_2^* are described and a short summary of the research concerning the distribution of the temporal sampling points in ^{1}H MRI is given. Radial k-space sampling will be used throughout as example readout scheme since this is applied in ^{23}Na MRI due to the rapid decay. A list of previous T_2^* reports for ^{23}Na is also provided.

Pulse sequences

The apparent decay time T_2^* is typically measured with a multi-echo gradient echo sequence. A schematic diagram is shown in **Figure 2.7**. After the excitation pulse, a prewinder

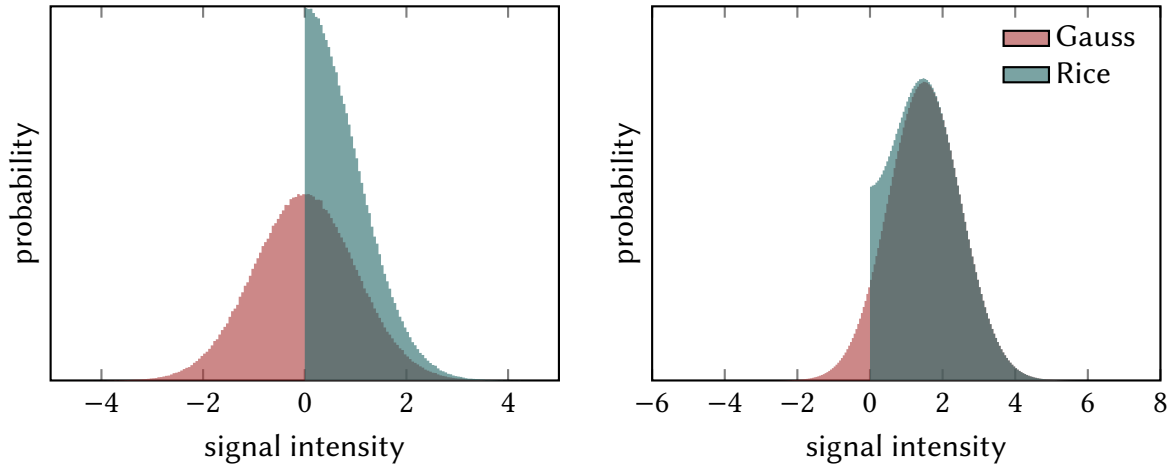

Figure 2.6: Comparison of Gaussian and Rician distribution. Left: In a region without signal, both distributions differ but the Rician distribution approaches the Gaussian for SNR > 0 (right).

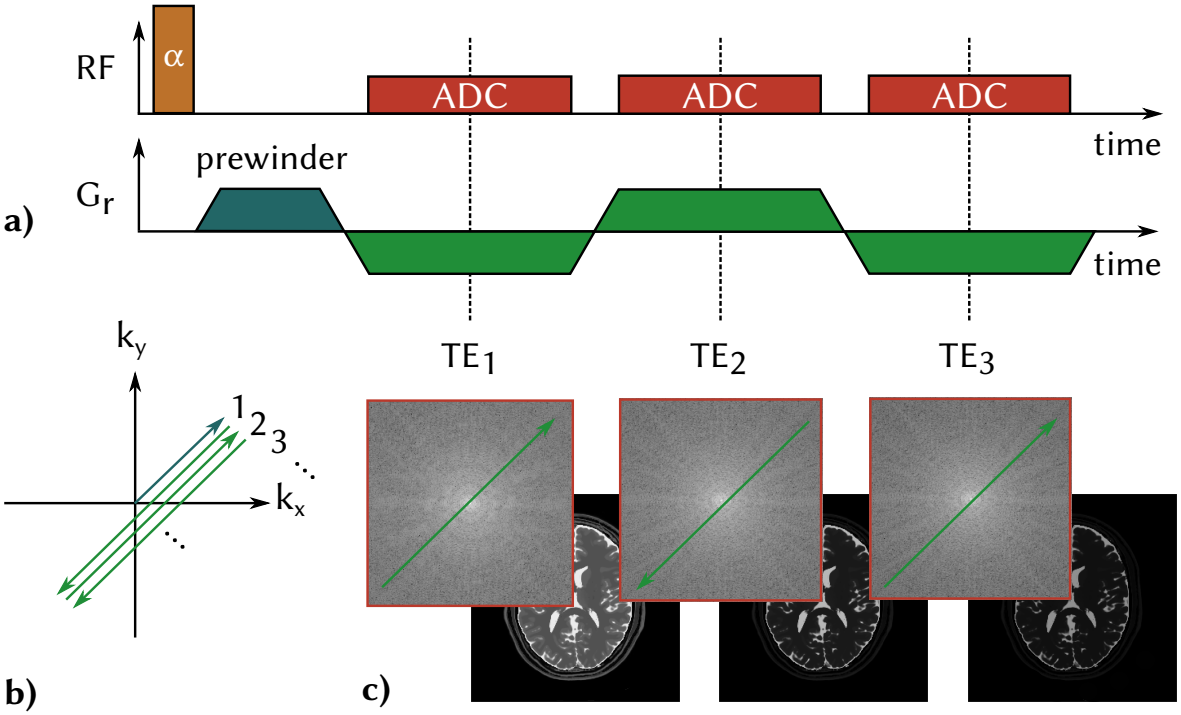

Figure 2.7: Sequence diagram of a multi-echo gradient echo pulse sequence (a). After the excitation, a prewinder gradient prepares the magnetization for the following bipolar readouts. The resulting k-space trajectory is displayed in (b) and example multi-echo data together with image reconstructions are shown in (c).

gradient prepares the magnetization towards the specific position in k-space where the readout should start. Each line is then sampled continuously by switching between positive and negative gradient polarity. The echo time TE_i is defined as the time at which the k-space center is acquired. The k-space is filled by repeating the temporal sampling at all necessary k-space lines (cf. Section 2.2.2). For the determination of T_2, an additional 180° refocusing pulse is inserted in order to refocus dephasing due to B_0 field inhomogeneities (cf. **Figure 2.8**). The refocusing pulse is switched at $TE/2$ to achieve full rephasing at the time of the acquisition. Additionally, crusher gradients are switched before and after the 180° pulses to minimize residual excitation due to B_1 inhomogeneities. B_1 field inhomogeneities can lead to incomplete refocusing especially at ultra-high field (UHF) and SAR can become an issue. More accurate values for T_2 can be determined by performing a single-echo spin echo (SE) acquisition with varying echo times. This however, prolongs measurement duration.

Sample distribution

The timings of the *TE* in a multi-echo relaxation measurement can have significant influence on the accuracy. In the following, a short summary of the research in ^{1}H MRI is given concerning sample distribution for decay quantification. It was reported that the optimal strategy to sample an exponential decay is to use as few different sampling times as possible and rather apply averaging ([Haacke et al., 1999], p. 664ff). Accuracy can be increased by choosing sampling times such that they allow an efficient determination of the underlying parameters by matching the signal shape with the sample positions. For increased accuracy these points can then be averaged multiple times. Jones et al. [1996] reported that best accuracy can be obtained when placing measurements only at two time points: $t_1 = 0\,\text{ms}$ and at $t_2 = 1.28 \cdot T_2$. The point at t_2 should be sampled four times as often as t_1. Thus, this sampling pattern is solely determined by the value of T_2 in the tissue. It has been shown, that sampling patterns with a small number of sampling points are generally superior to multi-point strategies when averaging can be performed Fleysher et al. [2008].

Previous ^{23}Na T_2^* measurements

A list of previous studies of ^{23}Na T_2^* measurements in brain at a field strength of 7 T is given in **Table 2.3**. Only considering studies at 7 T, a variation from 2 ms to 5 ms is found for $T_{2,\text{s}}^*$. $T_{2,\text{l}}^*$ is often considered to be detectable with higher accuracy since a higher sampling rate can be achieved ($T_{\text{RO}} < T_{2,\text{l}}^*$). Still, a large spread of values between 22 ms and 40 ms is seen. The even longer decay time of cerebrospinal fluid (CSF) ranges from 47 ms to 57 ms at 7 T. A more extensive list can be found at the end of the chapter including other field strengths and acquisition parameters (**Table 2.3**).

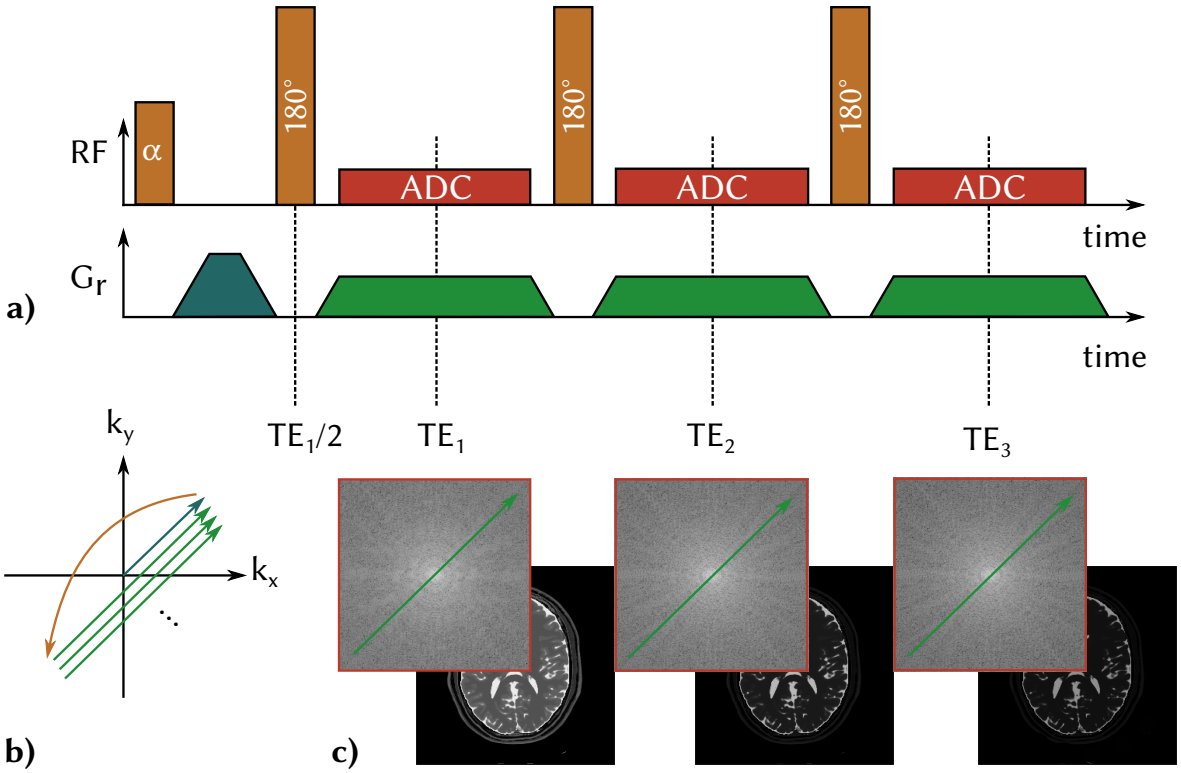

Figure 2.8: Sequence diagram of a multi-echo spin echo experiment. A 180° pulse is applied at *TE*/2 leading to refocusing of the magnetization at *TE* (a). The k-space trajectory produced by the gradients is displayed (b) together with k-space and image data (c).

Table 2.1: Overview of previous studies of the apparent transverse relaxation time T_2^* of ^{23}Na in brain tissue at 7 T. Separate values for $T_{2,s}^*$ and $T_{2,l}^*$ are given together with the relative contribution (r) of each component. The different tissue types are GM, WM, CSF, brain parenchyma (BP = WM + GM), vitreous humor (VH), and whole brain (WB). A detailed list of previous studies including other field strengths and acquisition parameters is presented at the end of the chapter (page 26).

Study	**Tissue type**	$T_{2,s}^*$ [ms]	$T_{2,l}^*$ [ms]	r
Fleysher et al. 2009	WM	-	29±2	0
	GM	-	28±2	0
	CSF	-	54±4	0
Nagel et al. 2011	BP	4.7±2	40± 2	0.67±0.02
	CSF	-	56±4	0
Niesporek et al. 2017	WM	3.5±0.1	23.3±2.6	0.6
	GM	5.4±0.2	36.4±3.1	0.6
	CSF	-	46.9±2.1	0
Blunck et al. 2017	WM	1.99±2.09	22.4±7.8	0.6
	GM	2.02±1.67	25.9±8.3	0.6
	CSF	-	57.2±6.6	0
Bydder et al. 2017	WM	4.50±0.65	39.99±5.24	0.6
	GM	5.02±0.89	33.89±5.96	0.45

2.3 Physiological role of sodium

^{23}Na is essential for a number of biological processes and occurs as positively charged Na^+ ions in the body. In the intracellular space, the concentration is about 12 mM and in the extracellular space it is 143 mM [Silbernagl and Despopoulos, 2003; Alberts et al., 2002]. This concentration gradient is actively regulated by the Na^+-K^+-ATPase ("sodium-potassium pump") under the consumption of ATP. The Na^+-K^+-ATPase is a membrane enzyme which exists in all animal cells. During each action cycle, it transports three Na^+ through the membrane into the extracellular space and at the same time pumps two K^+ into the cell. Thus, the concentration of K^+ is inverted compared to the Na^+ ions. The intracellular concentration is 140 mM and extracellular only 4 mM are found. Together with Cl^- ions, the membrane potential can be closely approximated by the Goldmann-Hogkin-Katz equation

$$\phi_m = \frac{RT}{F} \cdot \ln \frac{P_{\mathrm{Na}}[\mathrm{Na}^+]_{\mathrm{ex}} + P_{\mathrm{K}}[\mathrm{K}^+]_{\mathrm{ex}} + P_{\mathrm{Cl}}[\mathrm{Cl}^+]_{\mathrm{in}}}{P_{\mathrm{Na}}[\mathrm{Na}^+]_{\mathrm{in}} + P_{\mathrm{K}}[\mathrm{K}^+]_{\mathrm{in}} + P_{\mathrm{Cl}}[\mathrm{Cl}^+]_{\mathrm{ex}}} \quad . \tag{2.70}$$

Here, R is the gas constant, T the temperature, F the Faraday constant and P the permeability of the cell membrane for the respective ion. The indexes stand for intra- and extracellular space. In the case of energy under supply, the Na^+-K^+-ATPase breaks down and cell swelling leads to apoptosis. This process is accompanied by an increase in average sodium concentration of the tissue. The tissue sodium concentration has therefore been described as a measures of cell viability. A number of applications have been reported for ^{23}Na concentration measurements via MRI [Madelin and Regatte, 2013] ranging from studies in tumors or kidney to applications in muscle and cartilage towards neurodegenerative diseases such as multiple sclerosis and Alzheimer's. In the latter, ^{23}Na is especially interesting since the action potential of neuron is a result of the triggered inflow of Na^+ ions, which leads to a depolarization of the cell.

Table 2.2: Overview of previous studies of the (apparent) transverse relaxation time $T_2^{(*)}$ of ^{23}Na in brain tissue. Separate values for $T_{2,s}^*$ and $T_{2,l}^*$ are given together with the relative contribution (r) of each component. Detailed parameters concerning the sampling strategy are listed being: the time of the first/last sampling point TE_{min}/TE_{max}, the number of samples (No.), and the sampling strategy (equidistant with spacing ΔTE, logarithmic, or other (a-d)). The different tissue types are gray matter (GM), white matter (WM), cereborspinal fluid (CSF), brain parenchyma (BP = WM + GM), vitreous humor (VH), and whole brain (WB).

Study(1)	**Tissue type**	$T_{2,s}^{*}$ (2) [ms]	$T_{2,l}^{*}$ (2) [ms]	r(3)	B_0 [T]	**Sequence**	TR [ms]	TE_{min} [ms]	TE_{max} [ms]	ΔTE [ms]	**No.**	TA [min]
Cope(4) **1970** Rat, post-mortem	WB	0.75	10	0.6–0.7	0.9	FID	250	0.81	-	≈ 0.14 for $T_{2,s}$	-	-
Ra et al. 1986	BP	$\leq$3	-	-	1.5	Hybrid SE	-	3.6	14	-	-	-
Perman et al. 1989	VH	-	56.8±2.1	0	1.5	3D SE	100	3	$\approx$ 27	$\approx$ 3	8	-
	GM/WM	-	16.8–17.6±2.4	0								
Winkler et al. 1989	WM	-	12.4±3.2	0	1.5	3D SE	98	3	12	3,6,9,12	4	34
	Cortex	-	11.2±3.1	0								
	CSF	-	47.5±20.6	0								
	Blood	-	20.9±6.0	0								
	VH	-	58.0±26.6	0								
Boada et al. 1997	BP	3	15	0.60	1.5	(TPI)	-	-	-	-	-	-
	BP	-	7.6	0.00								

(1-4) and (a-d): For an explanation of the indexes as well as for a detailed list of the sampling times see end of the table at page 25.

Table 2.2: (Continued) Overview of previous studies of the (apparent) transverse relaxation time $T_2^{(*)}$ of ^{23}Na in brain tissue.

Study[1]	**Tissue type**	$T_{2,s}^{*}$ [2] [ms]	$T_{2,l}^{*}$ [2] [ms]	r [3]	B_0 [T]	**Sequence**	TR [ms]	TE_{min} [ms]	TE_{max} [ms]	ΔTE [ms]	**No.**	TA [min]
Constantinides et al. 2000	BP	2.11±3.3	19.95±2.3	-	1.5	TPI	100	0.37	20	-	-	-
Winter and Bansal 2001 (Rat brain)	WB	3.0±0.2	26.0±0.8	0.64 ± 0.02	9.4	SE	-	0.05	50	log.	15	-
Bartha and Menon 2004	WM	-	19	0.6	4	GRE	80	3.8	68.7	(a)	10	22
Fleysher et al. 2009	WM GM CSF	- - -	29±2 28±2 54±4	0 0 0	7	GRE	130	12	37	12,37	2	63
Lu et al. 2011	WM GM CSF	0.2-3.0 -	10 14 55	- - 0	3	TPI	160	0.2	25.2	3.45	24	60
Nagel et al. 2011	BP CSF	4.7±2 -	40± 2 56±4	0.67±0.02 0	7	DA 3D-RAD	70	0.4	55	1	56	65

(1-4) and (a-d): For an explanation of the indexes as well as for a detailed list of the sampling times see end of the table at page 25.

Table 2.2: (Continued) Overview of previous studies of the (apparent) transverse relaxation time $T_2^{(*)}$ of ^{23}Na in brain tissue.

Study[1]	Tissue type	$T_{2,s}^{*}$ [2] [ms]	$T_{2,l}^{*}$ [2] [ms]	r[3]	B_0 [T]	Sequence	TR [ms]	TE_{min} [ms]	TE_{max} [ms]	ΔTE [ms]	No.	TA [min]
Niesporek et al. 2017	WM	3.5±0.1	23.3±2.6	0.6	7	DA-3DPR	250	0.35	100	(b)	32	67
	GM	5.4±0.2	36.4±3.1	0.6								
	CSF	-	46.9±2.1	0								
Blunck et al. 2017	WM	1.99±2.09	22.4±7.8	0.6	7	3D-MERINA	160	0.4	122	2	38	27
	GM	2.02±1.67	25.9±8.3	0.6								
	CSF	-	57.2±6.6	0								
Bydder et al. 2017	WM	4.50±0.65	39.99±5.24	0.6	7	DA 3D-RAD	120	0.3	100	(c)	24	60
	GM	5.02±0.89	33.89±5.96	0.45								
This study (linear/ optimized)	WM	2.8±0.3/ 0.7±0.4	34.0±0.8/ 28.6±1.1	0.6	7	DA 3D-RAD	65	0.35	55	(d)	32	60
	CSF	-	47.4±2.6/ 47.9±2.2	0								

(1) Studies are listed chronologically. If not stated differently, the data are from healthy human volunteers.
(2) Given is the apparent transverse relaxation time T_2^* except for the studies of Ra et al., Perman et al., Winkler et al., and Winter et al., who employed spin-echo techniques.
(3) $r = 0$ represents a monoexponential signal model. The relaxation time is given as $T_{2,l}^*$.
(4) Separate fitting of $T_{2,s}^*$ and $T_{2,l}^*$
Details on sampling schemes [ms]:
a) 3.8, 13.9, 17.5, 27.6, 31.2, 41.3, 44.9, 55.0, 58.5, 68.7
b) 0.35, 6.5, 14, 21, 28, 35, 45, 55; 0.5, 10, 18, 25, 32, 40, 50, 70; 1.5, 8, 16, 23, 30, 38, 47, 100; 3, 12, 19, 26, 33, 42, 49, 85
c) 0.3, 0.8, 2.3, 6.3, 7, 9.7, 12, 13, 15, 17, 19, 21, 23, 25, 28, 31, 35, 40, 45, 54, 66, 80, 89, 100
d) See **Table 4.5**.
- = not mentioned or not applicable
Sequence abbreviations: DA-3DPR – Density-adapted 3D projection reconstruction [Nagel et al., 2009], FID – Free induction decay, GRE – Gradient Echo Sequence/ FLASH, SE – Spin-Echo, TPI – Twisted Projection Imaging [Boada et al., 1997], Hybrid SE – detailed description in original work [Ra et al., 1986]

3 Methods

In this chapter the methods employed in this work are presented. First, the necessary hard- and software for the MRI acquisition and image formation are described. Then, an optimization procedure for the distribution of the T_2^* sampling is shown. Finally, additional methods are explained which were required for different evaluation procedures.

3.1 The imaging process

In this section the required hard- and software for imaging of ^{23}Na and ^{1}H are shown. In the first part, hardware and pulse sequences are explained which were employed for the signal acquisition. In the second part, the image reconstruction from radial k-space data and multi-channel receive arrays is described.

3.1.1 Data acquisition

The MRI data acquisition requires an MRI scanner and RF coils for transmission and reception as well as dedicated pulse sequences for specific contrasts and spatial resolution of the object. The respective characteristics are provided in the following sections.

Hardware

MRI Scanner The superconducting solenoid coil of the MRI scanner establishes the main magnetic field B_0 and three independent gradient coils produce the imaging gradients. All measurements in this thesis were carried out at a passively shielded 7 T whole-body scanner (Magnetom 7 T, Siemens Healthineers, Erlangen, Germany). The tomograph is equipped with a broadband amplifier which enables the transmission and reception on multiple distinct frequencies of different nuclei besides the standard ^{1}H channel. Relevant frequencies for this work were 297.16 MHz for ^{1}H imaging and 78.60 MHz for ^{23}Na. The gradient performance is characterized by a maximum amplitude of 40 mT/m in x- and y-direction and 45 mT/m in z-direction (direction of the main field and table movement). The minimal rise time to maximum amplitude is 200 µs with the maximum slew rate being 200 T/m/s. A view of the scanner is shown in **Figure 3.1**.

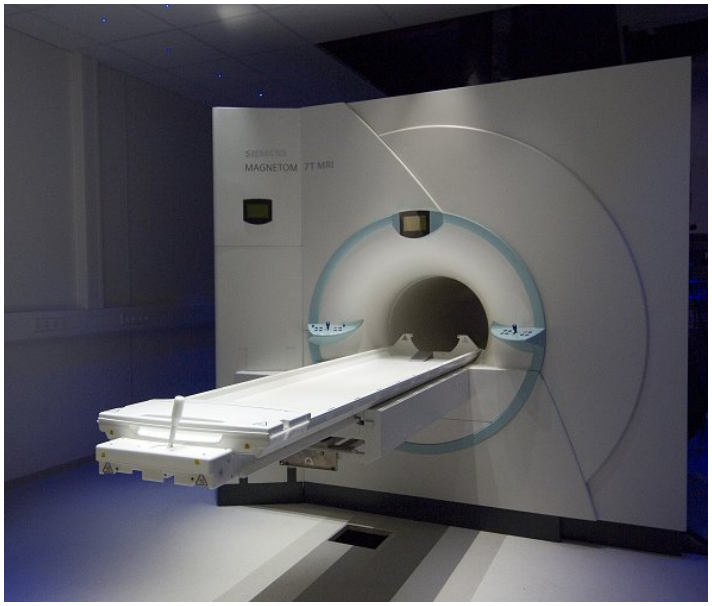

Figure 3.1: View on the 7 T whole-body scanner. Photograph from dkfz.de (10/21/2017).

Radio frequency coils During this work, two ^{23}Na RF coils and one ^{1}H coil were utilized. These are a double-tuned ^{1}H/^{23}Na Tx/Rx birdcage, a double-tuned ^{1}H/^{23}Na Tx/Rx birdcage with a nested 30-channel Rx array (both by RAPID Biomedical GmbH, Rimpar, Germany), and a ^{1}H Tx/Rx birdcage with a nested 24-channel Rx array (Nova Medical, Wilmington, Massachusetts, USA). The RF coils are depicted in **Figure 3.2**. All three coils use birdcage volume resonators for transmission [Vaughan et al., 1994]. Compared to surface coil geometries, these allow a relatively homogeneous excitation profile. However, the multi-channel array inserts of the two latter coils show a higher SNR efficiency [Roemer et al., 1990].

Agarose tissue phantom Agarose gels are employed for validation and testing of quantitative imaging methods since their MRI properties are similar to tissue. Agarose is a polysaccharide derived from seaweed, which after heating in a liquid solution forms a continuous mesh. Phantoms are typically characterized by the amount of agarose which they contain given in mass percent. Increasing the concentration results in shortening of both T_1 and T_2 relaxation times of the phantom. For concentrations of 2 % to 5 %, the pore sizes of the gel is in the range of 200 nm to 400 nm [Pernodet et al., 1997] and is dependent on temperature [Narayanan et al., 2006]. In the phantom studies of this work, concentrations ranging from 0 % to 7 % were used, allowing the analysis over a range of relaxation times. The different agarose concentrations where contained in smaller cylinders with an inner diameter of 43 mm and were circularly arranged inside of a larger cylinder filled with pure NaCl solution having a diameter of 190 mm (cf. **Figure 3.3**). The base medium of the phantom is a 0.9 % NaCl solution. This phantom was first presented by Benkhedah [2013].

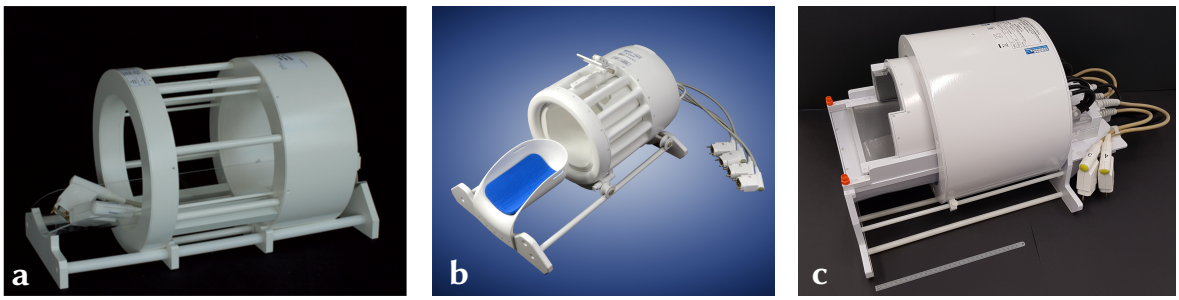

Figure 3.2: Radio frequency coils used in this work. a) 1-channel ^{23}Na Tx/Rx birdcage (BC), b) ^{23}Na Tx/Rx birdcage with 30-channel Rx array, and c) ^{1}H Tx/Rx birdcage with 24-channel Rx array. Courtesy of RAPID Biomedical (a, b).

Figure 3.3: Image of the phantom with different agarose concentrations. The smaller tubes are filled with agarose concentration from 1 % to 7 % and have a diameter of 43 mm. They are surrounded by pure 0.9 % NaCl solution in a cylinder of 190 mm diameter.

Computational recourses All computations were performed on either of the following machines: a standard desktop PC for basic development ("PC1"), another PC equipped with strong recourses of random access memory (RAM) ("PC2"), which was used especially for the memory-intensive reconstructions of the array-coil data, and a high performance computing cluster (HPC), which allowed strong parallelization necessary for the optimization and calculation of SNR maps.

PC1 The standard desktop PC was running Windows 7 Enterprise (Microsoft, Redmond, Washington, USA) and based on a 64-bit architecture with Core i7 processor (Intel, Santa Clara , California, USA) having 4/8 cores/threads and 16 GB RAM.

PC2 The PC with increased RAM was running Windows 7 Enterprise with a processor of the type Intel Xeon E5-v3 having 8/16 cores/threads and 128 GB RAM.

HPC The HPC was running on Windows Server 2008 R2 Enterprise and based on the 64-bit architecture. The cluster setup consisted of one head node managing four worker nodes. The head node was equipped with two Intel Xeon E5620 CPUs with 4/8 cores/threads and 24 GB memory. The worker nodes consisted of two Intel Xeon E5649 CPUs with 6/12 cores/threads. In total, 96 hyperthreaded cores could be used with 2 GB memory each and 128 GB for the complete HPC. This cluster setup was developed by Breithaupt [2015].

MR pulse sequences

The acquisition of the ^{23}Na MRI signal data was performed using a sampling-density-adapted 3D radial (DA 3D-RAD) sequence proposed by Nagel et al. [2009]. A multi-echo version of this readout allowed time resolved measurements of the signal decay. For anatomical reference, two ^{1}H sequences were measured. These were the magnetization prepared rapid acquisition gradient echo (MPRAGE) and the constructive interference in steady state (CISS) sequences. In the following, basic characteristics of these acquisition schemes are given.

Density-adapted 3D radial sequence (DA 3D-RAD) The fast relaxation of the ^{23}Na signal requires shorter echo times than conventional Cartesian trajectories. Radial k-space sampling allows immediately acquiring the signal after the excitation pulse and is therefore most suitable for fast decaying signal [Konstandin and Nagel, 2014]. A disadvantage of radial acquisition is the decreasing sampling density towards the k-space periphery, which leads to lower SNR efficiency [Liao et al., 1997]. This can be compensated by adapting the k-space trajectory to the radial sampling density [Boada et al., 1997; Nagel et al., 2009]. A derivation of the gradient waveform is outlined in the following.

In the case of white Gaussian noise and variance σ_k^2 in each k-space sample point, the noise variance in image space σ_i^2 is determined by

$$\sigma_i^2 \propto \int_{V_k} \frac{\sigma_k^2}{D(\boldsymbol{k})} \mathrm{d}^3k \quad . \tag{3.1}$$

The integration is evaluated over the acquired k-space volume V_k and $D(\boldsymbol{k})$ is an arbitrary filter function. The highest SNR efficiency is achieved for uniform sampling [Liao et al., 1997]. To realize this, the amplitude of the imaging gradients can be modulated as a function of the k-space radius. This is expressed in a filter function with the property

$$D(\boldsymbol{k}) \propto \frac{1}{k^2 G(t)} \quad , \tag{3.2}$$

where $G(t) = \sqrt{G_x(t)^2 + G_y(t)^2 + G_z(t)^2}$ is the gradient magnitude. By considering hardware constraints, the solution for the gradient waveform can be found to be [Nagel et al., 2009]

$$G(t) = k_0^2 G_0 (3\gamma k_0^2 G_0 (t - t_0) + k_0^3)^{-2/3} \quad . \tag{3.3}$$

Here, k_0 is the k-space radius at which the sampling-density adapted acquisition can start after measuring the center with constant amplitude G_0. The time at which the adapted trajectory starts is t_0 and the maximum gradient amplitude G_0 is determined by the desired resolution. A sketch of the gradient shape is shown in the sequence diagram in **Figure 3.4**. The full k-space volume is covered subsequently by sampling from the center towards endpoints, which are distributed over a spherical surface following the algorithm of Rakhmanov et al. [1994]. This is shown for 50 spokes in **Figure 3.5**. The minimal echo time (TE_{min}) which can be achieved is constrained by the pulse length and the ring-down time of the RF coil after the excitation pulse. It is defined defined as half of the duration of the excitation pulse plus a delay time (50 µs) to allow for ring-down The duration of the sampling with a trapezoidal gradient was set to $t_0 = 0.5$ ms for all measurements in this work.

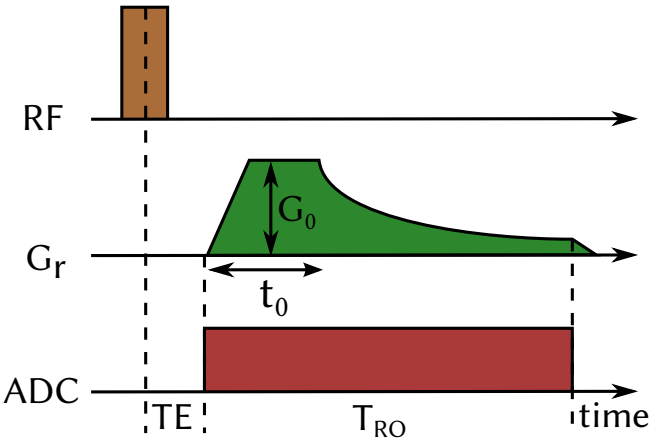

Figure 3.4: Readout scheme of the DA 3D-RAD sequence. The gradient magnitude G_r decreases towards the k-space periphery in order to sustain a constant sampling density. Due to hardware limitations, this gradient form can only start at times later t_0.

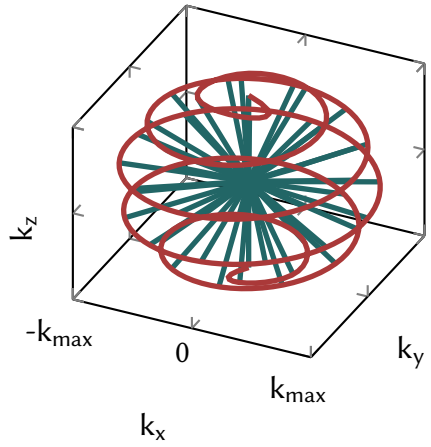

Figure 3.5: Schematic for the k-space coverage in the employed radial sampling scheme. The readout spokes are distributed successively along a spiral on the sampling surface at k_{max} [Rakhmanov et al., 1994].

Multi echo readout scheme In order to spatially resolve the T_2^* relaxation, the signal decay had to be sampled in the temporal domain at multiple time points TE_i. To this end, the DA 3D-RAD sequence was extended by additional rewinder gradients allowing for a multi echo acquisition (cf. **Figure 3.6**). The temporal amplitude integral of the rewinder is identical to the one of the preceding readout gradient but with inverted polarity. Thus, the phase which is acquired during the readout is reverted and a sampling point at the end of the rewinder is located again in the k-space center. The implementation used in this work allowed the acquisition of eight echoes and echo times TE could be set within an accuracy of 0.01 ms if $TE < 10$ ms and 0.1 ms if $TE \geq 10$ ms. This restriction was given by the scanner's interface.

Anatomical Sequences For the purpose of tissue segmentation, two anatomical ^{1}H pulse sequences, namely the MPRAGE for the segmentation and a CISS to improve brain extraction. The MPRAGE (magnetization prepared rapid acquisition gradient echo) proposed by Mugler and Brookeman [1990] is a fast 3D readout with pronounced contrast between GM and WM, which renders it especially suitable for the purpose of tissue segmentation. The distinct contrast of this readout scheme is determined by an inversion pulse followed by a fast 3D gradient echo (GRE) readout and a magnetization recovery period leading to a T_1-weighted contrast. Even though the liquid suppression is strong in the MPRAGE, an additional T_2-weighted pulse sequence was acquired for the brain extraction (cf. Section 3.3.3). A CISS (constructive interference in steady state) was chosen due to the strong T_2 contrast [Besta et al., 2015]. This sequence is a steady-state free precession scheme with reduced banding artifacts from B_0 inhomogeneities typical for steady-state free precession sequences. Two separate acquisitions with different RF-cycling schemes are averaged and thereby these artifacts can be reduced.
An impression of the image contrast obtained by these sequences is given in **Figure 3.7**. In the MPRAGE measurement WM and GM can be clearly distinguished. However, brain parenchyma and skull are not always separated in their image intensity. In the CISS acquisition, a continuous signal void can be acknowledged. In the frontal region, typical banding artifacts are visible.

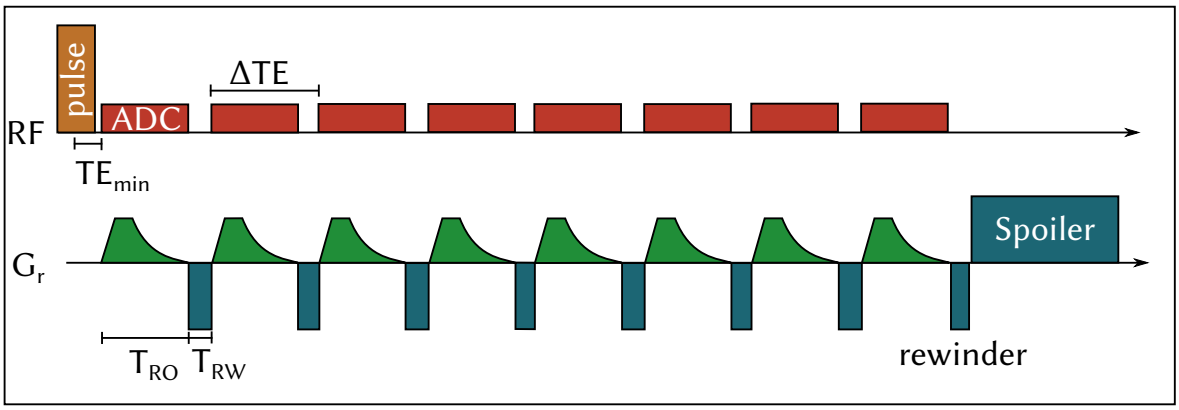

Figure 3.6: Pulse sequence diagram of the multi-echo acquisition scheme. The radial readout trajectory of duration T_{RO} was repeated eight times with a rewinder gradient of duration T_{RW} interleaved. The echo spacing is $\Delta TE = T_{RO} + T_{RW}$. The echo time ΔTE_{min} of the first acquisition is defined as half of the pulse duration plus an RF ring-down time of 50 µs.

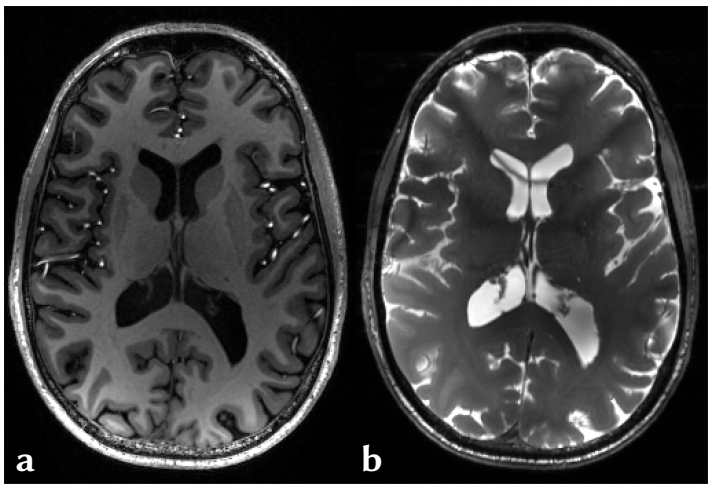

Figure 3.7: Example data of anatomical ^{1}H sequences: MPRAGE (a) and CISS (b). WM and GM can be clearly distinguished in the MPRAGE acquisition. Brain parenchyma and skull are not continuously separated in image intensity. In the CISS data, skull can be clearly separated. Banding artifacts are visible as dark stripes.

3.1.2 Image reconstruction

In this section, the image reconstruction for the cases of radial k-space data and multi-channel coils is explained.

Non-Cartesian reconstruction

For Cartesian k-space sampling, the raw data can be transformed to image space in a straightforward manner by the application of the FFT [Cooley and Tukey, 1965]. For the radial trajectories used here, a direct evaluation of the Fourier coefficients would be of order $O(N^2)$ operations in comparison to the FFT being $O(N \log N)$. To this end, practical implementations prefer an interpolation of the non-Cartesian data onto a regular grid prior to a application of the FFT. This is sometimes also termed *gridding*. An efficient, accurate, and convenient implementation is the non-uniform fast Fourier transformation (nuFFT) by Fessler and Sutton [2003].
In more detail, a non-Cartesian readout determines the MRI signal $S(\boldsymbol{k}_m)$ at k-space positions $\boldsymbol{k}_m$. For the interpolation onto a Cartesian grid, the following operation has to be evaluated

$$S(\boldsymbol{k}_n) = \sum_{n=1}^{N} v_{n,m} S(\boldsymbol{k}_m) \quad . \tag{3.4}$$

Here, n designates the index enumerating the set of points on a Cartesian grid from 1 to N and likewise the number of radial points are designated by $m = 1, \ldots, M$. For the presented application typically $M > N$ without further implications. The interpolation process is depicted in **Figure 3.8**. The values of $\boldsymbol{v}$ are determined by the chosen interpolation kernel. The ideal kernel is the sinc-function and would span the full matrix size N. For efficiency reasons, this range can be reduced to a neighborhood of width W. A widely used interpolation function is the Kaiser-Bessel window [Rasche et al., 1999]. In the implementation of Fessler and Sutton a so-called min-max approach is applied which further reduces interpolation errors.

Image reconstruction for multi-channel data

For a multi-channel acquisition, the data from each separate channel have to be combined into one image. Here, it has to be considered, that the SNR may vary over the object dependent on the coil profiles and their location relative to the object. Furthermore, the data of different channels is correlated in both signal and noise. Two approaches were used in this work: the sum-of-squares combination and the adaptive channel reconstruction, which are explained in the following.

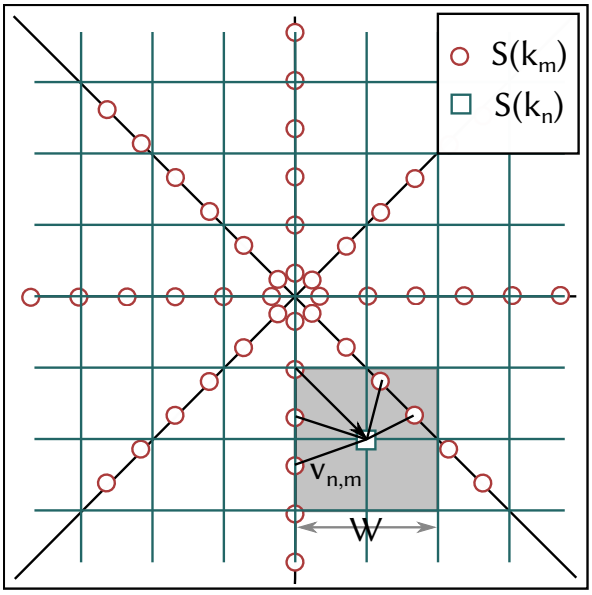

Figure 3.8: Schematic of the gridding process. Data from the non-Cartesian sampling (red) are interpolated onto points on a Cartesian grid (green) by weighting with the filter coefficients $v_{n,m}$ inside a window of width W.

Sum-of-squares combination The sum-of-squares (SOS) reconstruction is a simple method for combining multi-channel data. The combined image I_{comb} is obtained by voxel-wise summation of the squared image intensity from the N separate channels I_i

$$\boldsymbol{I}_{\text{comb}} = \sqrt{\sum_{i=1}^{N} \boldsymbol{I}_i^2} \quad . \tag{3.5}$$

Here, the spacial dependence of the image intensity $I = I(x, y, z)$ is omitted for clarity. In the SOS combination, voxels with high intensity are implicitly assumed to stem from regions with high coil sensitivity and contribute stronger to the final image. This is a suitable approach for sufficiently high SNR and in regions of signal [Larsson et al., 2003]. However, for poor SNR and noise regions it leads to noise amplification.

Adaptive combination The adaptive combination (AC) proposed by Walsh et al. [2000] allows taking into account the coil profiles and the noise correlation between data from separate channels. Thereby, a reconstruction with near-optimal SNR behavior is possible [Roemer et al., 1990]. The image is formed by a linear combination of the separate image reconstructions which are locally scaled by the complex weighting factors $\boldsymbol{m}_i$. Thus, the finale image is determined by

$$\boldsymbol{I}_{\text{comb}} = \sum_{i=1}^{N} \boldsymbol{m}_i \boldsymbol{I}_i \quad . \tag{3.6}$$

The linear combination has the advantage of retaining the signal phase in contrast to the SOS approach.

The weighting factors are determined by an analysis based on stochastic signal theory. It can be found that the vector, which optimizes the SNR of the final image $\boldsymbol{I}_{\text{comb}}$, is determined by the signal and noise correlation of the individual channels. Denoting the signal correlation by $\boldsymbol{R}_s$ and the noise correlation by $\boldsymbol{R}_n$, the vector $\boldsymbol{m}$ is determined by the highest eigenvalues of the matrix $\boldsymbol{R}_n^{-1}\boldsymbol{R}_s$. The signal correlation can be estimated from a block-wise covariance analysis of the image data from each coil using

$$\boldsymbol{R}_s(i,j) = \sum_{\text{Block}} \boldsymbol{I}_i \boldsymbol{I}_j^* \quad . \tag{3.7}$$

The indexes i and j run over the N coil elements. The receive profiles are accounted for by stronger weighting of channels with a higher local SNR. The noise correlation can be determined by a covariance analysis of either the image data or, prior to the reconstruction, from raw data. Therefore, a noise scan is acquired by setting the amplitude of the excitation pulse to zero. The combination parameters used in this work are listen in **Table 3.1**. These values were reported previously by Benkhedah et al. [2016] for the application in ^{23}Na MRI.

3.2 Techniques for the observation of the T_2^* decay

The main goal of this work was to improve the accuracy of T_2^* quantification for ^{23}Na MRI in vivo. In this section, the basic techniques are described which were used for the determination of the decay parameters. First, the employed signal model is established together with different approaches to incorporate noise bias in the data. Then, an optimization procedure is described, which was developed in order to tailor the sampling scheme with respect to the low SNR and rapid biexponential decay of the ^{23}Na signal.

3.2.1 Signal model and decay parameter fitting

The two relaxation times $T_{2,\text{s}}^*$ and $T_{2,\text{l}}^*$ of the biexponential signal decay were determined by voxel-wise fitting of image data acquired with a multi-echo pulse sequence (cf. Section 3.1.1).

Table 3.1: Parameters for AC channel combination. These parameters were reported previously by Benkhedah et al. [2016].

Parameter	Value
block size	8
interpolation factor	2
prefiltering	Gauss with $\sigma = 2$ voxels

A biexponential decay model following from the signal theory of ^{23}Na MRI in biological tissue was fitted to the data (cf. Section 2.1.4). The general form of the model is

$$S(A_0, T_{2,\mathrm{s}}^*, T_{2,\mathrm{l}}^*, n) = \sqrt{A_0^2 \left(r\mathrm{e}^{-TE/T_{2,\mathrm{s}}^*} + (1-r)\mathrm{e}^{-TE/T_{2,\mathrm{l}}^*} \right)^2 + n^2} \ . \tag{3.8}$$

The signal amplitude measured in a voxel at position $\boldsymbol{x}$ is denoted by S. The spatial dependence is omitted for clarity. A_0 is the apparent magnetization which comprises the spin-density ρ, T_1 relaxation, the excitation, and other contributions (cf. Section 2.2.3). The percentage of the signal decaying with $T_{2,\mathrm{s}}^*$ is denoted by r and is set to $r = 0.6$ as follows from ^{23}Na interaction theory. The additional parameter n expresses the magnitude bias due to noise (cf. next section).

Models for the incorporation of the noise bias The non-zero mean of the Rician distribution has to be taken into account when fitting low-SNR magnitude data (cf. Section 2.2.4). Three possible formulations for the parameter n in Equation 3.8 where investigated. These are

(1) including a constant predetermined Rician noise floor by setting $n = \sqrt{(2-\pi/2)}\sigma$ as described by Gudbjartsson and Patz [1995]

(2) determination of the noise amplitude n by fitting

(3) ignoring the noise contribution ($n = 0$)

In the models (1) and (3) a constant term is used to take noise into account whereas model (2) requires an additional fitting of this parameter.
All fit models were evaluated with regard to varying noise amplitude (SNR = 10/15/20). Furthermore, the fit quality was investigated as function of the number of samples acquired because it might be beneficial to sample the decay until late TE for more accurate measurement of $T_{2,\mathrm{l}}^*$. This however, can also increase noise bias since later samples exhibit lower SNR. Assuming an equidistant sampling scheme, the total number of samples can be parametrized by the latest sample at $TE_{\max}$, which is determined by TR. For the evaluation, signal was synthesized with $T_{2,\mathrm{s}}^* = 5$ ms and $T_{2,\mathrm{l}}^* = 40$ ms and an increasing number of sampling points spaced with $\Delta TE = 5$ ms from $TE_{\max} = 20$ ms to 150 ms. Thus, the number of sampling points ranged from 5 to 30.

Non-linear least squares fitting The parameter fitting was performed using the non-linear least squares (NLLS) method. The parameters β of the model f_β are determined by minimization of the sum of the squared deviations Φ between model and the measurement y at point x for all N observations according to

$$\arg\min_{\beta} \Phi \quad \text{with} \quad \Phi = \sum_{i=1}^{N} (f_\beta(x_i) - y_i)^2 \tag{3.9}$$

as proposed by [Legendre, 1805] and [Gauss, 1809]. The minimization of the objective function was executed with a trust region method [Coleman and Li, 1994, 1996] implemented in MATLAB (The MathWorks, Inc., Natick, Massachusetts, USA).

3.2.2 Optimization of the temporal sample distribution for T_2^* measurements

A factor which impacts the quality of a decay measurement is the distribution of sampling points on the curve, i. e. the form of the temporal sampling. For an accurate and efficient parameter estimate, the sampling scheme should match the decay and SNR situation. To this end, an approach was designed to evaluate different sampling schemes on the basis of one single quality measure including bias and uncertainty for all model parameters. Using this metric, a dedicated sampling pattern was designed for ^{23}Na T_2^* quantification in human brain. This process is described in more detail in the following section.

Development of a dedicated sampling strategy

Sampling strategies from ^{1}H MRI cannot be directly translated to ^{23}Na MRI due to the lower SNR and the short T_2^* compared to the readout duration T_{RO}. For ^{23}Na T_2^* sampling, multiple echoes are acquired after each excitation pulse. These samples are distributed with a temporal spacing of at least ΔTE_{min}. The minimal echo spacing of the multi-echo scheme used in this work is the sum of the duration of the readout T_{RO} and the rewinder gradient ($\Delta TE_{min} = T_{RO} + T_{RW}$). However, to be able to resolve short $T_{2,s}^*$, a finer temporal sampling is required. This is realized by repeating the echo train with the first sampling point shifted to a later TE (cf. **Figure 3.9**).
For ^{23}Na MRI, SNR is the crucial limitation (cf. Section 2.1.5) and all available signal energy should be exploited. For SNR efficiency, dead times should be avoided since during these

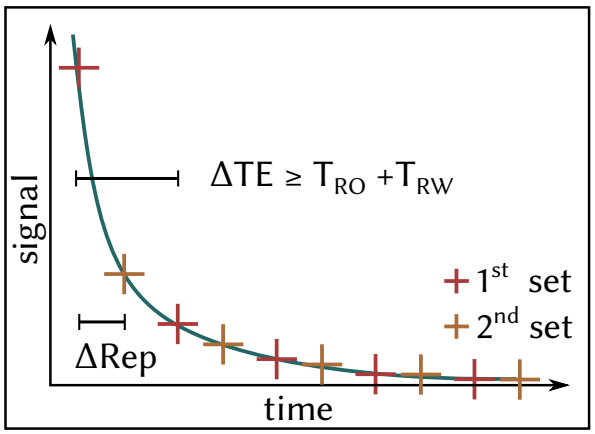

Figure 3.9: Schematic of T_2^* sampling in ^{23}Na MRI. A decay curve is shown with symbolic sampling times TE_i. Due to the time required for the readout (T_{RO}) and the rewinder (T_{RW}) a minimal spacing between two samples (ΔTE) is required (red). A finer temporal sampling can be achieved by an additional acquisition shifted by ΔRep (orange marks).

signal energy is lost. Thus, within one *TR* successive sampling points were acquired immediately after the previous readout separated by ΔTE_{min}. This leads to a base pattern of N_{Echoes} equidistant samples, which was repeated N_{Reps} times with a shift ΔRep_i relative to the first acquisition (cf. **Figure 3.9**). The first point in the first set was acquired at the earliest *TE* possible (ideally $TE_1 = TE_{\text{min}} = 0\,\text{ms}$) since this yields the highest SNR. For this type of sampling scheme, the distribution of all samples can be solely parametrized by the shifts ΔRep_i. The repetition of an equidistant sampling train compared to an arbitrary distribution of all sample points reduces the degrees of freedom from $N_{\text{Reps}} \cdot N_{\text{Echoes}}$ down to $N_{\text{Reps}} - 1$. The parametrization via the ΔRep_i allows tuning the sampling scheme to the optimal trade-off between reliability and accuracy for a given decay and SNR. For example, higher reliability can be achieved by averaging ($\Delta\text{Rep}_i = 0\,\text{ms}$) or a better temporal resolution by denser sampling (e.g. linear sampling with $\Delta\text{Rep}_i = \Delta TE/N_{\text{Reps}} \cdot (i-1)$).

The base sampling scheme consisting of 8 echoes. Sequence parameters were adjusted to achieve an SNR of approximately 15 in brain parenchyma since this was determined to be the minimum requirement for the parameter fitting of the biexponential model (cf. Section 4.1.2). Thereby, the spacing ΔTE is determined by the sequence parameters (detailed sequence parameters in Section 4.2.1). The acquisition time was constraint to one hour, which is assumed to be tolerable with regard to in vivo applicability. Within this time, $N_{\text{Reps}} = 4$ repetitions could be acquired determined by the measurement parameters. Therefore, the following optimization was conducted for 4 shifts ΔRep_i.

Quality metric for parameter estimation

The evaluation of the fitting quality for the biexponential decay is ambiguous since multiple model parameters exist. To this end, a single evaluation measure was designed, which captures the most important fit criteria. For the low-SNR signal of ^{23}Na MRI, these are namely the deviation of the parameter estimate from the true value (bias) and the variation due to noise (uncertainty). To establish a single quality measure, the metric Q was defined which incorporates both criteria as follows.
If the same underlying parameter i with the true value X_i is measured over a volume of voxels, the bias is expressed by the deviation of the measured mean value over this set $\bar{X}'$ from X_i. The uncertainty can be judged by the magnitude of the standard deviation of the set of parameter estimates $\sigma(X_i')$. Therefore, the quality Q of the estimate was defined to be the sum of the relative bias scaled by the relative standard deviation over all parameters

$$Q = \sum_{i=1}^{3} \left(\frac{\sigma(X_i')}{X_i} \cdot \frac{\bar{X}_i' - X_i}{X_i} \right)^2 \quad . \tag{3.10}$$

The index i runs from 1 to 3 representing the amplitude A_0, $T_{2,\text{s}}^*$, and $T_{2,\text{l}}^*$. The contribution of each model parameter is squared in order to penalize strong bias and improve smoothness of the metric. Thus, a larger Q indicates a reduced overall quality of the parameter estimation.

The shape of Q for different values of bias and standard deviation is visualized in **Figure 3.10** for a single parameter i.

Design of the optimization

The metric Q is a function of the sampling scheme and an optimization problem can be formulated to minimize Q with regard to the shifts ΔRep_i. To determine Q, the following procedure was conducted. First, signal was simulated with decay constants of $T^*_{2,\text{s}} = 5\,\text{ms}$ and $T^*_{2,\text{s}} = 40\,\text{ms}$ as reported for brain parenchyma with 60 % amplitude stemming from the short component [Nagel et al., 2011; Bydder et al., 2017]. Then, Gaussian noise scaled for an SNR of 15 was added. By calculating the absolute value, a Rician noise distribution was obtained [Gudbjartsson and Patz, 1995]. From this data, the parameter estimates X'_i were determined via fitting. This process was repeated $N = 30{,}000$ times to sample the fit statistics sufficiently accurate. Q was then calculated from the fit results by Equation 3.10. The full process is depicted in **Figure 3.11**. The fit parameters were initialized with 1, 3 ms and 30 ms (A_0, $T^*_{2,\text{s}}$, and $T^*_{2,\text{l}}$) and were loosely constraint to the intervals [0,10], [0,100] ms and [0,100] ms, respectively. The constraints of the fit were deliberately set to a wide parameter region to not constrain the problem with any prior knowledge not existing in the in-vivo situation. The minimization of Q was performed numerically using a multi-start approach described in more detail in the next section.

Global optimization algorithm

The shape of the parameter space of Q as a function of the shifts ΔRep is not known and convexity cannot be assumed. For this reason, a global search approach was chosen. The minimization was conducted with a multi-start heuristic algorithm presented by Ugray et al. [2007]. The procedure constitutes of two main phases: (1) a global phase and (2) a local phase. In the first phase a *scatter search* algorithm [Glover, 1998] is employed to sample the objective function on a global scale and to provide good candidates for the second phase. The second phase then runs a gradient based solver on the initial points to find the global minimum. In the following these two phases are outlined in more detail.

1 Global Phase: Scatter search The so called scatter search iterates through the following steps:

(a) Input of a seed solution x_0 and creation of additional starting points which lie at the upper and lower problem boundaries and on the midpoint in between.

(b) A *diversification generator* creates a larger set of new trial points. The generator introduces new points in a region spanned by two neighboring trial points by distributing random points over this region. If these points do not fulfill the problem conditions, they are mapped towards the nearest point within the boundaries. A new trial point

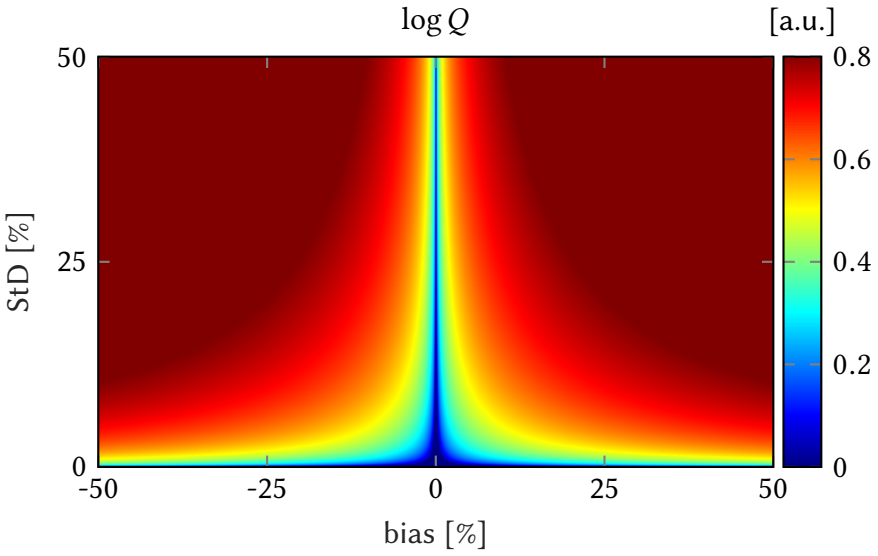

Figure 3.10: Quality metric Q for varying bias and uncertainty for single parameter i (cf. Equation 3.10). The standard deviation (StD) ranges from 0 % to 50 % and the bias from −50 % to 50 % (under- to overestimation). For a better visualization the logarithm of Q is shown. The strong decrease of Q towards low bias and standard deviation can be acknowledged.

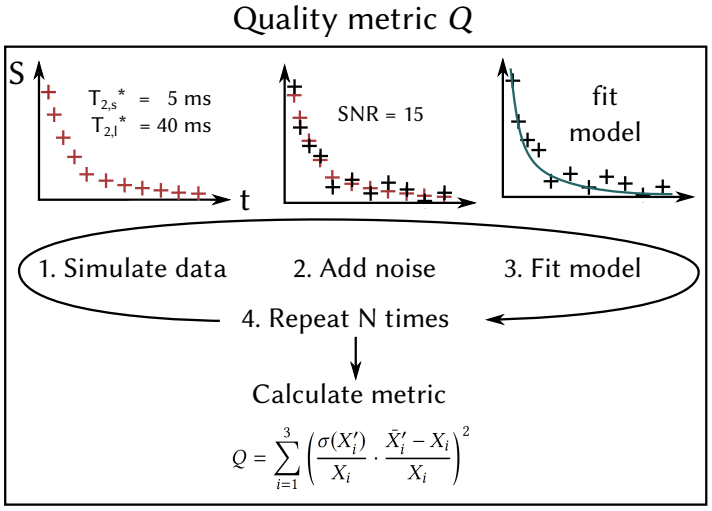

Figure 3.11: Visualization of the quality metric Q as determined in the optimization. The following process is repeated N times: (1) biexponential decay data are calculated at the times determined by the sampling scheme, (2) Rician noise is added, and (3) fit of the model parameters.

is then chosen as the point being located the farthest aways from all preexisting neighbors.

(c) The points retrieved by step (b) are rated by a penalty function consisting of the objective function and an additional weight for constraint violation. Non-promising candidates are discarded.

(d) The preceding steps are repeated until a designated number of trial points is reached.

2 Local Phase: Gradient-based optimization In this phase the gradient based solver is started iteratively from promising candidates determined in phase 1. These points are retrieved by two filters. The first filter is called a *distance filter*. It makes sure that points close to previous evaluations are are not considered multiple times. The second filter is a *merit* filter, which compares local solutions to previous results in the database. If the solution does not pass a threshold of the penalty function it is discarded.

For the minimization in this work, the algorithm was started on the linear scheme as the seed solution x_0. This pattern is considered to be the most neutral in terms of weighting towards a specific model parameter. Furthermore, 50 initial points were allowed. The evaluation of Q was split up to run in parallel on 16 cores on PC2 (cf. Section 3.1.1). The local gradient-based solver used in the implementation of the algorithm is MATLAB's *fmincon*.

Comparison to alternative sampling schemes

The sampling pattern retrieved from the optimization procedure was compared to four alternative sampling schemes (**Figure 3.12**). These were a *linear* scheme, an *early TE* pattern, the pattern by *Jones et al.*, and simple *averaging*. The *linear* pattern (a) was chosen to investigate a "neutral" pattern without focus on a specific decay time. The *early TE* scheme (b) is an example for a pronounced focus on the resolution of $T^*_{2,\mathrm{s}}$. The scheme of *Jones et al.* [Jones et al., 1996] (c) is an optimized solution for the problem of sampling a monoexpontial decay. This pattern was adapted to the presented parametrization by setting $T_2 = T^*_{2,\mathrm{s}} = 5\,\mathrm{ms}$ in order to focus on the short component $T^*_{2,\mathrm{s}}$. The *averaging* pattern (d) only focuses on the aspect of improving the reliability of the parameter estimation. In a real measurement, all shifts are delayed by the TE_{min} (cf. Section 3.1.1). Example image reconstructions of the linear pattern are shown in **Figure 3.13**. The respective shifts $\Delta\mathrm{Rep}_i$ of each pattern are given in **Table 3.2**.
For the comparison, biexponential decay data were simulated with SNR = 10/15/20/40 and N = 100,000 repetitions. Accuracy and parameter uncertainty were investigated over a range of T^*_2 values. $T^*_{2,\mathrm{s}}$ and $T^*_{2,\mathrm{l}}$ ranged from 0 ms to 20 ms and from 20 ms to 60 ms, respectively. For $T^*_{2,\mathrm{s}} = 0\,\mathrm{ms}$ the smallest 64-bit number $\epsilon = 2^{-53} \approx 2.2 \times 10^{-16}$ was set.

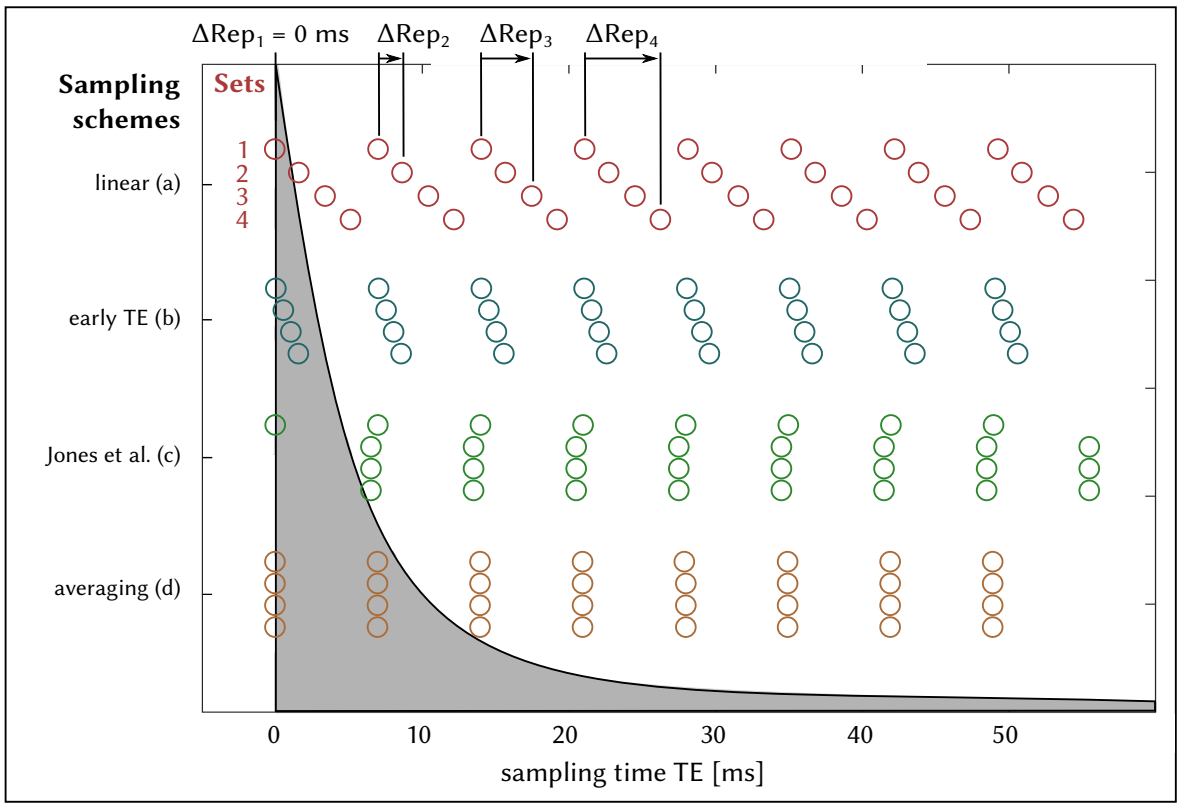

Figure 3.12: Overview of the alternative sampling schemes under investigation. A typical decay curve for brain parenchyma with $T_{2,s}^* = 5\,\text{ms}$ and $T_{2,l}^* = 40\,\text{ms}$ is shown (gray). The repetition number of the base pattern (1–4) and the respective shifts ΔRep_i are depicted in the linear pattern (a). The ΔRep_i are given in Table 3.2. See Figure 3.13 for an example image data set of the linear scheme.

Table 3.2: Timings of the alternative sampling schemes. Each pattern is completely described by the ΔRep_i, which denote the shift of each equidistant sampling block relative to the earliest point at TE_{min}. For the pattern of Jones et al. $T_2 = 5\,\text{ms}$ was assumed.

sampling scheme	**ΔRep_i [ms]**
linear	0.00, 1.75, 3.50, 5.25
early TE	0.00, 0.50, 1.00, 1.50
Jones et al. [1996]	0.00, 6.50, 6.50, 6.50
averaging	0.00, 0.00, 0.00, 0.00

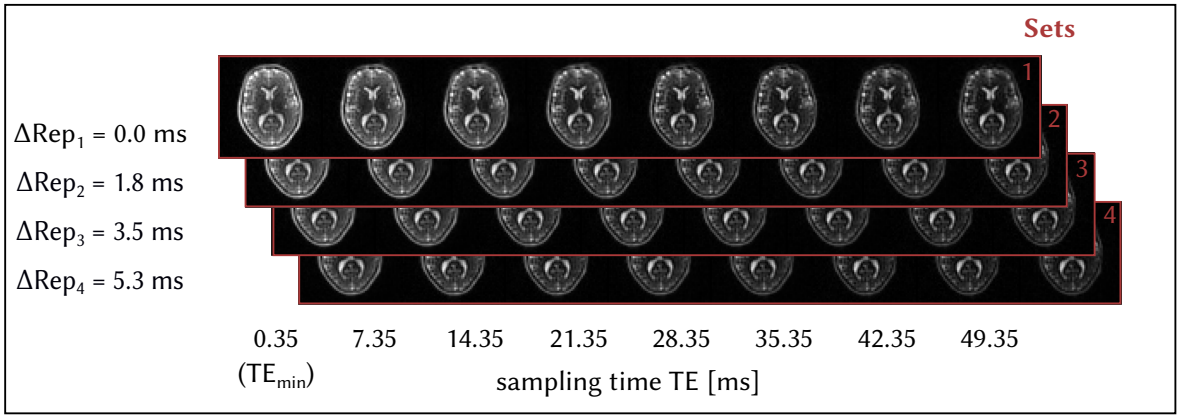

Figure 3.13: Example image data of a healthy volunteer using the linear sampling scheme. Four acquisition sets are shown with increasing shifts ΔRep_i (1–4).

3.3 Additional procedures

For the characterization of the novel 30-channel array coil and the in vivo evaluation of the T_2^* data, additional methods were required which are described in the following. These are SNR measurement techniques, B_1 mapping, and segmentation algorithms.

3.3.1 Measurement of the signal-to-noise ratio (SNR)

The SNR is a measure for the uncertainty of a data point with respect to the expected variance due to noise. For MRI, the SNR in the image space is of interest even though data is acquired in the Fourier domain of this image. Special care has to be taken when analyzing the SNR in the image space since the reconstruction process can influence the apparent SNR. Examples leading to such alterations are the calculation of a magnitude image from the complex-valued data [Gudbjartsson and Patz, 1995], parallel imaging [Dietrich et al., 2007], or non-linear reconstruction such as compressed sensing [Lustig et al., 2007].

Region-of-interest approach A simple estimate of the image SNR can be retrieved from the ratio of the mean signal S_0 in a region of interest (ROI) in the object and the standard deviation σ' in a noise ROI (cf. [Haacke et al., 1999], Sec. 15.1.5). For noise signal in amplitude images, the Rician distribution is equivalent to the Rayleigh distribution (cf. Section 2.2.4). The observed variance σ' of the noise can be corrected to the true standard deviation σ of the underlying Gaussian distribution with the relation

$$\sigma' = \sqrt{2 - \frac{\pi}{2}}\sigma \approx 0.66\sigma \quad . \tag{3.11}$$

Thus, the SNR can be determined via

$$\mathrm{SNR} = \frac{S_0}{\sigma} \approx 0.66 \cdot \frac{S_0}{\sigma'} \quad . \tag{3.12}$$

The advantage of this approach is its' ease in use. However, it cannot be applied anymore for nonlinear reconstruction techniques such as the SOS channel combination.

Pseudo multiple replica approach A more robust method for the SNR determination is the pseudo multiple replica approach [Robson et al., 2008; Dietrich et al., 2007], which allows to determine the SNR on a pixel basis. Multiple reconstructions of the raw data are performed. Prior to every Fourier transform, white Gaussian noise scaled to the actual measurement noise is added. The SNR of each pixel is then determined by the ratio of the mean and the standard deviation over all reconstructions. The scaling of the synthetic noise is determined through a noise scan which has to be performed in addition to the actual measurement. This method is relatively time intensive due to the many reconstructions which have to be carried out.

3.3.2 B_1 field mapping

Mapping of the B_1^+ excitation field was carried out using the so-called *phase-sensitive* method by Morrell [2008], which has been shown to be an appropriate technique for the low SNR of ^{23}Na [Lommen et al., 2016a]. The excitation field is mapped into the signal phase by the application of a 180°-90° composite pulse. Additional phase contributions are removed by the subtraction of two image reconstructions of data acquired with opposed phase of 0° and 180°. In the case of a Tx/Rx coil, the receive field profile B_1^- can be assumed to have the same spatial distribution by the argument of reciprocity at the ^{23}Na frequency [Hoult, 2000].

For a coil with separate Tx and Rx channel, as is the case for the 30-channel array coil (cf. Section 3.1.1), the sensitivity profile of the Rx unit $B_{1,\mathrm{Rx}}^-$ (e.g. the receive array) can be determined from a B_1^+ map of the Tx unit $B_{1,\mathrm{Tx}}^+$ (e.g. birdcage) and two standard image acquisitions one acquired with the Tx unit S_{Tx} and one with the Rx unit S_{Tx} [Volz et al., 2012]. The excitation field of the image from the Tx unit and the Rx unit are equivalent ($B_{1,\mathrm{Tx}}^+$) since excitation is only performed by the Tx unit. The object specific structure is removed by the ratio of images from both units. To this end, the receive profile can be determined by

$$B_{1,\mathrm{Rx}}^- = \frac{S_{\mathrm{Rx}}}{S_{\mathrm{Tx}}} \cdot B_{1,\mathrm{Tx}}^+ \quad . \tag{3.13}$$

3.3.3 Registration and segmentation

For the purpose of tissue segmentation, image registration, tissue segmentation, and brain extraction were carried out using the FMRIB software library (FSL). FSL is a collection of analysis tools developed for the purpose of functional MRI imaging. In this work the following tools were employed:

FLIRT The FLIRT (FMRIB's linear image registration tool) algorithm allows the registration of images from different image modalities by a diverse set of rigid and affine transformations [Jenkinson and Smith, 2001; Jenkinson et al., 2002]. During this work, the capability of intra-modal registration was useful for the registration of ^{1}H and ^{23}Na image data. It was found to be beneficial for the process to smooth ^{23}Na images prior with either a Gaussian or a Hamming filter. The result of the registration was found to be strongly dependent on the image data and the chosen cost function, which often require individual adjustment in order to obtain satisfying results.

BET BET (brain extraction tool) allows the extraction of the brain from surrounding skull and scalp tissue [Smith, 2002]. This is a necessary step prior to the tissue segmentation based on image intensity.

FAST The FAST (FMRIB's automated segmentation tool) algorithm allows fully automated tissue segmentation with optional bias field removal. The method is based on a hidden Markov random field model combined with a expectation-maximization algorithm [Zhang et al., 2001]. The algorithm was set to segment three tissue types: white matter (WM), gray matter (GM), and cerebrospinal fluid (CSF).

4 Results

In the following chapter, the main results of this thesis are presented. First, improved SNR efficiency by means of a multi-channel receive array is shown. Then, an optimized sampling scheme for the purpose of ^{23}Na T_2^* measurement is given and compared to alternative patterns. The influence of noise in the parameter fitting is analyzed for three signal models. Finally, spatially resolved in vivo T_2^* maps are presented, and from these data the correlation time of the interaction of ^{23}Na ions in brain tissue is estimated.

4.1 Methodical development for T_2^* determination

In this chapter, the methodical developments are presented which eventually lead to a spatially resolved measurement of ^{23}Na T_2^* in the human brain in vivo. First, the increased SNR performance of the novel 30-channel array coil is characterized and compared to a standard birdcage radio frequency coil. Then, an optimized distribution for the temporal sampling points is shown. This pattern is compared to common alternatives over a range of relaxation times and SNR. Furthermore, systematic influences due to the fitting model are investigated.

4.1.1 Improved SNR efficiency by means of a multi-channel coil

The use of multi-channel RF coils allows a higher SNR efficiency compared to volume coils such as birdcage resonators [Roemer et al., 1990]. The improvements in image SNR which could be achieved by utilization of the 30-channel array coil (cf. Section 3.1.1) are demonstrated in the following sections. First, important coil characteristics such as noise correlation and B_1 transmit and receive fields are determined. Then, a quantitative SNR comparison of the novel coil and a standard reference are given. Parts of this work were presented at the Annual Meeting of the ISMRM 2016 [Lommen et al., 2016b].

Noise correlation and field profiles

On the ^{23}Na frequency, the 30-channel array coil is built up from a Tx birdcage and a nested array of 30 separate Rx channels. For the purpose of localization and shimming, an additional ^{1}H birdcage is fit around the ^{23}Na unit. In **Figure 4.1** separate image reconstructions are

shown for each channel in axial and coronal view to give an impression of the channel locations and the individual sensitivity profiles of the separate channels. As can be seen, the image quality is not similar for all channels. The channels 18 and 28, which are located at the top of the head, exhibit higher noise amplitude. The sensitive depth of most channels appears to be larger than the radius of the array. E.g. for channels 6, which is located left of the head in **Figure 4.1** (A), still the complete ventricle and the border between the hemispheres are visible.
The noise correlation between the single channels was calculated from a radial acquisition with 1,000 projections by setting the voltage of the excitation pulse $V_p = 0\,\mathrm{V}$. This has been reported to be sufficient to sample the noise statistics [Benkhedah et al., 2016]. The noise correlation of the 30-channel coil acquired from a head scan is shown in **Figure 4.2**. The highest correlation is found to be 50 % and the mean is 13 %. The patterns of high correlation for channels 1-6 and around 25 are due to the neighboring positions (cf. **Figure 4.1**).
The transmit field was measured using the so-called phase sensitive approach by Morrell [2008], which was demonstrated to be the most appropriate B_1^+ mapping technique for ^{23}Na MRI [Lommen et al., 2016a]. The receive field of the array coil was determined via the field ratios of Tx birdcage and Rx array (cf. Section 3.3.2). For the single channel birdcage, B_1^+ is assumed to equal B_1^- by the reciprocity. All reconstructions for the B_1 mapping were performed using a 6 mm Gauss filter to increase the base SNR. The resulting field maps are shown in **Figure 4.3**. The excitation and receive fields for both coils are displayed in the same volunteer at equivalent measurement parameters (cf. **Table 4.1**). The comparison of the B_1^+ maps displays similar profiles for both coils. A reduced field strength in the top and bottom regions is seen as is typical for birdcage coils. A slight asymmetry of the field is seen in the axial slice of the 30-channel coil. The difference in excitation strength was evaluated by the ratio of the field strength in two ROIs left and right of the center. A difference of about 7 % in field strength was observed. The array coil exhibits a lower B_1 efficiency as seen from the ratio of the reference voltages for a 90° flip angle ($V_{\mathrm{Ref,30}}/V_{\mathrm{Ref,BC}} = 390\,\mathrm{V}/294\,\mathrm{V} = 1.3$). If both coils were driven at the same voltage, this would lead to an increased pulse duration of factor 1.3 for the 30-channel coil. The B_1^- receive profile displays a sensitivity increase of more than a factor two from the coil center towards the brain periphery.

SNR comparison between birdcage and 30-channel array coil

The novel multi-channel receive array was compared to a standard birdcage by the same vendor. To quantitatively compare the SNR in vivo, image data were acquired from one subject with both coils at equivalent acquisition parameters (cf. **Table 4.2**). SNR maps were then determined using the pseudo multiple replica approach (cf. Section 3.3.1). The SNR maps are depicted in **Figure 4.4**. For the 30-channel receiver an improved image SNR can be acknowledged in regions closer to the coil when compared to the birdcage data. The mean SNR was determined in three regions of interest (ROIs) relative to the coil: center, slight offset of the center in a lateral ventricle, and periphery (cf. **Figure 4.4** for the locations).

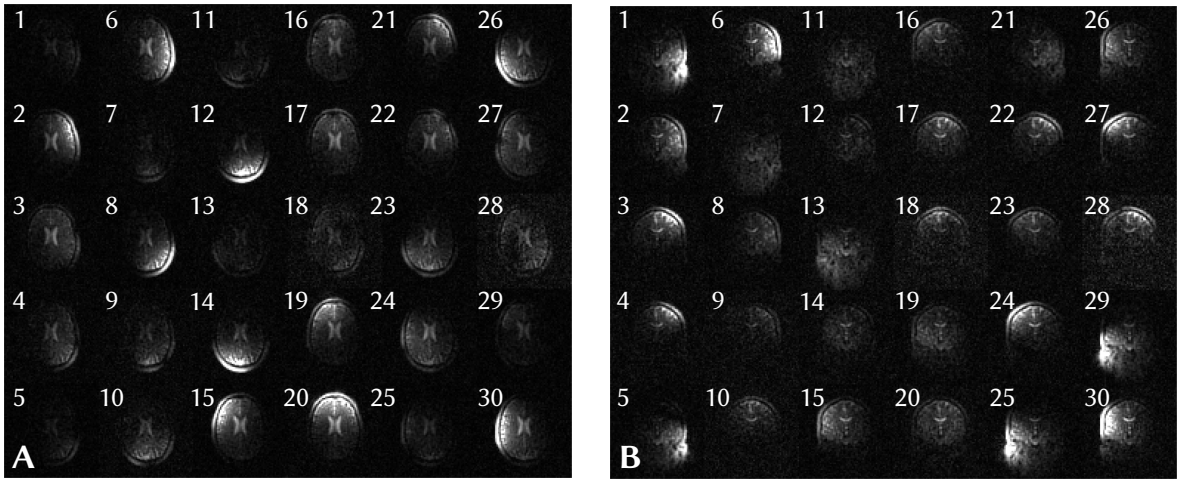

Figure 4.1: Separate channel data of the 30-channel array coil in axial and coronal view. Channels 18 and 28 show highest noise. The sensitive depth of most channels is larger than the radius of the array.

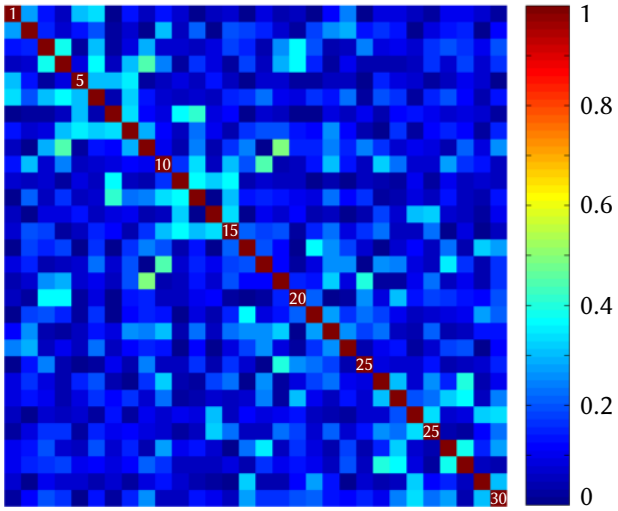

Figure 4.2: Noise correlation matrix of the 30-channel coil. The correlation was calculated from 1,000 projections acquired with pulse voltage $V_p = 0\,\mathrm{V}$. The highest correlation is found to be 50 % and the mean is 13 %. Strongest coupling is found for channel 9 and 19. The patterns of high correlation for channels 1-6 and around 25 are due to the neighboring positions. See Figure 4.1 for their location.

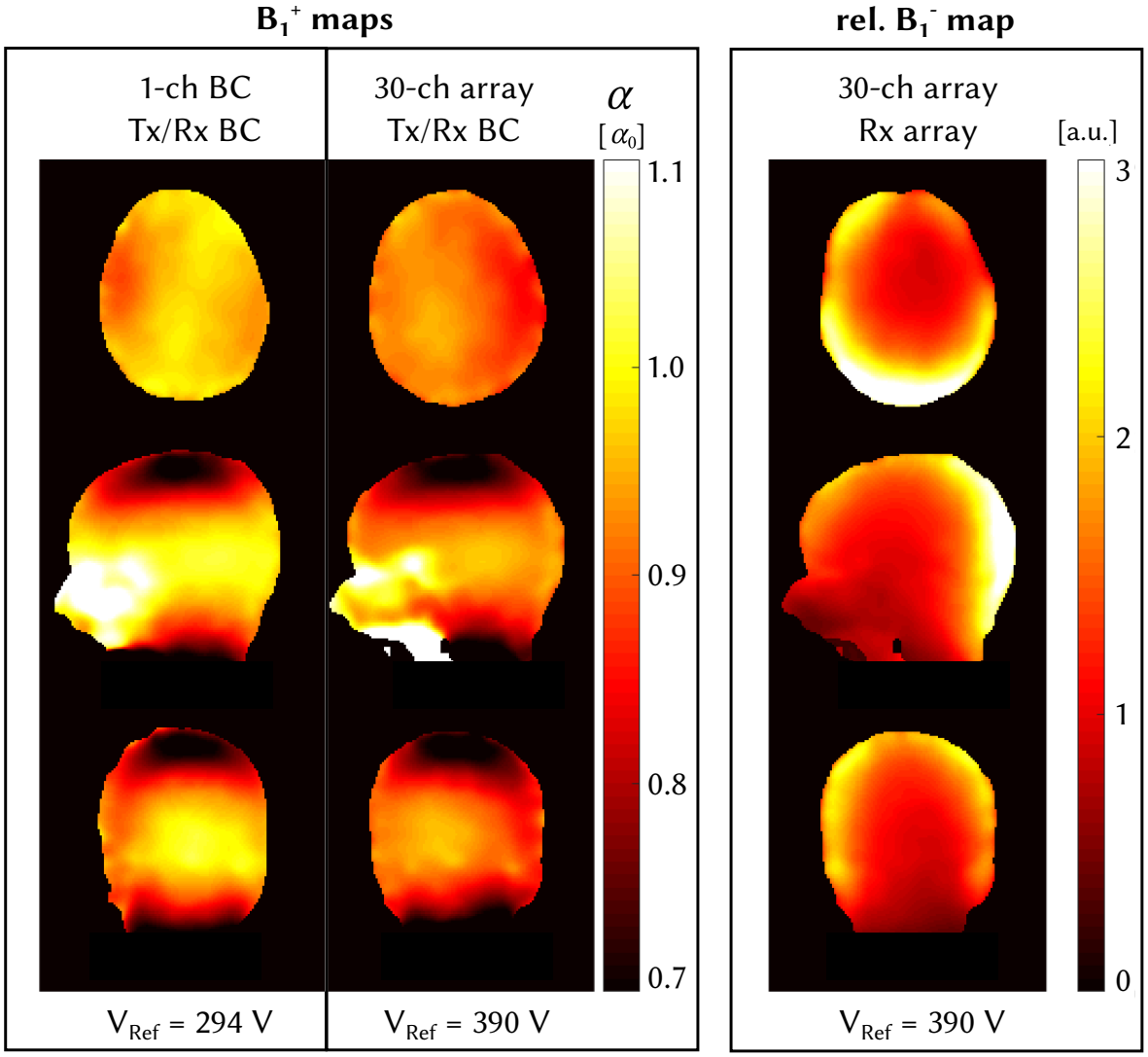

Figure 4.3: B_1 maps of 30-channel array and birdcage coil. B_1^+ maps are normalized to the nominal flip angle (α_0) and B_1^- to the center amplitude. Both coils show similar B_1^+ distribution with highest field strength in the coil center. The birdcage exhibits a higher transmit efficiency as seen in the reference voltages V_{Ref} (bottom). The receive profile of the array exhibits more than twice the sensitivity in the periphery compared to the center.

Table 4.1: Acquisition parameters for the B_1^+ field mapping.

Parameter		**Value**
Sequence		DA 3D-RAD + phase-sensitive excitation scheme
nom. resolution	Δx	4 mm
max. gradient amplitude	G_0	5.87 mT/m
projections	N_{proj}	3,000
radial samples	#RadSamples	384
echo time	TE	0.55 ms
repetition time	TR	150 ms
readout duration	T_{RO}	20 ms
flip angle	α	180°–90°
pulse length	t_p	2000 µs–1000 µs
acquisition time	T_{AQ}	2 × 7:30 min

Table 4.2: Acquisition parameters for the SNR comparison of the 30-channel array and the birdcage coil.

Parameter		**Value**
Sequence		DA 3D-RAD
nom. resolution	Δx	4 mm
max. gradient amplitude	G_0	5.87 mT/m
projections	N_{proj}	10,000
radial samples	#RadSamples	256
echo time	TE	0.35 ms
repetition time	TR	30 ms
readout duration	T_{RO}	10 ms
flip angle	α	53°
pulse length	t_p	600 µs
averages		2
acquisition time	T_{AQ}	2 × 5 min

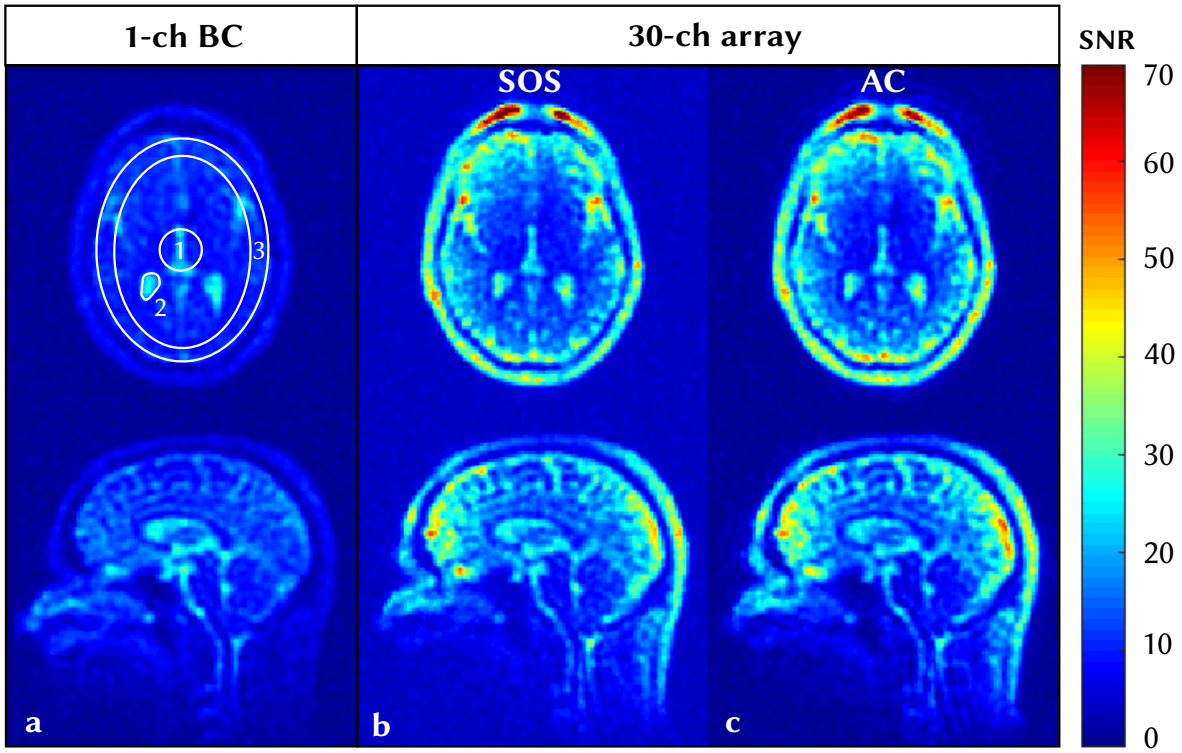

Figure 4.4: In vivo SNR comparison of the 30-channel array coil and the 1-ch birdcage without array. a) Single channel birdcage data, b) SOS channel combination, and c) adaptive combination reconstruction. The 30-channel data exhibit doubled SNR in the brain periphery and similar quality in the center compared to the 1-ch birdcage. The adaptive channel combination results in a further increase of the SNR in areas close to the coils. Mean values in the marked regions (1–3) are given in Table 4.3.

In the periphery the highest difference is expected between the coils and in the ventricle generally highest signal is found due the high concentration in CSF. The mean ROI values are given in **Table 4.3**. The SNR in the periphery was found to be significantly higher for the array coil ($SNR_{30,AC}/SNR_{BC}$ = 2.5). A slight decrease in SNR is apparent in the center region ($SNR_{30,AC}/SNR_{BC}$ = 0.9). However, already in the ventricle located slightly off center an improvement of factor 1.2 is seen.

Table 4.3: Mean SNR values in three brain regions marked in Figure 4.4: center, periphery, and ventricle. The SNR efficiency increases for the 30-channel coil towards the brain periphery as reflected in the ratio $SNR_{30,AC}/SNR_{BC}$.

ROI position	**1-ch BC**	**30-ch** SOS	**30-ch** AC	**$SNR_{30,AC}/SNR_{BC}$**
center (1)	14	14	13	0.9
ventricle (2)	23	27	27	1.2
periphery (3)	11	24	27	2.5

Comparison of image data

The image quality obtained by the two coils is compared in vivo in a healthy volunteer in **Figure 4.5**. Additionally, ^{1}H data are shown which were acquired with a fast GRE scan to demonstrate the performance of the ^{1}H channel. Respective acquisition parameters are listed in **Table 4.4**. As expected from the SNR maps, the image data from the single-channel birdcage coil exhibits higher noise than the array data. However, the SOS reconstruction shows high background noise. This is greatly reduced for the AC channel combination, where almost no background noise is visible. The 30-channel data exhibit an intensity decrease towards the brain center due to the receive sensitivity of the array. By normalization to the B_1^- field, this can be compensated. The 30-channel data allows an improved discrimination of finer structures in the cortex. Concerning the ^{1}H channel, a full brain coverage is achieved.

Table 4.4: Acquisition parameters for the comparison of the image quality between the birdcage and the 30-channel array.

Parameter		**Value**
Sequence		DA 3D-RAD
nom. resolution	Δx	2 mm
max. gradient amplitude	G_0	12.00 mT/m
projections	N_{proj}	25,000
radial samples	#RadSamples	512
echo time	TE	0.35 ms
repetition time	TR	30 ms
readout duration	T_{RO}	10 ms
flip angle	α	53°
pulse length	t_p	600 µs
averages		2
acquisition time	T_{AQ}	2 × 12:30 min

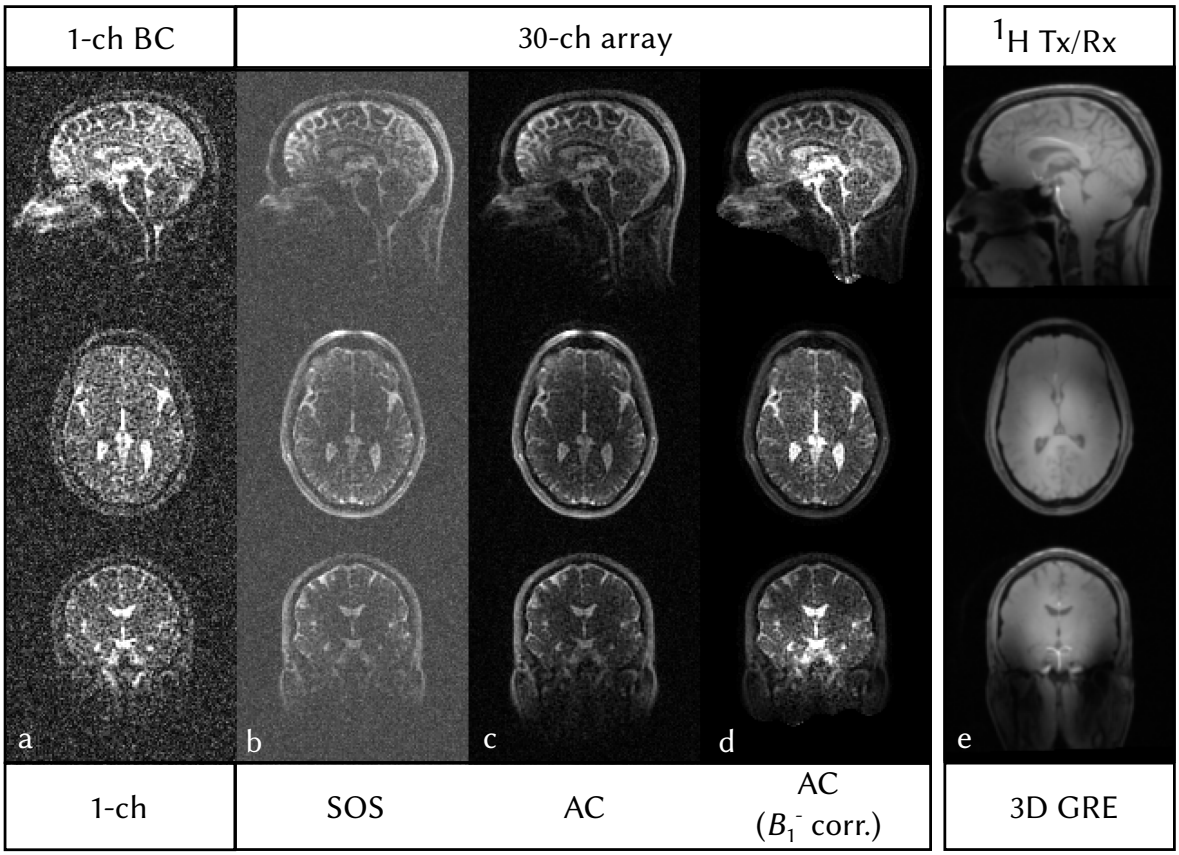

Figure 4.5: In vivo comparison of image data from the 30-channel array coil and the birdcage at same acquisition parameters. Shown are single channel birdcage data (a), 30-channel data with SOS combination (b), with AC (c), and AC with additional correction of the B_1^- profile (d). The higher SNR of the array coil allows for a better resolution of fine structures in the cortex. A fast ^{1}H GRE acquisition is shown in e).

4.1.2 Optimization of T_2^* sampling

In the following, the results from the optimization of the sampling pattern will be presented.

Minimum SNR for parameter fitting of a biexponential model

In this work, the acquisition parameters for in vivo the T_2^* measurements are determined through a minimum SNR requirement in WM for reliable parameter estimation. In order to obtain this threshold value, the fitting quality was analyzed over a range of possible SNRs. A typical biexponential signal decay was calculated over a range of SNR = 1–40 and fitted with the signal model (Section 3.2.1). The curve was sampled at the positions of a linear pattern with 4 sets and $\Delta TE = 7$ ms. This results in 32 points at the time points [0:1.75:54.25] ms. The mean bias and standard deviation over 100,000 repetitions are depicted in **Figure 4.6**. The bias of the amplitude A_0 and the short component $T_{2,\mathrm{s}}^*$ display similar behavior with values less than 5 % down to an SNR of 5. Below this value, a strong increase of a systematic overestimation is found. For the long component $T_{2,\mathrm{l}}^*$, fitting below an SNR of 10 leads to an overestimation by more than 10 % (cf. **Figure 4.6**, a). At SNR>15, all parameters are determined with a bias smaller than 3 %. The standard deviation displays an increasing accuracy for an SNR greater 5 (cf. **Figure 4.6**, b). The short component exhibits highest and the amplitude lowest variation. The long relaxation time exhibits a medium uncertainty in between. At SNR = 15, the uncertainty of $T_{2,\mathrm{s}}^*$ drops below 20 % and the standard deviations of $T_{2,\mathrm{l}}^*$ and A_0 are 12 % and 5 %. At SNR = 30, a variation lower than 10 % is reached.

Optimization of the sampling scheme

The calculation of the metric Q (cf. Equation 3.10) required repetitive data fitting and the variation between these fitting repetitions was used as a measure for the quality of the sampling pattern. To this end, the number N' of fit repetitions had to be determined at which the fit statistics are sufficiently sampled and Q becomes well-defined. This was done by reevaluating Q 100 times for different N ranging from 100 to 300,000. If N' is reached, the standard deviation over the 100 evaluation of Q should not change with further increasing N and converge to minimum. The standard deviation over the 100 results for Q as a function of N are displayed in **Figure 4.7**. As can be seen, at a value of $N = 5,000$ the variation of Q becomes minimal. For the optimization of the sampling pattern, a higher value of $N = 30,000$ was used for more reliability and for the comparison of the different pattern $N = 100,000$ was chosen. In **Figure 4.8**, the value of Q is shown for one path from the global optimization procedure. As can be seen, the value of Q steadily decreases until the minimization stops after 9 iterations.

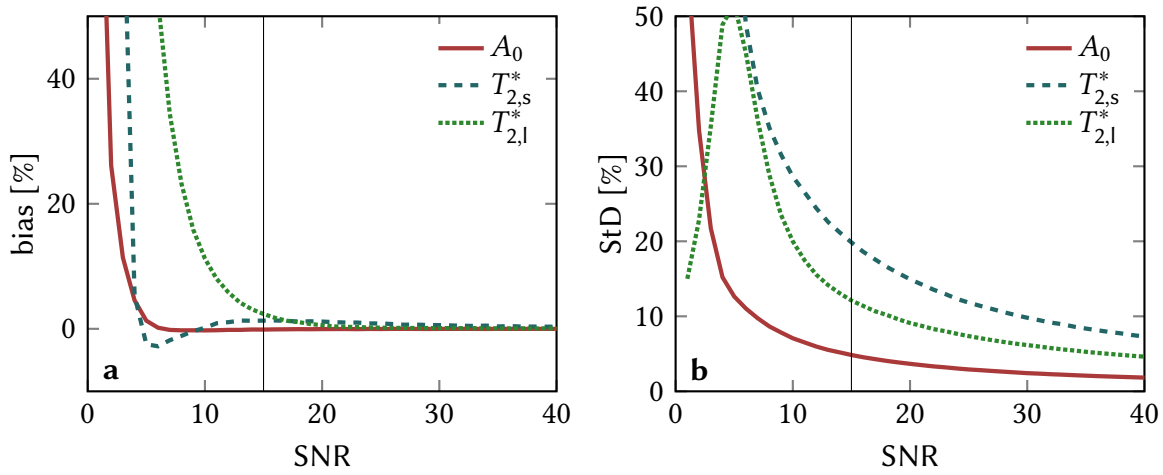

Figure 4.6: Bias (a) and standard deviation (StD, b) for fitting a biexponential decay at varying SNR. The SNR was varied from 1 to 40 (black line at SNR = 15). The short component displays the highest bias and variation. At SNR = 15, the bias of all parameters is less than 5 % and the variation drops below 20 %.

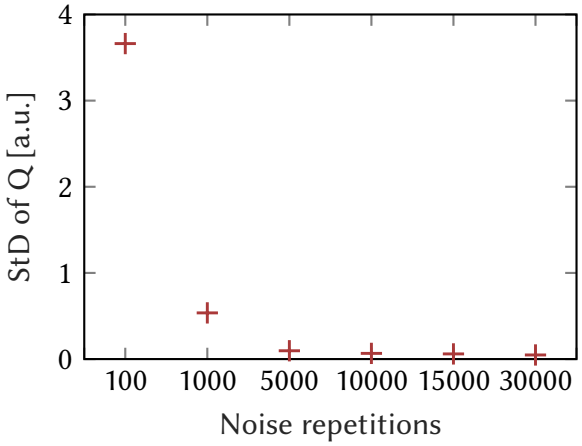

Figure 4.7: Test for well-definition of Q. Shown is the standard deviation for repetitive evaluation of Q for a varying number of noise repetitions N. If the fit statistics inside Q are sampled sufficiently accurately, Q becomes well-defined and converges to a minimum value. This is reached at $N' = 5,000$ noise repetitions.

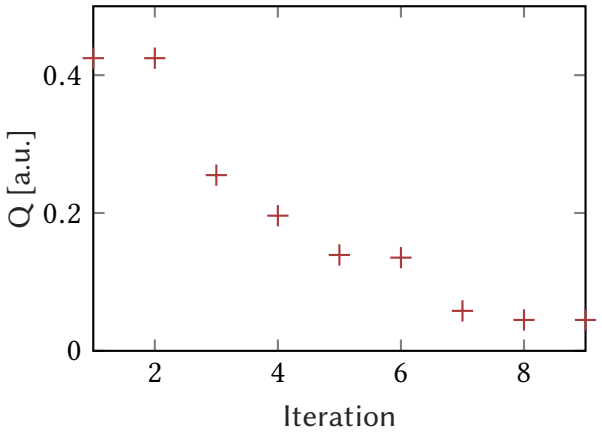

Figure 4.8: Convergence behavior of Q during optimization. Shown is one optimization path in the multi-start algorithm. The minimization of Q progresses steadily and stops after nine iterations.

Optimized sampling scheme

The sampling scheme obtained from the minimization of the quality metric Q described in detail in Section 3.2.2 resulted in the shifts ΔRep_i given in **Table 4.5**. A visualization together with the alternative sampling patterns is shown in **Figure 4.9**. The optimized sampling is determined by $\Delta\text{Rep} = [0.0, 0.0, 0.0, 4.1]$ ms. Thus, the pattern consists of 3 averages at TE_{min} and an additional point at $TE = TE_{\text{min}} + 4.1$ ms.

4.1.3 Evaluation of T_2^* determination

In this section, different aspects are investigated which have an influence on the accuracy and uncertainty of the T_2^* determination. First, a comparison of the different sampling patterns is presented. Signal simulations were performed for five different schemes for a variety of $T_{2,\text{s}}^*$ and $T_{2,\text{l}}^*$ as well as for different SNR. Furthermore, three fitting models are analyzed with regard to systematic bias due to noise signal.

Table 4.5: Shifts ΔRep_i of the scheme resulting from the optimization shown together with values of the alternative patterns. The optimized pattern consists of three averages at TE_{min} and one intermediate point at 4.1 ms.

sampling scheme	ΔRep_i [ms]
optimized	0.00, 0.00, 0.00, 4.10
linear	0.00, 1.75, 3.50, 5.25
early TE	0.00, 0.50, 1.00, 1.50
Jones et al. [1996]	0.00, 6.50, 6.50, 6.50
averaging	0.00, 0.00, 0.00, 0.00

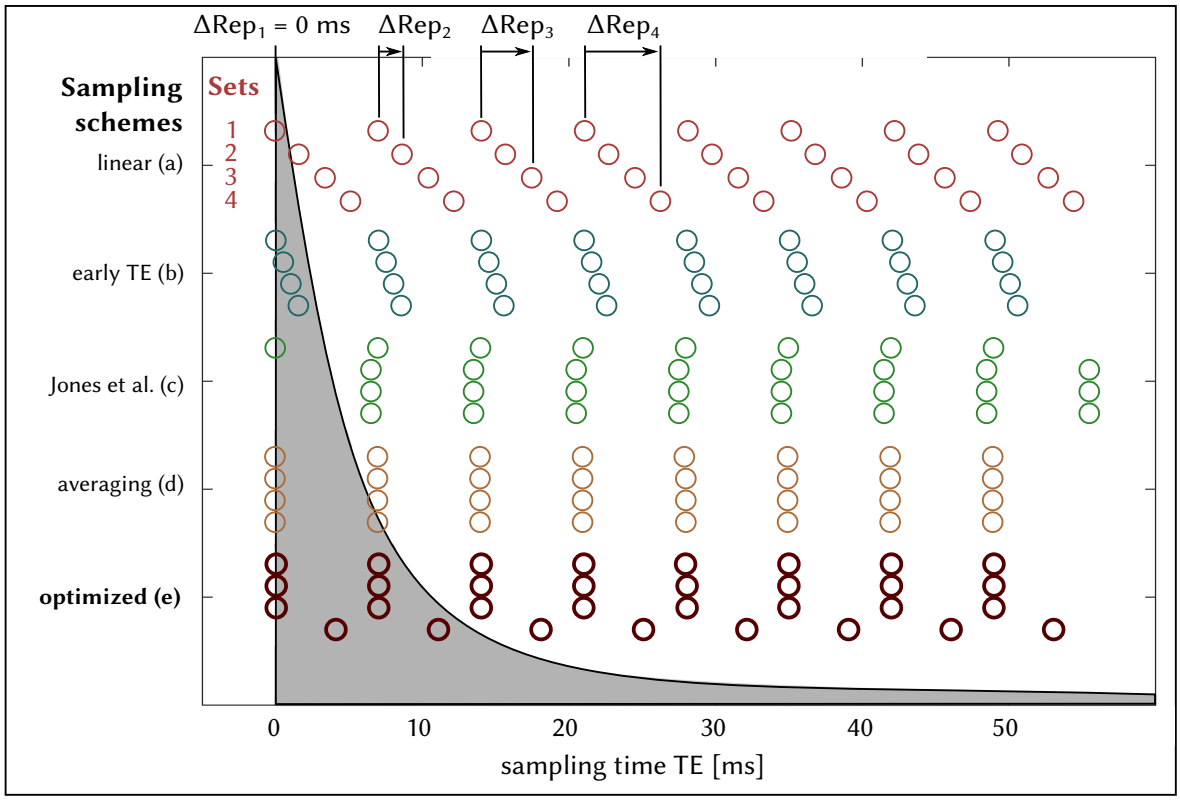

Figure 4.9: Sample distribution of the optimized scheme (dark red) determined by the shifts ΔRep = [0.0, 0.0, 0.0, 4.1] ms. The optimized pattern consists of 3 averages at TE_{min} and an additional point at $TE = TE_{\text{min}} + 4.1$ ms. The pattern is shown together with the investigated alternatives for comparison.

T_2^* resolution of different sampling schemes

The performance of the considered sampling schemes (cf. **Figure 4.9**) was investigated for a range of $T_{2,s}^*$ and $T_{2,l}^*$ which are likely to occur in vivo. To this end, data was simulated and analyzed as described in Section 3.2.2. Bias, uncertainty, as well as overall quality Q were determined for $T_{2,s}^*$ ranging from 0 ms to 20 ms (0.0, 0.1, 0.5, 1.0 ms, and 2 ms to 20 ms in steps of 2 ms) and for $T_{2,l}^*$ varying from 20 ms to 52 ms in steps of 4 ms. Averaging and the optimized pattern exhibit the most accurate determination of A_0 (0.1 % to 0.5 % bias, **Figure 4.10**). For the other schemes, a lower reliability is found as demonstrated by the higher standard deviation ($\approx$ 7 %, **Figure 4.11**). $T_{2,s}^*$ is generally overestimated for very short relaxation times. At higher $T_{2,s}^*$, a transition from underestimation to overestimation is found as a function of $T_{2,l}^*$ in the range of $T_{2,l}^*$ = 30 ms to 40 ms. Most accurate determination of $T_{2,s}^*$ is found for $T_{2,s}^*$ between 4 ms to 10 ms and $T_{2,l}^*$ in the range of 30 ms to 50 ms. For all schemes, this region also exhibits low variation (18 % to 25 %) with increasing uncertainty towards very short $T_{2,s}^*$ (**Figure 4.11**). Averaging, early TE, and the optimized pattern exhibit an extended region of improved fitting quality as seen in the maps of the metric Q (**Figure 4.12**). This region is most extended for the optimized and linear pattern as affirmed by a low standard deviation over a wider range (cf. **Table 4.6** and **Figure 4.12** for the evaluation region). The optimized pattern exhibits the lowest mean values which demonstrates best overall parameter estimation. The optimized scheme exhibits a more robust determination whilst the linear pattern allows to resolve shorter relaxation times. The accuracy of $T_{2,l}^*$ does not display a pronounced dependency on the sampling pattern. The variation of $T_{2,l}^*$ increases slightly for longer $T_{2,s}^*$ and a systematic overestimation for values close to $T_{2,s}^*$ is found. Even for $T_{2,s}^*$ close to zero, $T_{2,l}^*$ and A_0 can be observed without additional bias (cf. **Figure 4.10** and **4.11**, top rows).

Table 4.6: Mean values and standard deviation (StD) of quality Q over a range of T_2^* for the considered sampling schemes. A low mean value displays a higher quality of the parameter estimate. A low standard deviation represents a constant behavior over the considered region. The values were normalized to the lowest (best) value retrieved by the optimized pattern. Please note that in Figure 4.12 the logarithm of the values is shown which makes variations appear smaller.

	linear	early TE	Jones et al.	averaging	optimized
Mean ± StD	1.02 ± 1.35	3.33 ± 6.38	23.02 ± 62.33	19.49 ± 47.87	1.00 ± 1.61

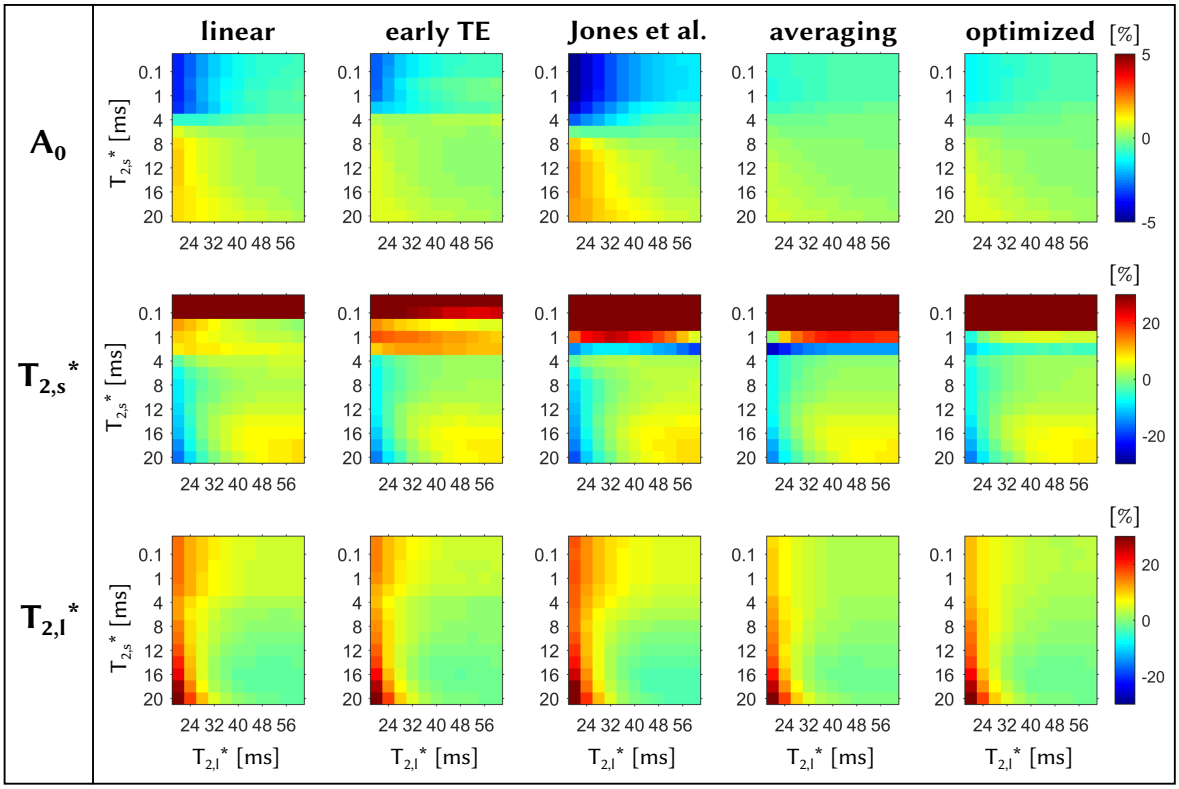

Figure 4.10: Relative bias of parameter estimation over a range of T_2^* values for different sampling schemes at SNR = 15. See text for more information on the exact T_2^* values. Smoothest variation and lowest bias are found for the linear and optimized pattern. The latter shows a more robust determination, whilst the linear pattern allows to resolve shorter relaxation times. $T_{2,s}^*$ is underestimated for short $T_{2,l}^*$ whilst overestimated for longer $T_{2,l}^*$. Most accurate determination is found for $T_{2,s}^*$ between 4 ms and 10 ms and $T_{2,l}^*$ between 30 ms and 50 ms. The accuracy of $T_{2,l}^*$ does not show a pronounced dependence on the sampling pattern.

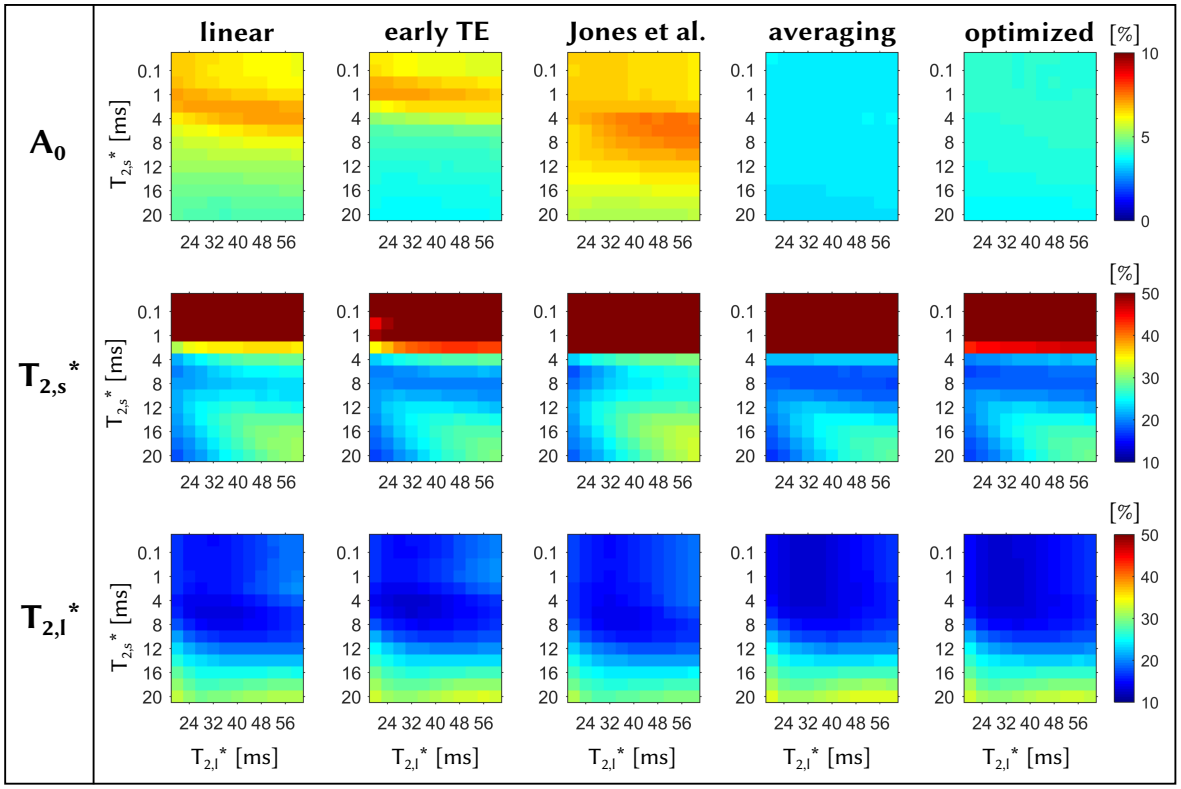

Figure 4.11: Relative standard deviation of parameter estimation over a range of T_2^* values for different sampling schemes at SNR = 15. See text for more information on the exact T_2^*values. For A_0, averaging and the optimized pattern show most favorable behavior ($\approx$ 4 % variation). A stronger variation ($\approx$ 7 %) is found at very short $T_{2,s}^*$ for the other patterns. The short component $T_{2,s}^*$ exhibits a region with relatively low variation (18 % to 25 %) at medium $T_{2,s}^*$, which is most pronounced in the optimized scheme. For all schemes the variation increases for short $T_{2,s}^*$. The long relaxation component $T_{2,l}^*$ does not exhibit a pronounced dependency on the sampling pattern.

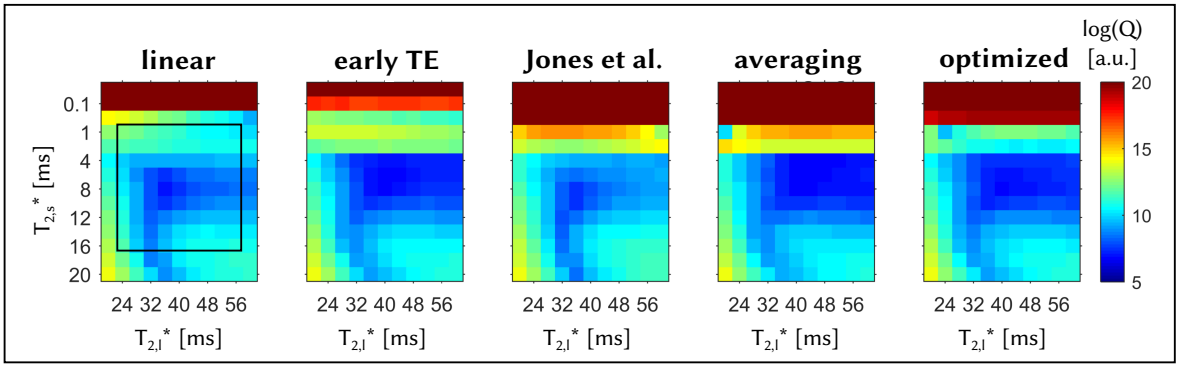

Figure 4.12: Quality metric Q representing overall performance of parameter estimation. The logarithm of Q is shown for better visualization. A region with favorable behavior is found for the early TE pattern, averaging, and the optimized pattern at medium $T_{2,\mathrm{s}}^*$ and $T_{2,\mathrm{l}}^*$. This region is most extended for the optimized and linear pattern as affirmed by the mean and standard deviation in the marked region (cf. Table 4.6). The pattern of Jones et al. and averaging exhibit decreased resolution for very short $T_{2,\mathrm{s}}^*$, whilst the early TE scheme performs best in this aspect. Please note that the logarithm makes variations appear smaller than they actually are.

T_2^* determination at varying SNR

The performance of the different sampling schemes is shown as a function of the image SNR in **Figure 4.13**. The parameter estimates were averaged over a range of T_2^* values in order to take into account variations in the relaxation times, e. g. due to pathologies. The range was chosen symmetrically around reported relaxation values for brain parenchyma ($T_{2,s}^*$ = 3 ms to 7 ms, $T_{2,l}^*$ = 32 ms to 48 ms [Nagel et al., 2011]). For SNR = 15, the average bias for all schemes is 0.4 %, 4 %, and 11 % (A_0, $T_{2,s}^*$, and $T_{2,l}^*$) and the uncertainty is of the order of 5 %, 25 %, and 15 %, respectively. The signal amplitude is most accurately determined by averaging (0.16 %) and the optimized pattern (0.22 % bias). $T_{2,s}^*$ is captured best by the optimized pattern (2.0 % bias) whereas averaging exhibits highest bias (4.4 %). The uncertainty is similar for the optimized, linear, and early TE pattern (26.0 %) and highest for the pattern by Jones et al. (34.5 %). The influence on $T_{2,l}^*$ is low. Here, the highest accuracy is found for the early TE pattern and averaging (2.7 %), and lowest for Jones et al. (4.5 %). The uncertainty is in the range of 15 %. The overall performance Q rates the optimized pattern as the most appropriate. Linear sampling exhibits similar behavior while early TE, Jones et al., and averaging result in lower overall quality.

Analysis of data fitting

To understand the influence of the fitting model in the parameter estimation three models were investigated with regard to their behavior under different noise amplitudes and sample numbers. To this end, multiple fitting repetitions were performed for all parameters (cf. Section 3.2.1). The mean and standard deviation were determined for all models and are shown in **Figure 4.14** for SNR = 10, 15, and 20. In general, the short component is overestimated ($\approx$ 6 %) whilst amplitude and long component exhibit a more complicated behavior. Including the noise floor as an additional fit parameter results in the strongest bias at low SNR and low TE_{max} < 80 ms (bias $\approx$ 40 %). The bias decreases for a higher number of samples. The two models with constant noise term yield similar results at lower TE_{max}. However, if the noise contribution is neglected (n = 0), a systematic bias is found for higher TE_{max}, resulting in an overestimation of $T_{2,l}^*$ and an underestimation of A_0. For rather low TE_{max}, like TE_{max} = 55 ms used in this study for in vivo T_2^* mapping, the short component is determined most accurately by neglecting the noise contribution. A_0 and $T_{2,l}^*$ are captured comparably by neglecting or including the known SNR up to medium TE_{max} around 80 ms. For A_0, the standard deviation is almost independent for all models. For the relaxation times, decreasing uncertainty is found for higher number of sampling points. However, at TE_{max} $\approx$ 100 ms, the reliability of $T_{2,s}^*$ does not increase further which similarly applies to $T_{2,l}^*$ for TE_{max} higher 80 ms. $T_{2,s}^*$ is detected most reliably by using a constant noise floor.

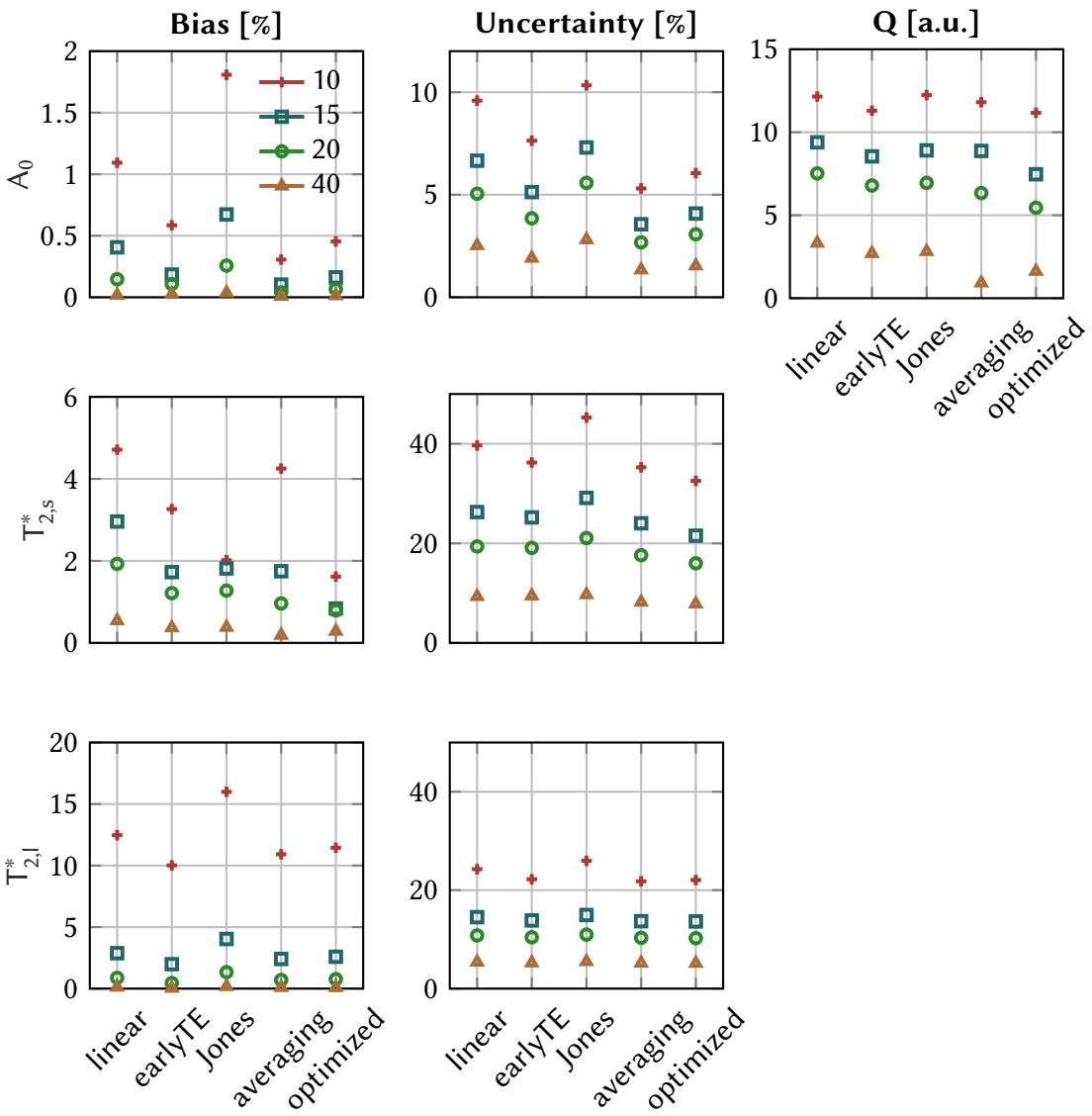

Figure 4.13: Performance of the different sampling schemes for varying SNR. Bias, standard deviation, and the overall quality Q are depicted for SNR = 10/15/20/40. To determine the quality of the different schemes when quantifying tissue with varying relaxation times (e.g. due to pathologies), values were averaged over a range around reported T_2^* values for brain with $T_{2,s}^*$ = 3 ms to 7 ms and $T_{2,l}^*$ = 32 ms to 48 ms. At SNR = 15, lowest bias and variation are found for the optimized scheme. $T_{2,l}^*$ does not show a strong dependency on the sampling pattern. The overall quality Q is best (lowest values) for the optimized pattern.

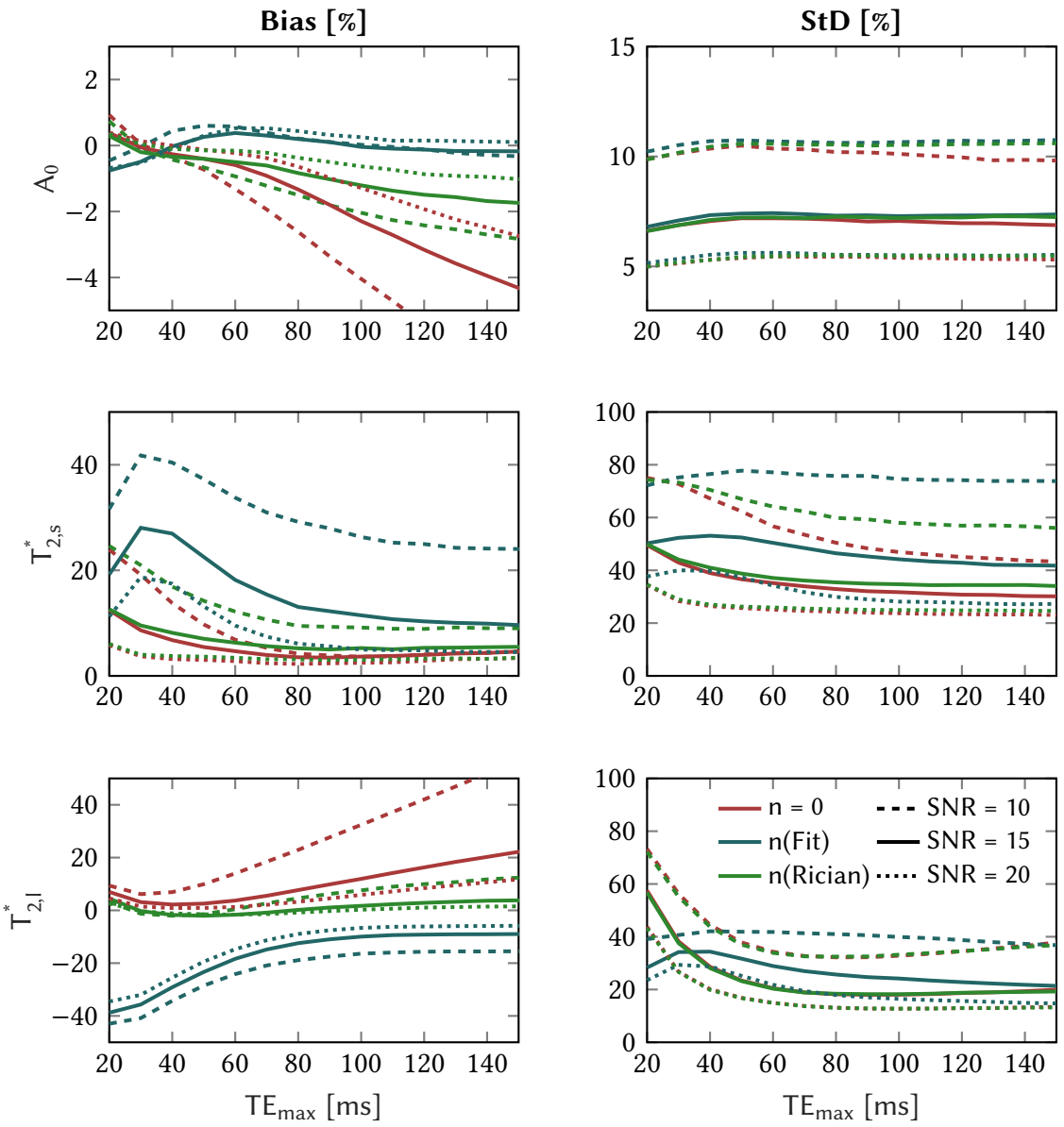

Figure 4.14: Bias and standard deviation (StD) of parameter estimation for three different fitting models as function of the SNR and the number of sampling points. TE_{max} is the latest sampling point and determines the number of samples. The different fit models are characterized by neglecting (red), fitting (blue), and setting the known noise amplitude for the noise floor (green). At low TE_{max}, lowest bias is found when neglecting the noise floor. If more samples are acquired, it has to be taken into account. The reliability of the T_2^* estimates increases up to a certain threshold around 80 ms after which most of the signal has decayed.

4.2 In vivo T_2^* mapping

In this section, in vivo T_2^* mapping of ^{23}Na ions in healthy human brain is presented. The quantification of the signal relaxation was conducted with the linear and the optimized pattern in three healthy volunteers. Possible errors due to signal blurring from liquid compartments into the parenchyma are analyzed. Finally, the correlation time of the interaction of the ^{23}Na ions with their environment is determined.

4.2.1 Workflow of the in vivo evaluation

In vivo T_2^* mapping in healthy human brain was performed with both the linear and the optimized acquisition scheme in 3 healthy volunteers (age 26±4 years). Acquisition parameters were chosen such that an SNR of approximately 15 was achieved at TE_{min} in WM after Hamming filtering. This resulted in a measurement time of 15 min per set and $N_{\text{reps}} = 4$ repetitions could be acquired within one hour. ^{23}Na measurements were conducted with the ^{23}Na 30-channel array coil (cf. Section 3.1.1), using the multi echo version of the DA 3D-RAD sequence (cf. Section 3.1.1). The flip angle was determined via the Ernst angle (cf. Equation 2.64) for $T_1 = 37$ ms as reported by Nagel et al. [2011]. Additionally, two anatomical scans were acquired using the 24-channel ^{1}H coil (cf. Section 3.1.1). These were, an MPRAGE sequence (T_1 weighted) for the tissue segmentation and a CISS sequence (T_2 weighted) with strong brain-liquor contrast to improve the brain extraction (cf. Section 3.1.1). Acquisition parameters of the pulse sequences are listed in **Table 4.7** and **Table 4.8**.
The image data were reconstructed using adaptive combination (cf. Section 3.1.2) and then each echo time was coregistered to the acquisition at $TE_{\text{min}} = 0.35$ ms. In each voxel, the biexponential signal model was fitted with the noise parameter $n = 0$ (Equation 3.8). This was determined to be the most reliable signal model at the chosen acquisition parameters (cf. Section 4.1.3). Mono- and biexponential compartments were separated by refitting voxels with $T_{2,\text{l}}^* > 50$ ms with a monoexponential model similar as proposed by Blunck et al. [2017]. The relaxation constants were initialized with $T_{2,\text{s}}^*/T_{2,\text{l}}^* = 3\,\text{ms}/30\,\text{ms}$ and the amplitude A_0 with the intensity of the first echo $A_0 = S(TE_{\text{min}})$ due to varying signal intensity of different tissues (e.g. $S_{\text{CSF}} \approx 4 \cdot S_{\text{WM}}$). The values were loosely constraint to the intervals [0,1.2], [0,15] ms and [0,80] ms ($A_0/T_{2,\text{s}}^*/T_{2,\text{l}}^*$). Image data was normalized to the maximum value of the image acquired at $TE = 0.35$ ms.
The compartments of WM and CSF were segmented with masks retrieved from the MPRAGE scan using FSL (cf. Section 3.3.3). The segmentation was conducted at ^{1}H resolution and then coregistered to the ^{23}Na scan (cf. workflow diagram, **Figure 4.15**). Only voxels with a partial volume share of at least 90 % were included. During this process, the mask for GM could not be retained due to the small extent of this compartment.
Exemplary reconstructions of the data used for T_2^* mapping are displayed in **Figure 4.16** for one volunteer (age 22). Shown are the first 30 echoes of the linear pattern representing equidistant time steps of $\Delta TE = 1.75$ ms. The data were acquired at a nominal resolution of 2.8 mm and reconstructed with a Hamming filter. The long T_2^* of CSF can be acknowledged

Table 4.7: Acquisition parameters for the in vivo T_2^* mapping using the multi echo readout (cf. Section 3.1.1) with the optimized and linear sampling scheme.

Parameter		**Value**
Sequence		ME DA 3D-RAD
nom. resolution	Δx	2.8 mm
max. gradient amplitude	G_0	10.45 mT/m
projections	N_{proj}	14,000
radial samples	#RadSamples	384
minimal echo time	TE_{min}	0.35 ms
other sample points		cf. Section 4.1.2
repetition time	TR	65 ms
readout duration	T_{RO}	5.6 ms
rewinder duration	T_{RW}	1.4 ms
echo spacing	ΔTE	7 ms (= T_{RO} + T_{RW})
flip angle	α	79°
pulse length	t_p	600 µs
acquisition time	T_{AQ}	4 × 15 min (N_{reps} = 4)

Table 4.8: Acquisition parameters for the anatomical ^{1}H scans used for the brain tissue segmentation. The MPRAGE was used for the segmentation and the CISS for an improved brain extraction.

Parameter		**Value**
Sequence		MPRAGE
resolution	Δx	0.6 mm
echo time	TE	1.99 ms
repetition time	TR	3400 ms
inversion time	TI	1200 ms
bandwidth	BW	362 Hz
flip angle	α	9°
acquisition time	T_{AQ}	10 min

Parameter		**Value**
Sequence		CISS
resolution	Δx	0.6 mm
echo time	TE	2.2 ms
repetition time	TR	5.01 ms
inversion time	TI	-
bandwidth	BW	610 Hz
flip angle	α	13°
acquisition time	T_{AQ}	7:30 min

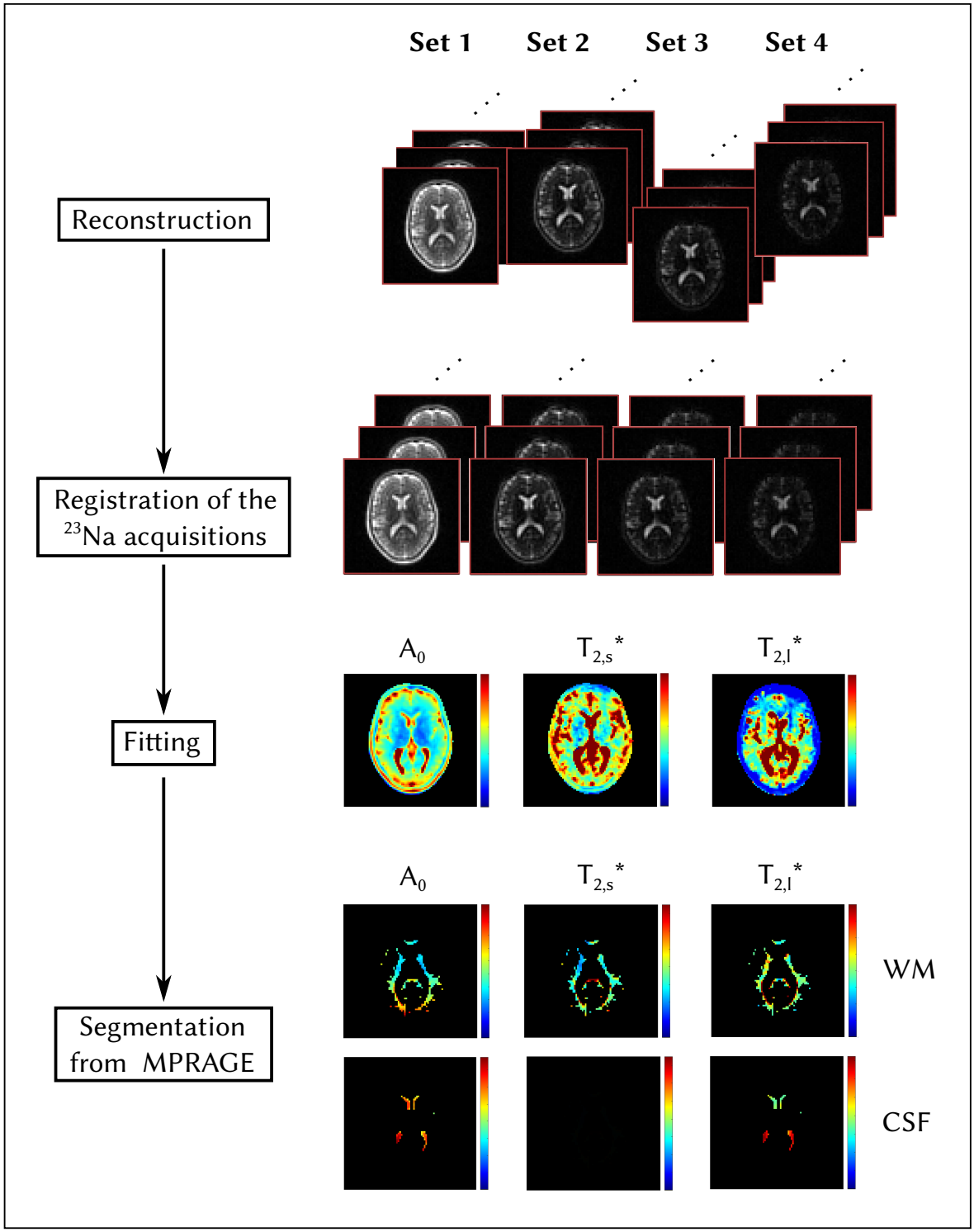

Figure 4.15: Workflow of the in vivo evaluation. First, the ^{23}Na data were reconstructed and coregistered to the first acquisition at TE_{min}. Then, the signal model was fitted to the image data. The tissue compartments were separated using masks retrieved from an MPRAGE scan.

compared to the fast signal decay in parenchyma. For later echo times, distortions in the frontal region become stronger due to B_0 inhomogeneities caused by air in the paranasal sinuses. In **Figure 4.17**, the signal decay is depicted for two example voxels, one located in WM and one in CSF. The location of the voxels is marked in the figure. The biexponential signal decay can be seen in the WM voxel. In CSF, the signal decays more slowly exhibiting monoexponential shape. The SNR of the data in WM is reduced compared to CSF due to the lower tissue concentration ([^{23}Na] $\approx$ 30 mM vs. 150 mM [Madelin and Regatte, 2013]).

4.2.2 T_2^* relaxation in human brain

Voxel-wise T_2^* maps were determined by fitting of the image data with the respective signal model expected from theory (cf. Section 3.2.1). An example T_2^* map of one volunteer is depicted in **Figure 4.18**. In both sampling strategies an intensity increase towards the brain periphery is seen in the amplitude data, which is due to the sensitivity profile of the coil. Substructures of the WM adjacent to the lateral ventricles can be acknowledged. These structures are more clearly visible in the data of the optimized pattern. In the maps of the relaxation components in brain parenchyma (b,c,f,g) a strong contrast between fluid and tissue compartments is seen, stemming from the slower decay times in the CSF. In the comparison of the relaxation maps of the short component, the cortex region exhibits slightly higher overall values in the linear pattern than in the optimized. From the relaxation maps, the compartments of WM and CSF were segmented to obtain mean values for these tissue types. Additionally, data from a smaller ROI were extracted to reduce errors due to signal blurring from neighboring compartments. These ROIs were located in the WM close to the ventricles (cf. **Figure 4.18** for the location). An overview of all relaxation times is given in **Table 4.9**. For all volunteers, the $T_{2,\mathrm{s}}^*$ obtained with the linear pattern were higher than those of the optimized pattern. These were 7.1 ± 2.0 ms, 5.6 ± 0.5 ms, and 6.7 ± 1.2 ms for the linear pattern and 6.6 ± 2.2 ms, 5.4 ± 1.3 ms, and 6.3 ± 1.8 ms for the optimized scheme. The respective mean values are 6.5 ± 0.8 ms and 6.1 ± 0.6 ms (linear/optimized). This difference was more pronounced for the local ROI evaluation than in the segmentation over the whole brain. There, the values for linear sampling were 6.2 ± 1.3 ms, 4.5 ± 0.9 ms, and 4.6 ± 0.9 ms and 4.8 ± 0.6 ms, 4.0 ± 0.6 ms, and 3.9 ± 1.0 ms for the optimized scheme. The mean values are 5.1 ± 0.8 ms and 4.2 ± 0.4 ms. The long relaxation component displays a similar trend with mean values of 40.9 ± 2.2 ms and 40.1 ± 2.2 ms in the full WM segmentation and 35.7 ± 2.4 ms and 34.4 ± 1.5 ms in the ROI. In CSF, the mean monoexponential relaxation times of both patterns are similar being 53.6 ± 6.9 ms and 54.4 ± 5.7 ms.

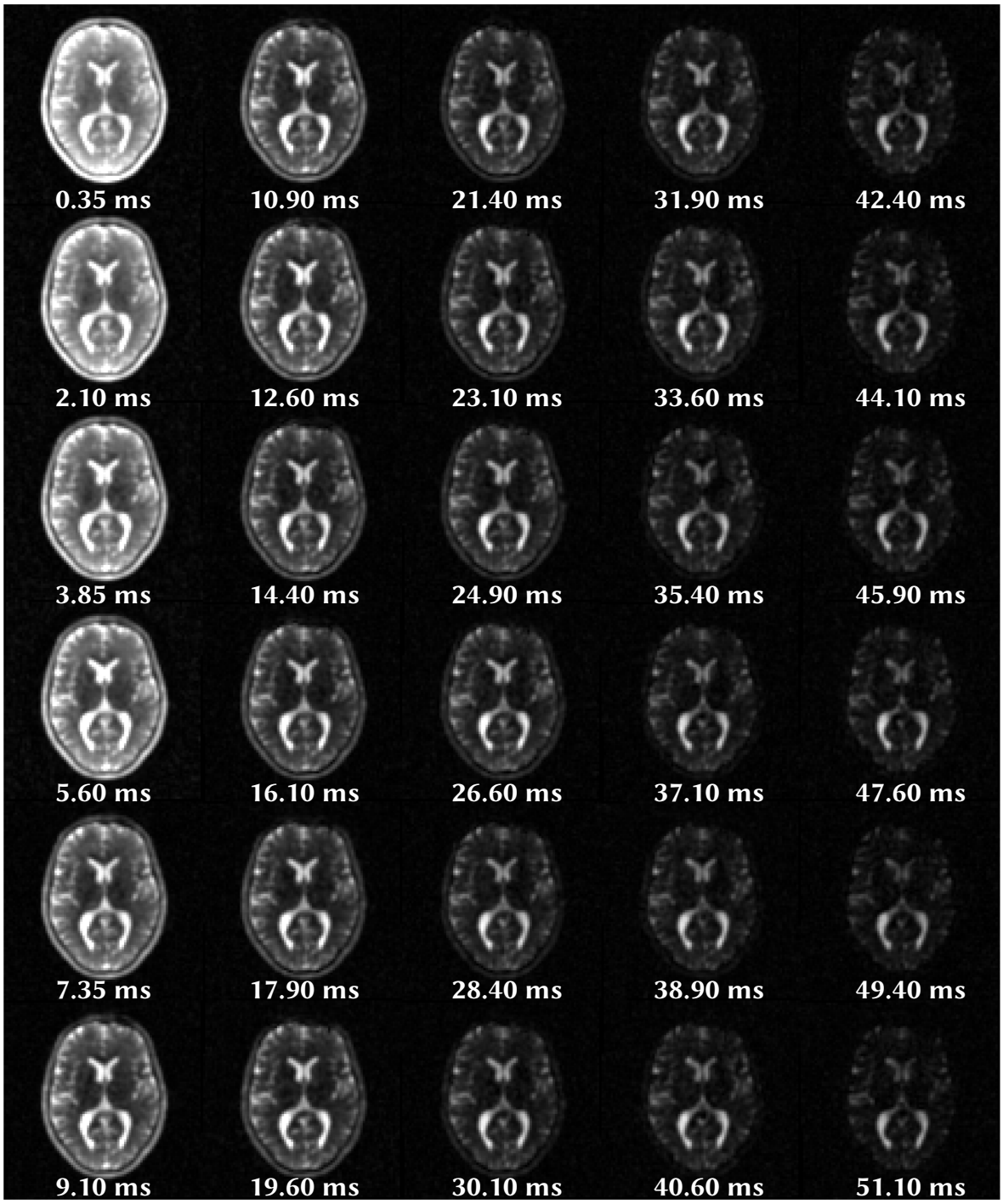

Figure 4.16: Image reconstructions of the base data for T_2^* mapping. Shown are the first 30 echoes of the linear pattern. The data were acquired at a nominal resolution of 2.8 mm and reconstructed with a Hamming filter. The long T_2^* of CSF can be acknowledged compared to the fast signal decay in parenchyma. For later echo times, distortions in the frontal region become visible due to B_0 inhomogeneities caused by air in the paranasal sinuses.

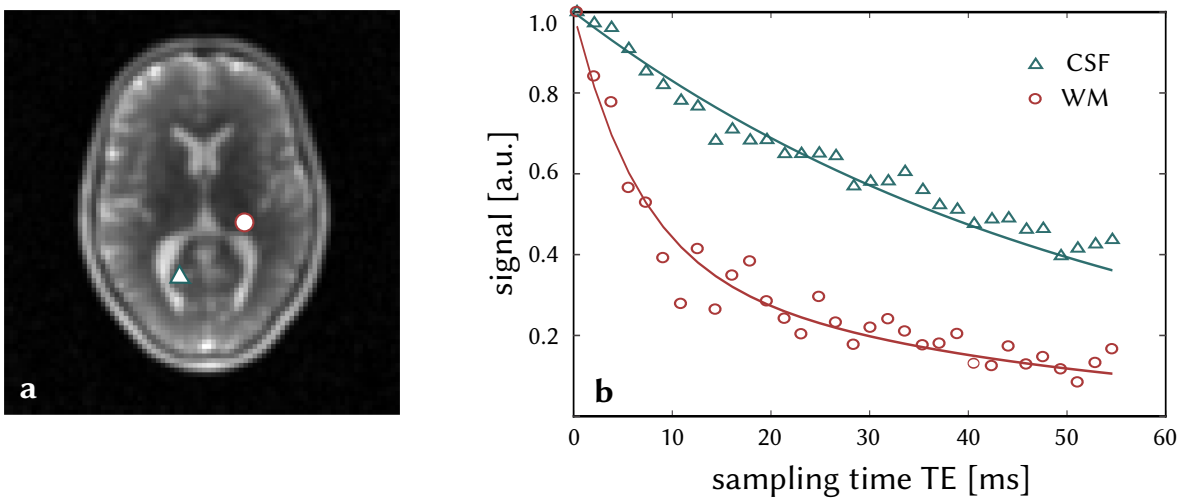

Figure 4.17: Example voxel data and decay curves in brain tissue. The signal decay in two voxels of WM and CSF (red circles and green triangles) is shown together with decay curves describing the mean decay from this volunteer (b). The location of the voxels is marked in the image data (a). Signal intensities in both voxels were normalized to the first point. The lower SNR of WM is due to a lower concentration compared to CSF.

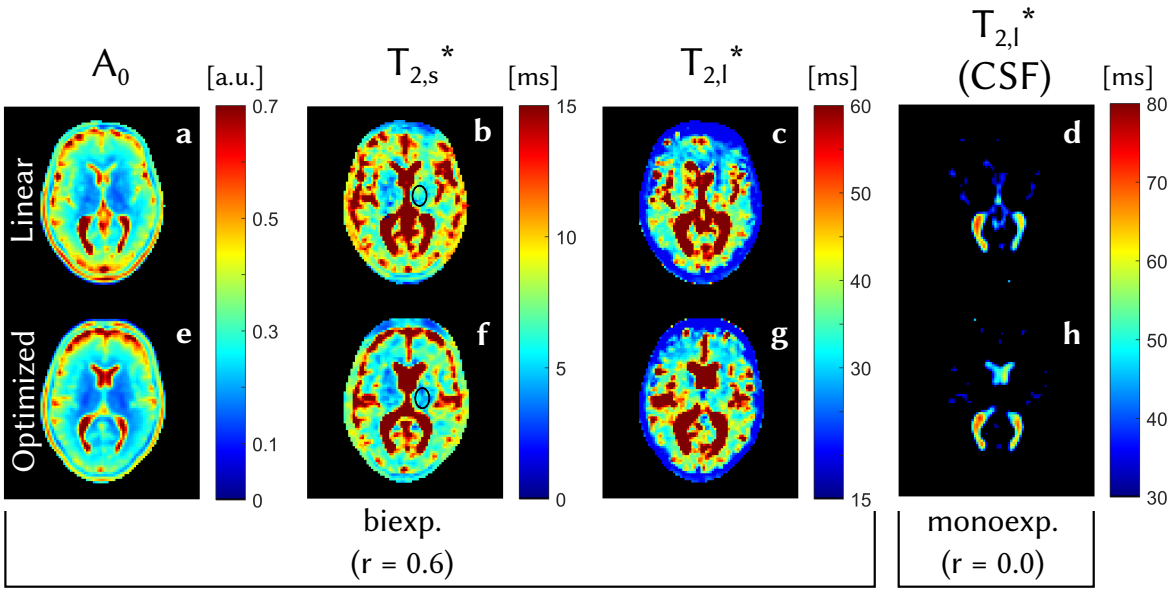

Figure 4.18: In vivo parameter maps of the relaxation times in a healthy volunteer measured with the linear sampling pattern (a-d) and the optimized scheme (e-h). A_0, $T^*_{2,s}$, and $T^*_{2,l}$ are shown from left to right. $T^*_{2,l}$ is displayed for fluid compartments with a monoexponential fit (d, h) and with a biexponential fit for parenchyma (b, c and f, g). In parenchyma, the optimized pattern yields shorter relaxation times compared to linear sampling (black circle, also cf. Table 4.9).

Table 4.9: In vivo T_2^* times in WM and CSF of 3 healthy volunteers (age 26 ± 4) with two different sampling patterns. Only voxels with more than 90 % compartment probability in the segmentation were included (Seg). In WM, the optimized pattern results in lower T_2^* values for both short and long component as shown in a separate ROI. In CSF, the relaxation time of the monoexponential model agrees within the uncertainty for both patterns.

Sampling scheme	**Volunteer (Age)**		$T_{2,s}^*$ **[ms]**	$T_{2,l}^*$ **[ms]**	
			WM	WM	CSF
Linear	1 (22)	Seg	7.1 ± 2.0	42.3 ± 11.4	57.0 ± 11.4
		ROI	6.2 ± 1.3	34.0 ± 2.8	
	2 (26)	Seg	5.6 ± 1.5	38.3 ± 7.1	45.6 ± 10.3
		ROI	4.5 ± 0.9	32.3 ± 4.7	
	3 (30)	Seg	6.7 ± 1.2	42.0 ± 11.0	58.0 ± 11.7
		ROI	4.6 ± 0.9	36.4 ± 4.2	
	Mean ± StD	Seg	**6.5 ± 0.8**	**40.9 ± 2.2**	**53.6 ± 6.9**
		ROI	**5.1 ± 0.8**	**35.7 ± 2.4**	
Optimized	1 (22)	Seg	6.6 ± 2.2	41.5 ± 11.8	56.2 ± 11.3
		ROI	4.8 ± 0.6	33.5 ± 2.7	
	2 (26)	Seg	5.4 ± 1.3	37.5 ± 7.1	48.0 ± 9.4
		ROI	4.0 ± 0.6	34.6 ± 2.7	
	3 (30)	Seg	6.3 ± 1.8	41.2 ± 11.2	59.0 ± 12.3
		ROI	3.9 ± 1.0	39.0 ± 5.9	
	Mean ± StD	Seg	**6.1 ± 0.6**	**40.1 ± 2.2**	**54.4 ± 5.7**
		ROI	**4.2 ± 0.4**	**34.4 ± 1.5**	

4.2.3 Influence of signal contamination from CSF

For quantification measurements in parenchyma, the signal contribution coming from CSF due to partial volume effects results in a systematic error. To this end, the deviation in the observed relaxation times was investigated. The difference due to the sampling scheme was analyzed for varying amount of liquid contamination. Furthermore, measurements were performed at two different resolutions and quantification before and after filtering were compared.

Apparent relaxation in case of liquid contamination

In the analysis of the sampling patterns, the linear and optimized sampling strategies were found to be the most appropriate ones (cf. Section 4.1.3). Therefore, the behavior of these schemes was investigated for the case of signal contamination in parenchyma coming from liquid compartments. A biexponential decay was simulated ($T^*_{2,\mathrm{s}}/T^*_{2,\mathrm{l}}$ = 4.5 ms/35.0 ms) with a varying contribution of slow decaying monoexponential signal with a signal intensity ratio from 0 % to 30 % ($T^*_{2,\mathrm{l}}$ = 54.0 ms). The resulting parameter estimates for A_0, $T^*_{2,\mathrm{s}}$, and $T^*_{2,\mathrm{l}}$ are depicted in **Figure 4.19**. The signal amplitude is captured more accurately by the optimized pattern which leads to a maximum deviation of less than 1 %. A bias of 3 % is found for the linear pattern. For both relaxation components, the linear pattern results in higher estimates. Especially, for the short component the two sampling schemes deviate in their parameter estimate by 11 % of the underlying $T^*_{2,\mathrm{s}}$. For the long component this deviation is only 3 % of the set value for $T^*_{2,\mathrm{l}}$. In general, an increasing signal contribution with slow relaxation behavior, as it is the case for CSF signal, results in an underestimation of the true signal amplitude of less than 3 %. Both relaxation components are observed with increasing values with a higher relative influence in the short component.

Measurement resolution and filtering: Influences on the T_2^* mapping

To demonstrate the advantage of acquiring data at higher resolution with subsequent Hamming filtering, **Figure 4.20** displays both T_2^* maps derived from a measurement with 4 mm nominal resolution and one with 2.8 mm. All other sequence parameters were kept constant (cf. **Table 4.7**). The 4 mm acquisition is shown with and without Hamming filtering before image reconstruction (cf. **Figure 4.20**, A and B) and the 2.8 mm acquisition with filtering (cf. **Figure 4.20**, C). At lower resolution, Gibbs ringing artifacts occur in the parenchyma. These can be suppressed by applying a Hamming filter. However, this results in a loss of resolution. At the higher resolution and additional filtering no ringing artifacts are visible. To evaluate the influence of resolution and filtering, the mean relaxation times from a segmentation of WM and CSF are displayed in **Figure 4.21**. It can be recognized that the observed T_2^* values in CSF decrease for the low resolution data from 60.1 ms to 51.4 ms if Hamming filtering is applied. At the same time, the value of $T^*_{2,\mathrm{s}}$ in WM increased from

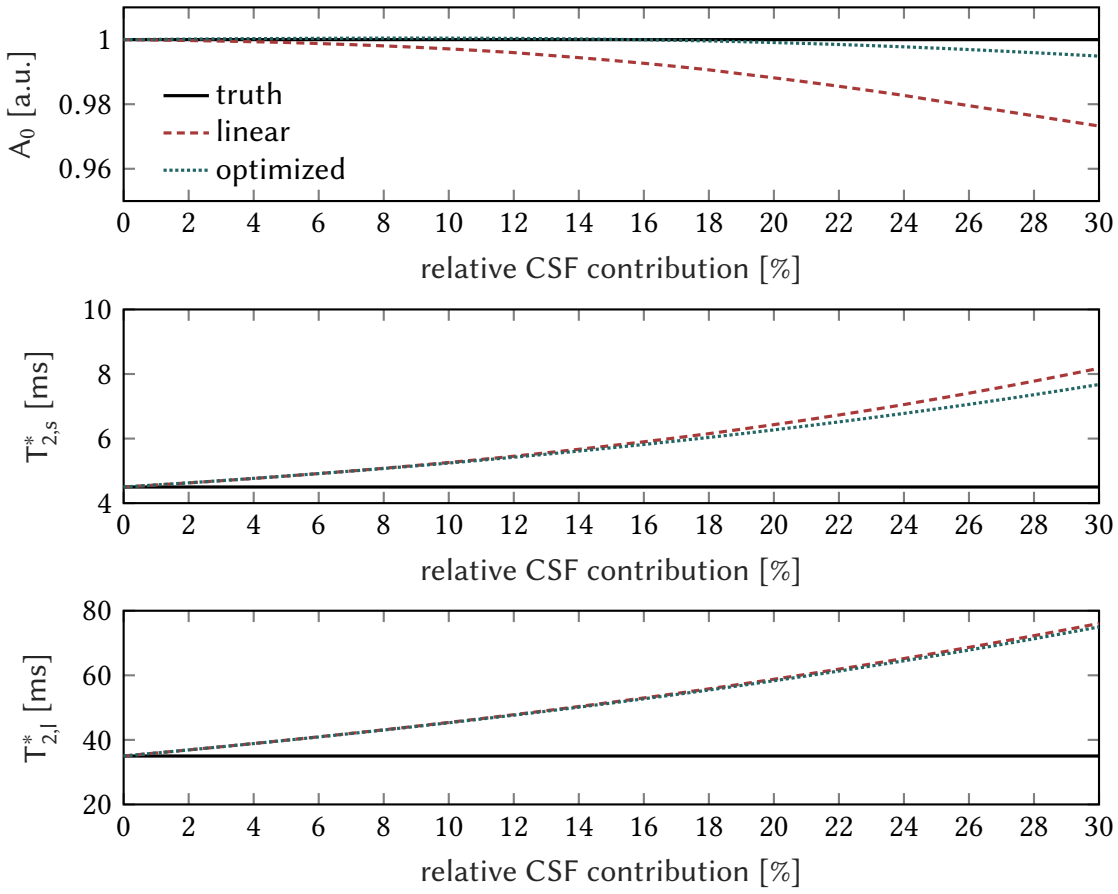

Figure 4.19: Change in parameter estimation of biexponential signal in case of CSF contribution for the linear and optimized pattern. The actual signal amplitude (black line) is captured more accurately by the optimized pattern. Both decay components increase with higher CSF contribution. For $T_{2,s}^*$, a larger value is determined by the linear pattern compared to the optimized scheme. This difference increases for higher CSF contribution.

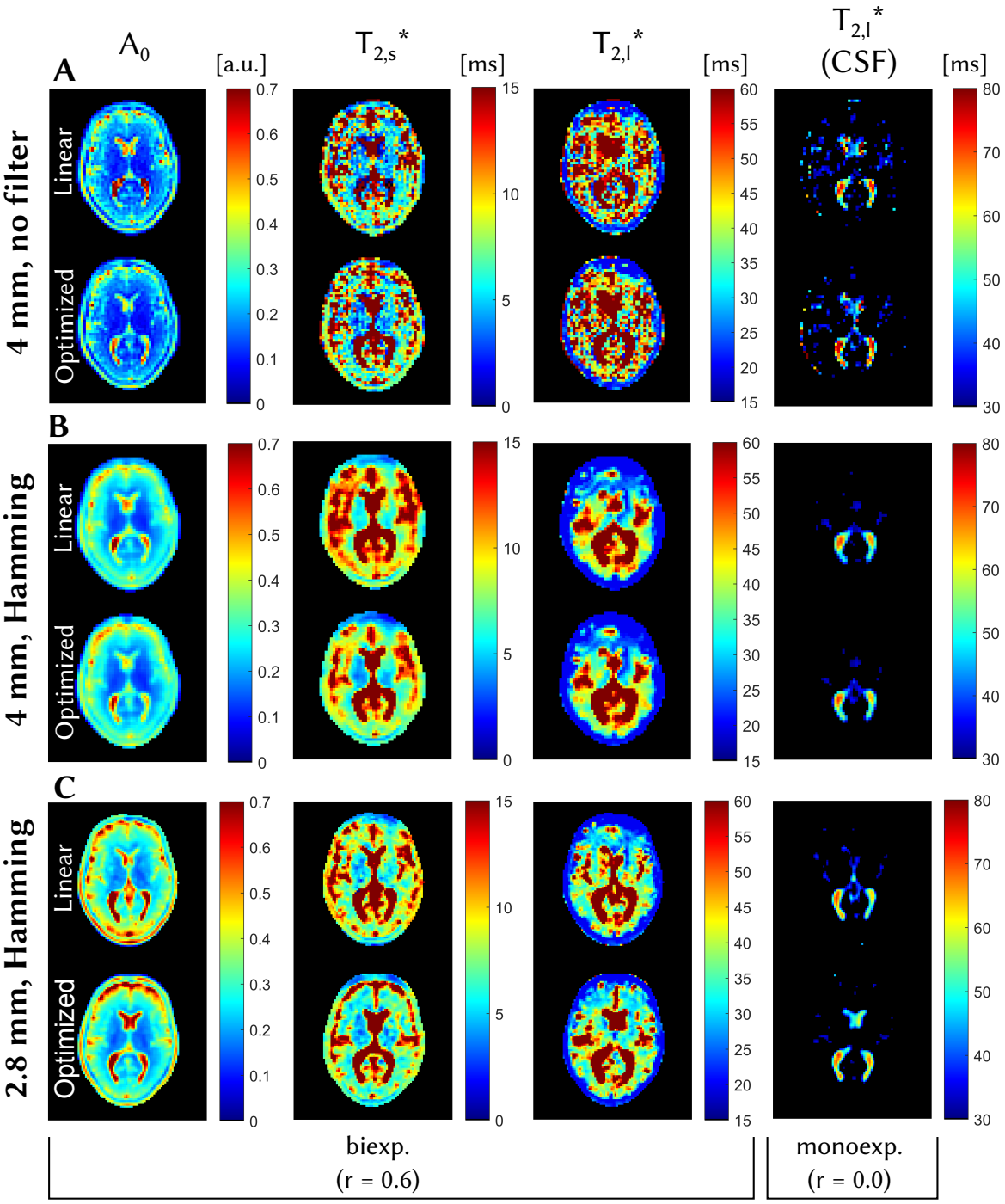

Figure 4.20: Comparison of the influence of nominal spatial resolution and Hamming filtering on the parameter maps. Shown are data with 4 mm nominal resolution without and with Hamming filter (A and B) and a 2.8 mm acquisition with Hamming filtered reconstruction (C). The unfiltered data show ringing artifacts which can be reduced by filtering. However, this leads to a blurring of the PSF which can be compensated by acquiring higher resolution data but still filtering the data.

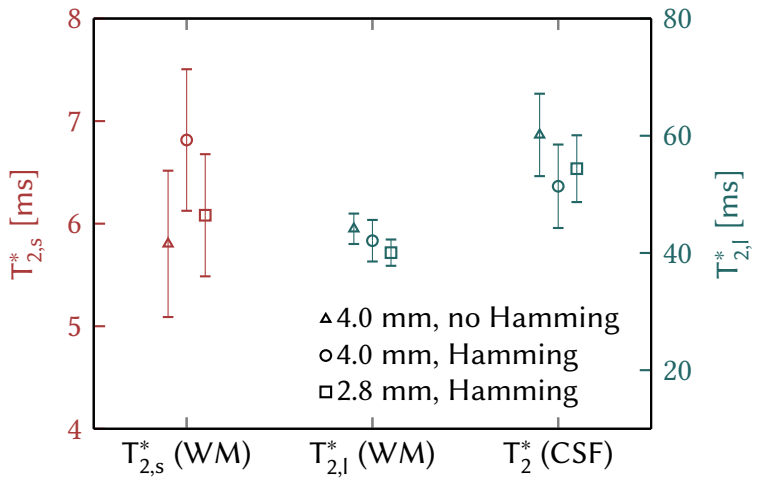

Figure 4.21: Relaxation times in WM and CSF segmented from the data presented in Figure 4.20 (resolution of 4 mm w/ and w/o filtering and 2.8 mm w/ filtering). Filtering of the low resolution data leads to signal blurring from the CSF compartment into WM. As a result, the CSF relaxation time is underestimated (orange triangle and circle) and the values in the parenchyma are overestimated (blue triangle and circle). The loss in resolution can be compensated by acquiring the data at a higher resolution (squares).

5.8 ms to 6.8 ms. If the data are acquired at higher resolution, the effect of the broadening of the PSF is compensated resulting in a value of $T^*_{2,s} = 6.1$ ms in the WM compartment. This value is still slightly higher than the 4 mm measurement but is in accordance within the measurement uncertainty.

4.2.4 Determination of the correlation time from T_2^*

In the case of dominating quadrupolar interaction, the correlation time of the interaction between ^{23}Na ions and the external electrical field gradient can be determined by the ratio of fast and slow relaxation components. The correlation time was calculated from the ratio $R = T^*_{2,l}/T^*_{2,s}$ by using the formula

$$\tau_c = \frac{1}{2\sqrt{2}} \sqrt{\frac{\sqrt{25R^2 - 58R + 49}}{\omega_0^2} + \frac{5R}{\omega_0^2} - \frac{9}{\omega_0^2}} \quad . \tag{4.1}$$

This relation is the positive solution of the quadratic equation resulting from the ratio of the equations for the short and long relaxation times (cf. Equation 2.49 given in Section 2.1.4).

Correlation times of ^{23}Na in brain tissue

Spatially resolved maps of the correlation time are depicted in **Figure 4.22**. These maps were

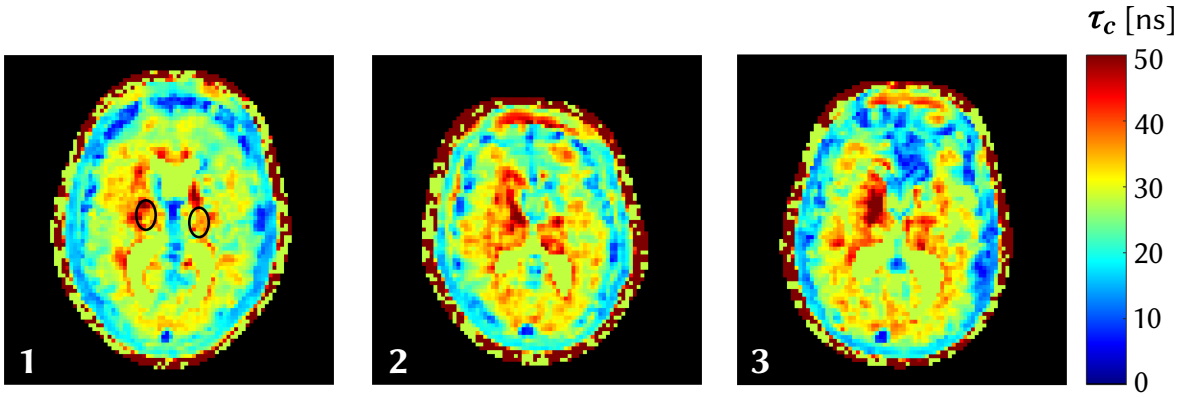

Figure 4.22: Maps of the apparent correlation time τ_c for three healthy volunteers. Values were determined from a measurement of the optimized pattern. For all three subjects a slight asymmetry between left and right hemisphere appears to be present. The locations of the ROIs used for the evaluation are depicted in volunteer 1.

determined from the T_2^* data acquired with the optimized pattern (cf. Section 4.2.2). Highest values of τ_c are found in WM regions close the ventricle. Towards tissue borders with CSF, an increase of the values is observed as well. Going from the center to the brain periphery, the observed correlation time gradually declines. In the CSF of the lateral ventricles, a constant value of 27.9 ns is found, which is not valid since the biexponential model is not applicable in liquids. A slight asymmetry between the left and right hemisphere appears to be present. An ROI analysis was performed in the WM located left and right of the lateral ventricles. For the three volunteers, the mean correlation times were 35.5 ± 3.8 ns, 40.6 ± 3.8 ns, and 43.1 ± 6.3 ns. The mean value over all three volunteers was determined to be 39.3 ± 2.5 ns. The resulting correlation times for the left and right hemisphere are depicted in **Figure 4.23**. The values of the correlation times are shown in **Table 4.10**.

The respective base parameters are shown in **Figure 4.24**. The asymmetry is also visible in the A_0 as well as $T_{2,\mathrm{l}}^*$. $T_{2,\mathrm{s}}^*$ does not exhibit this trend. The variation of the data in the evaluated ROI is larger than the discrepancy between the values.

Table 4.10: In vivo correlation times in three healthy volunteers. Given are values in an ROI in WM located left and right of the lateral ventricle (cf. Figure 4.22).

	correlation time τ_c [ns]		
Volunteer	#1	#2	#3
left	36.8±6.3	41.9±6.3	48.2±12.7
right	34.2±5.1	38.1±5.1	36.8±3.8
intra volunteer mean	35.5±3.8	40.6±3.8	43.1±6.3
total mean		**39.3±2.5**	

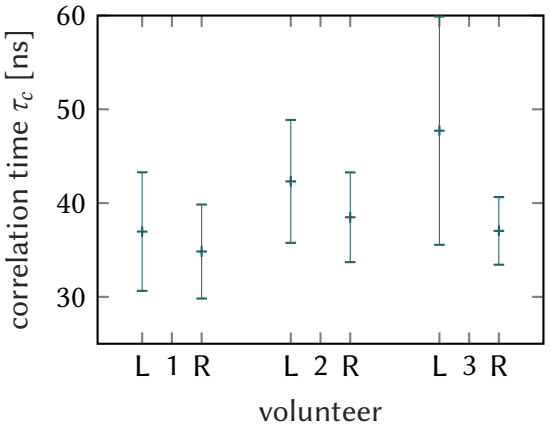

Figure 4.23: Correlation times of three healthy volunteers in units of ω_0^{-1}. The data were determined in an ROI in WM located left and right of the lateral ventricles. The mean value over all subjects is 3.1±0.2.

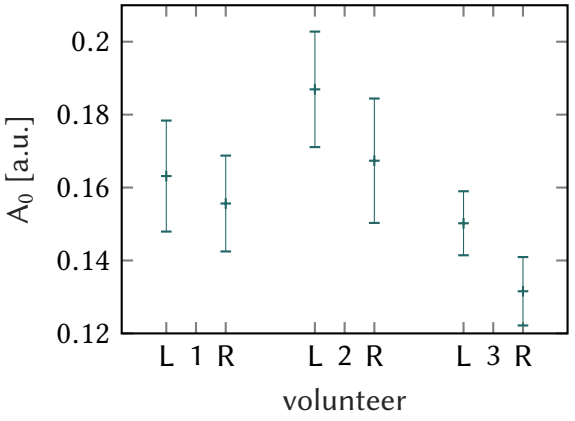

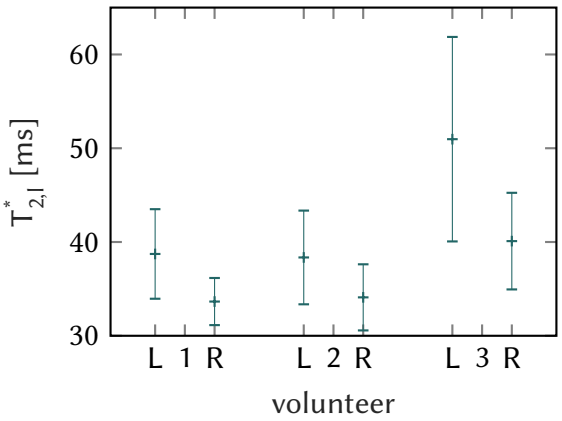

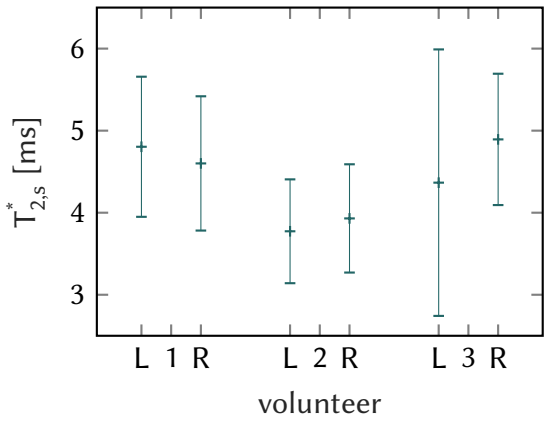

Figure 4.24: The base parameters $T^*_{2,s}$ and $T^*_{2,l}$ for the calculation of the correlation times. Additionally, the amplitude A_0 is shown as well.

Correlation times of ^{23}Na in agarose phantoms

For the purpose of comparison to the in vivo results, correlation times were determined in agarose phantoms. These are often used to imitate tissue environment. The relaxation was measured in seven phantoms containing 1 %–7 % agarose concentration (cf. Section 3.1.1). The measurement parameters are given in **Table 4.11**. The correlation times are shown as a function of the agarose concentration in **Figure 4.25** and are given in **Table 4.12**. The observed correlation times exhibit a monotonic rise as function of the agarose concentration. At around 4 % the slope becomes lower and the values of 5 % and 6 % are almost the same.

Table 4.11: Acquisition parameters for phantom relaxation measurement.

Parameter		**Value**
Sequence		ME DA 3D-RAD
nom. resolution	Δx	4 mm
max. gradient amplitude	G_0	7.55 mT/m
projections	N_{proj}	7050
radial samples	#RadSamples	384
echo time	TE	linear patter (cf. Section 3.2.2)
repetition time	TR	120 ms
readout duration	T_{RO}	5 ms
flip angle	α	90°
pulse length	t_p	600 µs
acquisition time	T_{AQ}	4 × 14:07 min

Table 4.12: Correlation times measured in agarose phantoms. The uncertainty of the value in the phantom with 1 % agarose is increased compared to higher concentrations. The assumption of one single compartment might not be fulfilled.

Agarose [%]	τ_c **[ns]**
1	14.9±1.2
2	21.5±0.6
3	26.5±0.7
4	28.5±0.7
5	31.0±0.8
6	31.6±0.9
7	33.8±0.7

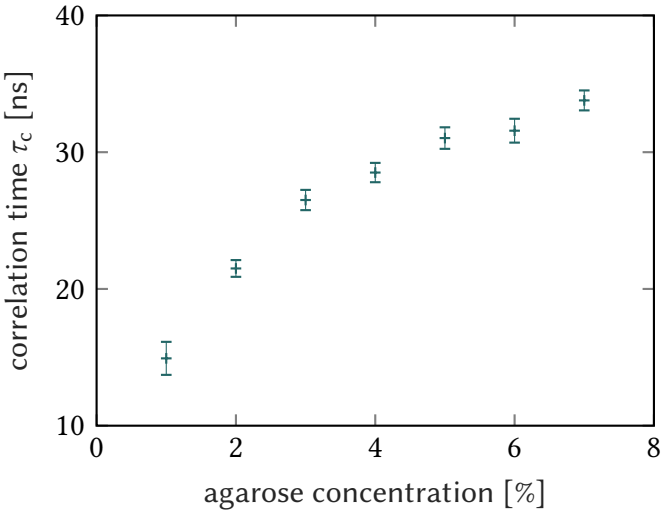

Figure 4.25: Correlation times in agarose as a function of agarose concentration. A linear relation would be expected if the agarose concentration had a linear influence on the correlation time. This is not the case for concentration higher than 4 %.

5 Discussion

The aim of this work was the efficient and accurate quantification of the T_2^* decay of the ^{23}Na MRI signal in vivo. The observation of the ^{23}Na signal relaxation is challenging due to low SNR and a fast biexponential decay in the order of a few milliseconds. The origin of the rapid relaxation is the electric quadrupole moment of the nucleus which enables an additional interaction path via electric field gradients present in the ionic environment. To this end, the signal relaxation represents a direct probe into the microscopic surrounding through electric interaction. The information contained in the decay properties with regard to biological tissue is still not fully understood but is assumed to be linked to the location of the ions relative to the cell. Having in mind, the major regulatory role of ^{23}Na ions when transported between intra- and extracellular space for the purpose of signal conduction and cell homeostasis, further understanding of the relaxation characteristic could add another layer of information to the imaging of this nucleus, which exhibits second best MRI properties after ^{1}H in the human body.

In brain tissue, the concentration of ^{23}Na ions is about 40 mM [Niesporek et al., 2015]. This low abundance is the main reason for the SNR of ^{23}Na MRI being four orders of magnitude lower compared to imaging of the ^{1}H nucleus [Madelin and Regatte, 2013]. In the past, mostly concentration measurements were performed using spin-density weighted sequences and are still considered challenging in the clinical context. The concentration was reported to be a measure of cell viability and is a useful parameter in the research of neurodegenerative diseases and tumor response. Due to the overall importance of ^{23}Na in cells, further studies showed wide-spread applications in muscle and cartilage, heart, kidney, and others [Madelin and Regatte, 2013]. The additional observation of the signal decay is even more challenging than the acquisition of a single image. Therefore, first in vivo T_2^* measurements were performed using global FID sampling [Nordenskiold et al., 1984; Cope, 1970]. Higher field strengths and more efficient readout schemes led to increased SNR and in turn allowed compartment-wise T_2^* determination [Nagel et al., 2011], or even voxel-wise fitting [Lu et al., 2011; Blunck et al., 2017]. Nevertheless, the low SNR still restricts reliability as well as detailed analysis of the signal behavior.

The large variations in previous reports of ^{23}Na T_2^* in brain tissue demonstrate the existence of influences on the parameter estimation which have not been completely explained yet. A summary of 14 studies reporting T_2 or T_2^* values for ^{23}Na of brain parenchyma is given in **Table 2.3**. Reported values range from 0.2 ms to 5 ms for $T_{2,\mathrm{s}}^*$ and from 10 ms to 64 ms

for $T_{2,l}^*$. The shown biexponential relaxation times exhibit an apparent rise with the field strength as expected from theory [Nagel et al., 2016]. However, even when only considering studies at 7 T, a variation from 2 ms to 5 ms is found for $T_{2,s}^*$. Also, a medium T_2 = 3 ms measured with a spin-echo sequence was reported in rats at 9.4 T [Winter and Bansal, 2001]. $T_{2,l}^*$ is often considered to be detectable with higher accuracy since a higher sampling rate can be achieved ($T_{RO} < T_{2,l}^*$). Still, a large spread of values between 22 ms and 40 ms was reported at 7 T. The even longer decay time of CSF was reported with values ranging from 47 ms to 57 ms at 7 T and 64 ms at 4 T. Influences which could lead to this spread are likely due to several reasons which could involve the experimental setup (shimming), the acquisition (sequence, sampling scheme), as well as the evaluation and post processing (segmentation, reconstruction, filtering, fitting procedure). In this work the sampling scheme and the post preprocessing were investigated.

The sampling of ^{23}Na T_2^* faces a trade-off between two main challenges: low SNR and a fast biexponential signal decay in the range of or even shorter than T_{RO} (T_{RO} = 2 ms to 20 ms, and mostly $T_{RO}/T_{2,s}^* \geq 1$). Consequently, the acquisition of sufficient information about the decay during one *TR* requires multiple repetitions of a multi-echo measurement. The topic of relaxation quantification has been investigated for ^{1}H imaging and dedicated sampling schemes have been developed and analyzed in detail [Poon and Henkelman, 1992; Jones et al., 1996; Anand et al., 2009; Uddin et al., 2013; Linnet and Teilum, 2016]. Acquisition schemes range from linear sampling to logarithmic patterns towards more sophisticated schemes as proposed by Jones et al. [1996]. The latter authors used the Cramér-Rao theory to analytically solve for an optimal sampling scheme for a specific T_2. Dula et al. [2008] also applied the Cramér-Rao theory to the question of optimal receiver bandwidth in the case of biexponential decay. However, these results cannot be transfered directly to ^{23}Na MRI due to the lower SNR and different relaxation behavior. Due to the biexponential decay straightforward T_2 determination from signal ratios [Haacke et al., 1999] can only be applied to the long component by using long *TE* as demonstrated by Fleysher et al. [2009]. Furthermore, conventional fast transverse relaxation time (T_2) sampling schemes such as Carr-Purcell-Meiboom-Gill [Poon and Henkelman, 1992; Pell et al., 2006] are not applicable to ^{23}Na MRI due to high SAR and increased echo spacings. Additional refocusing pulses lead to an increase of *TE* and $T_{2,s}^*$ cannot be resolved anymore. Thus, most studies focus on T_2^*. In the case of rapid relaxation $T_2 \approx T_2^*$, since for the short transverse relaxation times and the low gyromagnetic ratio of ^{23}Na ($\gamma_{Na} = \gamma_H/3.7$) dephasing due to field inhomogeneities is assumed negligible. However, deviations from this assumption have been reported for brain areas exhibiting irregular shape and susceptibility changes such as the sulci [Niesporek et al., 2017]. There, deviations of up to 56 % can occur for moderate field inhomogeneities. In the parenchyma, only small deviation of less than 10 % are expected. To this end, careful shimming is of high importance for T_2^* determination.

The aim of this work was to enable a more efficient and accurate quantification of the fast biexponential decay of the ^{23}Na MRI signal. To this end, the temporal distribution of

sampling points was analyzed with respect to resolution of the different decay components. A dedicated sampling scheme was developed for brain parenchyma employing numerical optimization. Bias and uncertainty of T_2^* quantification was investigated for different SNR values and fitting approaches. The image SNR could be significantly improved by the utilization of a novel 30-channel array coil. Finally, two sampling schemes were compared in vivo and T_2^* values for different brain compartments could be determined. From the relaxation components the correlation time τ_c was calculated which governs the interaction of the ^{23}Na ions in tissue.

5.1 Improved SNR efficiency via a multi-channel coil

In the course of this work, a novel 30-channel array coil for ^{23}Na imaging could be put in operation. The advantage of multi-channel coils is applied for ^{1}H MRI as a standard but is not that common in X-nuclei imaging due to lower demand and higher costs. For ^{23}Na MRI, the use of a receive array comes with a complication when measuring concentrations due to an intensity modulation caused by the receive profile of the array. In this work, the aim was the quantification of the T_2^* decay, where only the relative signal decay is of interest. Thus, the sensitivity profile did not create difficulties.
The 30-channel array was compared to a conventional ^{1}H/^{23}Na birdcage coil present at the site. Two types of multi-channel reconstruction were furthermore investigated: the sum-of-squares approach and adaptive channel combination. Compared to the birdcage coil, the new 30-channel array yielded a factor 2.5 SNR increase in the brain periphery and only a slight loss in the coil center by a factor of 0.9. The excitation field profile of the array coil showed comparable homogeneity to the birdcage coil. A small gradient in the field profile of 7 % was observed from left to right in the axial view. This gradient is probably due to the more complicated wiring of the coil which includes the 30-channel array inside of the excitation birdcage. The B_1^+ efficiency of the coil is lower by about 30 % if only considering global signal maximization which is mostly done for the flip angle calibration. Since the actually applied pulse voltage is mostly limited by hardware constraints, this can have an effect on the excitation pulse length. In case of rapidly decaying signal, this could be disadvantageous. However, for the relaxation times measured in this work, this represents a signal loss of a few percent and is compensated by the strong SNR gain through the use of the array geometry. The noise correlation of the coil (mean/maximum 13 %/50 %) was comparable or lower than previously reported for multi-channel sodium coils. For a 30-channel coil at 3 T 17 %/84 % were obtained [Benkhedah et al., 2016] as well as 9 %/54 % for a 27-channel coil built for 9.4 T [Shajan et al., 2016]. In the SNR comparison of the two reconstruction approaches, the AC method resulted in a 13 % higher value close to the coil elements. This is lower than reported by Benkhedah et al. [2013a] (50 %), which is likely due to the lower noise correlation of the utilized coil. The AC reconstruction exhibits the

additional advantage of retaining the signal phase as compared to the SOS combination which yields a magnitude image.

5.2 Optimization of the temporal sampling

Due to the rapid signal decay, center-out FID sampling strategies are most appropriate for ^{23}Na MRI [Boada et al., 1997; Gurney et al., 2006; Nagel et al., 2009]. In these sequences, the acquisition time of each echo can be shifted arbitrarily to a later time point. This is useful to capture the specific shape of the signal. However, it also renders the search for a dedicated pattern more complicated. On the acquisition side, various interdependent parameters had to be optimized to develop a dedicated sampling scheme: the echo time TE_i of each sampling point in each multi-echo acquisition, the number of repetitions N_{reps}, the T_{RO}, and the repetition time TR.

5.2.1 Base pattern of the optimization

Since SNR is the major constraint in ^{23}Na imaging, it was employed as a central parameter in the optimization process. The starting point for the optimization of sampling was to avoid dead times during the acquisition. Therefore, a base readout scheme was set. It constituted a multi-echo readout starting immediately after the excitation without delays between the acquired echoes. For a specific signal course there might exist an optimal distribution of sampling points to capture the decay parameters most accurately as shown for ^{1}H imaging [Jones et al., 1996; Fleysher et al., 2008]. This might be especially important for $T^*_{2,\text{s}}$. To this end, multiple acquisitions of this equidistant sampling were repeated but shifted by ΔRep_i. The parametrization via these shifts allows tuning the sampling scheme to the optimal trade-off between reliability and accuracy for a given decay and SNR. For example, higher reliability can be achieved by averaging or a better temporal resolution by denser sampling (e.g. linear sampling).

5.2.2 Minimum SNR for parameter estimation

To determine the minimum SNR needed for fitting a biexponential decay, the fit quality was analyzed for different noise levels. An SNR of 15 was concluded to be the minimum requirement to retrieve a reliable parameter estimate, since at this point systematic bias decreases below 5 % and the variation of $T^*_{2,\text{s}}$ is less than 20 %. These results were applied as basis for the sequence parameters in the in vivo study which were adjusted such that an SNR of approximately 15 was obtained in WM.

5.2.3 Optimization procedure

The evaluation of parameter estimation of the biexponential decay is ambiguous since multiple model parameters exist. To this end, a single evaluation measure was designed, which captures both uncertainty and bias for all three fit parameters. This metric is a function of the sampling pattern and was therefore used to optimize the sample distribution. This was performed using a global multi-start approach.
There exist two drawbacks of the presented method. First, the sampling of the fitting statistics via the N repetitive fits for the calculation of the metric can only give an estimate of the true value distribution. This can lead to prolonged duration of the optimization as well as to convergence towards local minima. However, the probability of local minima was reduced by the application of a multi-start optimization algorithm. Secondly, the quality metric Q is not strictly convex. In case of either 0 % bias or 0 % uncertainty it becomes zero and the optimization could stop at this point. However, this degenerate case did not occur during the presented optimization. In future applications, it could be captured and this path of the optimization could be restarted at another point. Furthermore, slightly better solutions might be found using more initialization points in the multi-start algorithm. Despite these drawbacks, it is straightforward to implement and can be generalized to a variety of SNR and decay environments.
In the presented metric, the fit amplitude A_0, $T_{2,\mathrm{s}}^*$, and $T_{2,\mathrm{l}}^*$ were weighted equally. Since the accuracy of $T_{2,\mathrm{l}}^*$ is not impacted as strongly by the acquisition scheme, a stronger weighting of $T_{2,\mathrm{s}}^*$ could be applied without degradation of $T_{2,\mathrm{l}}^*$. This might be of interest in applications where pathological changes are reflected mostly in one of the two decay components as reported for the long component in cartilage [Regatte et al., 1999].

5.2.4 Properties of the developed sampling distribution

The sample distribution obtained by the optimization procedure is determined by four repetitions of the linear base scheme with a shift of $\Delta\mathrm{Rep} = [0.0, 0.0, 0.0, 4.1]$ ms. Thus, the pattern consists of 3 averages at the earliest possible TE and one additional point at $TE = TE_{\mathrm{min}} + 4.1$ ms. This is comparable to the findings by Jones et al. [1996] in the context of ^{1}H MRI. Their scheme increases reliability for the monoexponential case by placing one sample at the earliest possible $TE = TE_{\mathrm{min}}$ and four at $TE = 1.28 \cdot T_2$. Thus, the sample with lower SNR is averaged to retrieve comparable reliability of both time points. For ^{23}Na MRI, averaging is also superior to denser temporal sampling. However, the findings of the presented work suggest an inverted averaging pattern with focus on the first point compared to the results of Jones et al. [1996]. This can be explained by the low SNR of ^{23}Na where a reliable definition of the earliest sample is crucial for the determination of the decay curve. When compared to the T_2^* times which were set in the optimization, the intermediate sample is placed at $TE = 0.82 \cdot T_{2,\mathrm{s}}^*$, or when described by the ratio of the short and long component at $TE = 32.8\,\mathrm{ms} \cdot T_{2,\mathrm{s}}^*/T_{2,\mathrm{l}}^*$. This deviates from the scheme described by Jones et al. [1996] where the second sample is placed at $1.28 \cdot T_2$. However, the optimization was carried out

for biexponential decay and lower SNR. Therefore, deviations are expected. Apparently, the focus is set more on rapid decay of $T_{2,s}^*$ by an early sampling point. The smaller factor relating decay and sample time can be further understood by the fact that $T_{2,l}^*$ is already sufficiently sampled as demonstrated by the small variation of bias and uncertainty for different sampling schemes (cf. **Figure 4.10**, **4.11**, and **4.12**). An earlier intermediate point might also be beneficial to separate the two decay components.

5.2.5 Comparison to alternatives schemes

The developed scheme was compared to four alternative patterns by signal simulations over a wide range of decay constants and SNR. The evaluation revealed that the quality of T_2^* measurements is a complicated function of the sampling scheme and the specific relaxation times. A trade-off between accuracy and reliability could be recognized by the fact that the standard deviation of schemes, which include averaging (optimized, averaging, Jones et al.), is lower around medium T_2^* values (cf. **Figure 4.11**). However, for schemes with sampling points at early *TE* (linear, early TE), a better resolution of very short $T_{2,s}^*$ is found (cf. **Figure 4.10**). The optimized sampling pattern allows for a reliable sampling with the capability to resolve short $T_{2,s}^*$. The linear scheme did show the second best overall performance and was therefore also tested in the in vivo measurements.

5.3 Influence of the fitting procedure

At low SNR, noise energy contributes systematically to the signal amplitude as described by the Rician distribution [Gudbjartsson and Patz, 1995]. This additional contribution can be taken into account in the fitting model. To this end, three models were investigated with regard to accuracy for different SNR and number of measurement points. The latter are essentially determined by *TR*. Generally, the applicability of the different models was found to be dependent on the acquisition scheme and the SNR. One single best method could not be determined (cf. **Figure 4.14**). At low maximum sampling times $TE_{\max} < 80\,\text{ms}$, the influence of the noise contribution is small and can either be neglected or included as a constant if the SNR is well-known. For data with additional sampling points at late $TE > 80\,\text{ms}$, the noise floor has to be taken into account to prevent a systematic bias in the magnitude and $T_{2,l}^*$. For $T_{2,s}^*$, regardless of the model and the SNR, a slight overestimation is seen, which is a typical problem in multi-component fitting [Papy et al., 2009]. In case of low SNR ≈ 10, most reliable determination is achieved by minimizing the degrees of freedom of the fit by a model with constant noise term.
Since the SNR is low, additional open parameters generally decrease the reliability of the parameter estimate as seen for including an additional noise floor parameter. Thus, the inclusion of both an additional noise parameter as well as the ratio of the fast and slow decaying signal contribution can result in a degraded estimate. In this work, the contribution

of the short component was always set to 60 %. This might be a strong assumption but ensured comparability to previous studies which were obtained in the majority using this assumption. This is a common simplification representing only one pool of ^{23}Na ions and was recently affirmed in WM by Bydder et al. [2017]. However, in biological tissue a number of different binding states of ^{23}Na ions are present which are in constant exchange [Thulborn et al., 1999a; Regatte et al., 1999; Payne and Styles, 1991]. It has also to be noted, that in the case of extremely short $T_{2,s}^*$, a significant signal amount decays during the excitation pulse. This can lead to systematic bias of the relaxation estimates. It could be taken into account by including a model of the signal decay during the excitation pulse into the fitting procedure [Stobbe and Beaulieu, 2005; Johnson et al., 2017].

5.4 In vivo T_2^* observation in healthy human brain

In vivo T_2^* mapping was conducted in three healthy volunteers both with the optimized and the linear pattern in order to determine the potential variation due to different sampling strategies. For all volunteers the optimized pattern resulted in lower $T_{2,s}^*$ values in WM compared to the linear scheme (mean: 5.1 ± 0.8 ms vs. 4.2 ± 0.4 ms, cf. **Figure 4.9**). This systematic deviation between the two schemes is confirmed by the presented simulations, where a slight overestimation is found for the linear pattern and a smaller underestimation for the optimized scheme (cf. **Figure 4.10**). The optimized sampling allows a more accurate determination of the first point which is crucial for the quantification of $T_{2,s}^*$. Together with lower standard deviation and a lower bias found in the simulation study, it is concluded that values from the optimized pattern are more reliable. The T_2^* values in CSF exhibit a rather large uncertainty amongst the volunteers. This can be explained by remaining partial volume effects at tissue borders and stronger field inhomogeneities in the area of the sulci as demonstrated by Niesporek et al. [2017]. It has to be noted, that registration and segmentation can cause an additionally variation, which is not actually present in the data. Still, the results of the two sampling schemes agree within the uncertainty for $T_{2,l}^*$ in CSF. The in vivo $T_{2,s}^*$ maps obtained with the linear pattern exhibit a gradient towards the brain periphery, which is probably due to CSF contamination (cf. **Figure 4.18**). The linear pattern was demonstrated to be more susceptible to CSF contamination which explains higher $T_{2,s}^*$ (cf. **Figure 4.19** and **Figure 4.20**). In tissue adjacent to the lateral ventricles, CSF contamination is smaller compared to the cortex. The strongest difference between the two sampling patterns was observed in WM close to the lateral ventricles (cf. ROI data, **Table 4.9**). This is probably due to the fact, that there residual effects are smallest due to the rather large extent of this compartment. In future, the effect of liquid contamination could be investigated by comparison of two measurements, one with and one without a liquid suppressing inversion pulse. First attempts have been reported for ^{23}Na in phantoms [Gilles, 2012] and was recently demonstrated in cartilage for ^{1}H imaging using a 3D cones readout [Ma et al., 2017].

Concerning the imaging parameters, Gibbs ringing artifacts occur in the parenchyma, which can lead to locally wrong relaxation estimates due to liquid contribution. These can be suppressed by applying a Hamming filter which results in a loss of resolution. This degradation of the PSF can be compensated by an acquisition with higher resolution and subsequent filtering. Due to the beneficial behavior of the Hamming filter, the resolution can be retained but a higher SNR is achieved [Konstandin and Nagel, 2013; Stobbe and Beaulieu, 2008a].

In summary, if only T_2^* values are of interest, relatively short TR (e. g. 60 ms to 70 ms) and low $TE_{\max}$ together with a fitting model neglecting the noise contribution are preferable for SNR efficiency. In the case of long $TR > 80$ ms and long $TE_{\max}$, e. g. for simultaneous concentration measurements, it is necessary to include a noise contribution. This can be done by estimating the image SNR as accurately as possible, e. g. from background voxels [Blunck et al., 2017; Bouhrara et al., 2015]. In future studies, the accuracy of ^{23}Na T_2^* measurements could benefit largely by using modern reconstruction techniques [Madelin et al., 2012; Gnahm et al., 2014; Gnahm and Nagel, 2015; Behl et al., 2016]. Also, the efficiency of the signal sampling could be further improved by applying a bipolar readout [Blunck et al., 2017]. However, in this work a monopolar readout was utilized, which is less susceptible to artifacts, since the same readout direction is used for all echoes. The use of a multi-echo readout instead of a single-echo acquisition was demonstrated to have negligible impact on the T_2^* estimate whilst being more time efficient [Niesporek et al., 2017].

The results of this study suggest that both, the fitting procedure and the sampling scheme strongly influence the observed relaxation times. This allows understanding certain aspects of the variation found across the literature. The $T_{2,\mathrm{s}}^*$ values in parenchyma observed in this study range between 4 ms and 5 ms similar to those reported by Nagel et al. [2011], Niesporek et al. [2017], and Bydder et al. [2017]. The values of the optimized pattern are lower than those of the linear scheme. In comparison, the values of Blunck et al. [2017] and Lu et al. [2011] are significantly shorter (2 ms and 0.3 ms to 3.0 ms). These studies employed different readout parameters such as longer TR and shorter T_{RO}. However, the $T_{2,\mathrm{l}}^*$ in CSF are reported consistently along previous studies with values around 55 ms. During the evaluation of the presented data a strong dependence of the fit results on the start values of the amplitude was observed especially at low SNR. Together with the results concerning the noise floor, which can lead to overestimates, it is concluded that the fitting procedure can have a strong impact on the parameter estimate. Parts of the variation across the literature could be due to this fact. The trajectories employed for ^{23}Na MRI (TPI [Boada et al., 1997], 3D cones [Gurney et al., 2006], DA 3D-RAD [Nagel et al., 2009]) are not expected to yield varying relaxation times when used with identical readout timings since the radial evolution in k-space is similar. From the apparent rise of the decay time in the literature, the assumption of $T_2 \approx T_2^*$ seems to be confirmed and speaks for a rather low influence of B_0 field inhomogeneities on the relaxation times.

5.5 Correlation time of quadrupolar interaction

In the case of dominating quadrupolar interaction, the correlation time between the ^{23}Na ions and the external electrical field gradient can be determined from the ratio between fast and the slow relaxation times. Thereby, the two observables can be traced back to the one single underlying parameter.

The correlation time was determined from the in vivo T_2^* measurements of the optimized pattern. A mean value of 39.3 ± 2.5 ns was found. This is equivalent to a value of 3.1 ± 0.2 in units of inverse Larmor frequency, which is in accordance with the underlying theory predicting a biexponential decay for $\tau_c\omega_0 \gtrsim 1$. In regions close to the lateral ventricles, a higher value of τ_c was found. This can be explained by an increased ratio $T_{2,\mathrm{l}}^*/T_{2,\mathrm{s}}^*$ due to partial volume effects (cf. **Figure 4.19**). An apparent asymmetry was found between the values in WM of the two hemispheres which, however, were still in accordance within the uncertainty. Together with possible systematic deviations in the measurement stemming from assumptions in the theory and in the evaluation, this effect cannot be considered significant. In the brain periphery, low values of τ_c were found. This is in accordance with the theory predicting lower correlation times in case of smaller interaction strength as is the average case for the superposition of liquid and parenchyma compartments in this area. However, due to this complicated composition of the signal, these values have to be seen critically and require further tests.

In order to compare the in vivo data to a simpler system, correlation times have also been determined in agarose phantoms with varying concentrations similar as done previously by Benkhedah [2013] and Gilles [2012]. The assumption is that in these systems the correlation time increases linearly with the agarose concentration due to restriction of the ion movement. In the experiments, the correlation times increased monotonically with the agarose concentration. However, a plateau-like behavior is seen at concentrations of 4 %. This could be explained by the fact that the spatial constraint for the ^{23}Na ions first increases linearly with increasing concentration but at a certain point, most of the ions are bound to the agarose molecules. Then, additional agarose does not change the correlation time further. Compared to the in vivo results, the correlation times of the agarose phantoms were lower by about 16 %. This could point to a stronger interaction of the ^{23}Na ions in vivo than in agarose models. However, due to more complicated composition of the in vivo signal, this interpretation would require further analysis. This could be done using more realistic model environments by adding proteins to the agarose phantoms which should approximate the in vivo situation more closely. Also, a multi-compartment model as employed by Payne and Styles [1991] would be a more realistic description. Correlation times have been published before for different model environments by Monoi [1976] who report values of 4 ns to 9 ns. For similar agarose phantoms used in the present work, comparable values ranging between 10 ns to 40 ns were reported [Benkhedah, 2013]. Nagel et al. [2016] determined slightly shorter values of about 1 ns for agarose models.

In the case of dominating quadrupole interaction both T_1 and T_2 are determined by τ_c. Therefore, an additional path for verification could be the observation of the correlation time via T_1. This has also the advantage of not being biased by B_0 inhomogeneities. However, to the knowledge of the author, the biexponential behavior of T_1 has not yet been observed in vivo. However, first attempts of measurement optimizations based on this relation were presented by Stobbe and Beaulieu [2005, 2008b]. It could be also interesting, to develop structural phantoms which mimic fibers as they occur in brain tissue. Thereby, the assumption of the rotational symmetric electric field gradient could be analyzed. Also, it would be insightful to compare the properties of the ^{23}Na signal decay with other methods, which can detect the actual position of the sodium ions inside the cell such as shift reagents [Gupta and Gupta, 1982; Winter and Bansal, 2001] or compare the signal of solutions containing different types and concentrations of cells similar to Nordenskiold et al. [1984] or Neubauer et al. [2017]. Due to the strong electro-chemical gradient, sodium ions are expected to be clustered close to the cell membrane [Alberts et al., 2002].

In summary, this work reports T_2^* quantification in the healthy human brain with the up-to-date highest resolution of nominal isotropic 2.8 mm. To achieve this, an SNR increase of more than a factor of two could be exploited by using a novel 30-channel array coil. The temporal signal sampling was optimized in order to minimize bias and uncertainty. By the analysis of a variety of different aspects which can result in deviations of the T_2^* estimate, parts of the variations across literature could be understood. From the measured relaxation times, the correlation time of the quadrupolar interaction of the ^{23}Na ions in biological tissue was estimated. Further research in this field combined with more efficient T_2^* measurements could be extremely insightful and potentially open up a number of applications, e.g. in the field of neurodegenerative diseases where sodium plays a crucial role as shown for multiple sclerosis or Alzheimer's disease [Zostawa et al., 2016; Vitvitsky et al., 2012].

6 Summary

Sodium (^{23}Na) ions play a crucial role in the physiology of animal tissue as they are an integral part of the signaling processes and required for maintaining cell homeostasis. Due to a nuclear spin of 3/2, the concentration of the ^{23}Na ions can be observed non-invasively by MRI and has become a growing tool in clinical research. However, a spin ≥ 1 also implies an asymmetric charge density of the nucleus, which opens up an additional interaction path with local electric field gradients. Dependent on the electric surrounding, this quadrupole interaction leads to a rapid biexponential decay of the NMR signal. The fast signal relaxation has long been an obstacle for the imaging of ^{23}Na but it also represents a probe into the microscopic environment of the ^{23}Na ions. Faster signal decay has been attributed to ions which are restricted in the intracellular space and undergo stronger interaction with surrounding macromolecules. The in vivo determination of the ^{23}Na signal relaxation could therefore yield specific information about the microscopic environment of the essential ion. However, the 20,000 times lower SNR compared to ^{1}H NMR together with readout bandwidths being in the order of the relaxation rate, render a reliable in vivo quantification challenging.

The aim of this work was to improve the quantification of the fast biexponential T_2^* decay of the ^{23}Na MRI signal in vivo. To this end, the temporal distribution of sampling points was analyzed and a dedicated sampling scheme was developed for brain parenchyma employing numerical optimization. Bias and uncertainty of relaxation measurements were investigated for different SNR values and fitting approaches. By utilization of a novel radio frequency coil, the image SNR could be significantly improved. Two sampling schemes were compared in vivo and T_2^* values were determined for different brain compartments. Finally, the correlation time τ_c that governs the interaction of the ^{23}Na ions in tissue was estimated from the relaxation components.

During this thesis, a novel 30-channel array coil could be put into operation which allowed an increased SNR efficiency compared to a 1-channel birdcage radio frequency coil. In the cortex, an SNR improvement of 145 % was determined. In the coil center, the SNR of both coils was comparable. A slight decrease of the excitation efficiency of 30 % is found due to the nested receive array. Furthermore, the application of adaptive channel combination allowed an SNR increase in the cortex of 13 %, when compared to sum-of-squares reconstruction. Complications due to a signal modulation with the sensitivity profile as present in concentration quantification do not arise for T_2^* measurements since only relative signal decay is of interest.

For the temporal distribution of the sampling points there exists a trade-off between reliability and increased resolution for short decay times. The latter can be achieved by a denser distribution of sampling times, while reliability through averaging. In order to adjust the sampling strategy to a specific SNR and decay environment, a parametrization of the sampling times was developed which assures SNR efficiency and is flexible to tune towards either reliability or accuracy. This was realized by shifted acquisitions of an efficient base pattern. This reduced the multi-parameter optimization to only two major variables: the SNR of the base pattern and the timings of the shifts.

To assess the quality of the T_2^* parameter estimation, a metric was developed which captures both reliability and accuracy for all decay parameters. This metric could then be used to numerically optimize the sample distribution. The resulting sampling scheme shows similar properties compared to previous reports for ^{1}H. This pattern was compared to four alternatives over a wide range of relaxation values, as well as for varying SNR. The optimized pattern is able to discriminate the two relaxation components more effectively compared to standard linear sampling as seen by a reduction of the mean bias from 3.0 % to 0.8 % for the short component and from 2.9 % to 2.6 % for the long component. Also, the reliability improved as demonstrated by a reduced parameter variation from 26 % to 22 %.

The low SNR of ^{23}Na MRI results in a systematic signal bias in magnitude data as determined by the Rician noise distribution which has to be considered in the fitting. To this end, three signal models were investigated for varying SNR and different number of samples. The results demonstrate that there exists not a single approach which is optimal for every type of acquisition. Rather, it is determined by the SNR and *TR*, which determines an upper limit for the largest *TE*. For short $TE < 80$ ms, the noise contribution can be neglected. However, if data are sampled until later *TE*, the noise contribution has to be taken into account via a priori information or fitting of the noise floor to avoid an overestimation of the long component. The presented analysis showed that by an appropriate choice of the signal model, typical overestimates of 15 % can be reduced to under 5 %.

The combination of hardware advances together with the improved sample distribution allowed the in vivo T_2^* mapping of ^{23}Na with an isotropic nominal resolution of 2.8 mm. For T_2^* measurements, this is up-to-date the highest reported resolution. In order to determine the dependence of the observed T_2^* values on the sampling strategy, in vivo measurements were conducted in three volunteers with both a linear and the optimized pattern. In white matter, the average short component was determined to be 5.1 ± 0.8 ms and 4.2 ± 0.4 ms for the linear and the optimized pattern, and for the long component 35.7 ± 2.4 ms and 34.4 ± 1.5 ms were observed, respectively. The values in CSF were in accordance within the uncertainty being 53.6 ± 6.9 ms and 54.4 ± 5.7 ms. The optimized pattern resulted in generally lower values. The results of the simulation study suggest that these values are closer to the actual relaxation times. In white matter, the optimized sampling strategy

resulted in a 29 % reduction of the mean variation in the short component. Concerning a comparison to the literature it has to be noted that a high variation in the reported values was found. Still, the measured relaxation times are in accordance with recent studies. Even though the presented work allows explaining significant aspects of the variation across literature, experimental validation by studies with larger populations is required.

For a pure quadrupolar interaction, the ratio between short and long component is solely determined by the correlation time of the ^{23}Na ions with respect to the electric field gradient. Through this relation, a spatially resolved map of the correlation time in brain parenchyma could be estimated. The mean value in white matter was found to be 39.3 ± 2.5 ns. For comparison, τ_c was also determined in agarose phantoms. A lower value of 28.5 ± 0.8 ns was observed in 4 % agarose, which could point to a stronger interaction in biological tissue than in the simple environment of the phantoms.

To conclude, this work represents an in vivo study of the T_2^* relaxation in ^{23}Na MRI. A dedicated sampling scheme was developed for the fast biexponential decay of the low SNR signal and the impact of different sample distributions was studied. Together with a novel 30-channel array coil, in vivo T_2^* mapping was achieved with a nominal resolution of 2.8 mm. First steps could be taken towards a deeper understanding of the signal decay by estimating the correlation time of ^{23}Na ions in brain parenchyma. Future studies could further analyze the connection between relaxation and the signal percentage arising from intra- and extracellular ^{23}Na ions. With this work, progress could be made towards a further understanding of the potentially valuable information connected to the quadrupolar relaxation of the in vivo ^{23}Na MRI signal being an additional contrast that is not present in standard ^{1}H imaging or ^{23}Na concentration measurements.

Bibliography

Alberts, B., Johnson, A., Lewis, J. (2002). *Molecular Biology of the Cell*. New York: Garland Science, 4. Aufl. Available from: https://www.ncbi.nlm.nih.gov/books/NBK26910/.

Anand, C. K., Bain, A. D., Sharma, A. (2009). Optimized sampling patterns for multidimensional T2 experiments. *J Magn Reson*, **197**(1):63 – 70.

Bartha, R., Menon, R. S. (2004). Long component time constant of 23Na T2* relaxation in healthy human brain. *Magn Reson Med*, **52**(2):407–410.

Behl, N. G., Gnahm, C., Bachert, P., Ladd, M. E., Nagel, A. M. (2016). Three-dimensional dictionary-learning reconstruction of 23Na MRI data. *Magn Reson Med*, **75**(4):1605–1616.

Benkhedah, N. (2013). *Biexponentiell gewichtete 23Na-Magnetresonanz-Tomographie*. Dissertation, Universität Heidelberg.

Benkhedah, N., Bachert, P., Nagel, A. M. (2013a). Biexponentially weighted sodium imaging with higher SNR efficiency. In *Proceedings of the ISMRM*, S. 1992.

Benkhedah, N., Bachert, P., Semmler, W., Nagel, A. M. (2013b). Three-dimensional biexponential weighted 23Na imaging of the human brain with higher SNR and shorter acquisition time. *Magn Reson Med*, **70**(3):754–765.

Benkhedah, N., Hoffmann, S. H., Biller, A., Nagel, A. M. (2016). Evaluation of adaptive combination of 30-channel head receive coil array data in 23Na MR imaging. *Magn Reson Med*, **75**(2):527–536.

Bernstein, M. A., King, K. F., Zhou, X. J. (2004). *Handbook of MRI Pulse Sequences*. Boston: Elsevier.

Besta, R., Shankar, Y. U., Kumar, A., Rajasekhar, E., Prakash, S. B. (2015). MRI 3D CISS–A novel imaging modality in diagnosing trigeminal neuralgia–A review. *Journal of Clinical and Diagnostic Research : JCDR*, **10**(3):ZE01–ZE03.

Bloch, F. (1946). Nuclear induction. *Phys Rev*, **70**:460–474.

Bloembergen, N., Purcell, E. M., Pound, R. V. (1948). Relaxation effects in nuclear magnetic resonance absorption. *Phys Rev*, **73**:679–712.

Blunck, Y., Josan, S., Taqdees, S. W., Moffat, B. A., Ordidge, R. J., Cleary, J. O., Johnston, L. A. (2017). 3D-multi-echo radial imaging of 23Na (3D-MERINA) for time-efficient multi-parameter tissue compartment mapping. *Magn Reson Med*, S. n/a–n/a.

Boada, F., Tanase, C., Davis, D., Walter, K., Torres-Trejo, A., Couce, M., Hamilton, R., Kondziolka, D., Bartynski, W., Lieberman, F. (2004). Non-invasive assessment of tumor proliferation using triple quantum filtered 23Na MRI: technical challenges and solutions. In *Engineering in Medicine and Biology Society, 2004. IEMBS'04. 26th Annual International Conference of the IEEE*, Bd. 2, S. 5238–5241. IEEE.

Boada, F. E., Gillen, J. S., Shen, G. X., Chang, S. Y., Thulborn, K. R. (1997). Fast three dimensional sodium imaging. *Magn Reson Med*, **37**(5):706–715.

Boada, F. E., LaVerde, G., Jungreis, C., Nemoto, E., Tanase, C., Hancu, I. (2005). Loss of cell ion homeostasis and cell viability in the brain: What sodium MRI can tell us. *Curr Top Dev Biol*, **70**:77 – 101.

Bouhrara, M., Reiter, D. A., Celik, H., Bonny, J.-M., Lukas, V., Fishbein, K. W., Spencer, R. G. (2015). Incorporation of Rician noise in the analysis of biexponential transverse relaxation in cartilage using a multiple gradient echo sequence at 3 and 7 Tesla. *Magn Reson Med*, **73**(1):352–366.

Breithaupt, M. (2015). *On Simulations of Spin Interactions Applied for the Volumetric T_1 Quantification by in vivo Magnetic Resonance Imaging at Ultra High Field.* Dissertation, Universität Heidelberg.

Bydder, M., Nagel, A., Maarouf, A., Verneuil, J., Viout, P., Guye, M., Ranjeva, J.-P., Zaaraoui, W. (2017). Sodium short and long T2* components in the normal human brain: a multi-TE 23Na MRI study at 7T. In *Proceedings of the ISMRM 2017*, 5631.

Coleman, T. F., Li, Y. (1994). On the convergence of interior-reflective newton methods for nonlinear minimization subject to bounds. *Math Program*, **67**(1-3):189–224.

Coleman, T. F., Li, Y. (1996). An interior trust region approach for nonlinear minimization subject to bounds. *SIAM J Optim*, **6**(2):418–445.

Constantinides, C. D., Boada, F., Bolar, D., Gillen, J., Pomper, M. G. (2000). Sodium MRI in cancer at 1.5 T. In *Proceedings of the ISMRM*, 387.

Cooley, J. W., Tukey, J. W. (1965). An algorithm for the machine calculation of complex fourier series. *Mathematics of computation*, **19**(90):297–301.

Cope, F. W. (1970). Spin-echo nuclear magnetic resonance evidence for complexing of sodium ions in muscle, brain, and kidney. *Biophys J*, **10**(9):843 – 858.

Dietrich, O., Raya, J. G., Reeder, S. B., Reiser, M. F., Schoenberg, S. O. (2007). Measurement of signal-to-noise ratios in mr images: Influence of multichannel coils, parallel imaging, and reconstruction filters. *J Magn Reson Imaging*, **26**(2):375–385.

Dula, A. N., Gochberg, D. F., Does, M. D. (2008). Optimal echo spacing for multi-echo imaging measurements of bi-exponential T(2) relaxation. *Journal of magnetic resonance (San Diego, Calif. : 1997)*, **196**(2):149–156.

Ernst, R. R., Anderson, W. A. (1966). Application of Fourier transform spectroscopy to magnetic resonance. *Rev Sci Instrum*, **37**(1):93–102.

Fessler, J. A., Sutton, B. P. (2003). Nonuniform fast fourier transforms using min-max interpolation. *IEEE Trans Signal Process*, **51**(2):560–574.

Fleysher, L., Oesingmann, N., Inglese, M. (2010). B0 inhomogeneity-insensitive triple-quantum-filtered sodium imaging using a 12-step phase-cycling scheme. *NMR Biomed*, **23**(10):1191–1198.

Fleysher, L., Oesingmann, N., Stoeckel, B., Grossman, R. I., Inglese, M. (2009). Sodium long-component T2*– mapping in human brain at 7 Tesla. *Magn Reson Med*, **62**(5):1338–1341.

Fleysher, R., Fleysher, L., Gonen, O. (2008). The optimal mr acquisition strategy for exponential decay constants estimation. *Magnetic resonance imaging*, **26**(3):433–435.

Gauss, C. F. (1809). *Theoria motus corporum coelestium in sectionibus conicis solem ambientium*. sumtibus F. Perthes et I. H. Besser.

Gilles, A. (2012). *Experimentelle Untersuchung des Relaxationsverhaltens von 23Na und 35Cl und tripelquantengefilterte In-vivo-35Cl-Magnetresonanztomografie*. Diplomarbeit, Universität Heidelberg.

Glover, F. (1998). *A template for scatter search and path relinking*, S. 1–54. Springer Berlin Heidelberg.

Gnahm, C., Bock, M., Bachert, P., Semmler, W., Behl, N. G. R., Nagel, A. M. (2014). Iterative 3D projection reconstruction of ^{23}Na data with an ^{1}H MRI constraint. *Magn Reson Med*, **71**(5):1720–1732.

Gnahm, C., Nagel, A. M. (2015). Anatomically weighted second-order total variation reconstruction of 23Na {MRI} using prior information from 1h {MRI}. *Neuroimage*, **105**:452 – 461.

Gudbjartsson, H., Patz, S. (1995). The Rician distribution of noisy MRI data. *Magn Reson Med*, **34**(6):910–914.

Gupta, R. K., Gupta, P. (1982). Direct observation of resolved resonances from intra- and extracellular sodium-23 ions in NMR studies of intact cells and tissues using dysprosium(iii)tripolyphosphate as paramagnetic shift reagent. *Journal of Magnetic Resonance (1969)*, **47**(2):344 – 350.

Gurney, P. T., Hargreaves, B. A., Nishimura, D. G. (2006). Design and analysis of a practical 3D cones trajectory. *Magn Reson Med*, **55**(3):575–582.

Haacke, E. M., Brown, R. W., Thompson, M. R., Venkatesan, R. (1999). *Magnetic Resonance Imaging: Physical Principles and Sequence Design*. J. Wiley & Sons, New York.

Hilal, S. K., Maudsley, A. A., Ra, J., Simon, H. E., Roschmann, P., Wittekoek, S., Cho, Z., Mun, S. (1985). In vivo NMR imaging of sodium-23 in the human head. *J Comput Assisted Tomogr*, **9**(1):1–7.

Hoult, D. I. (2000). The principle of reciprocity in signal strength calculations–A mathematical guide. *Concepts in Magnetic Resonance*, **12**(4):173–187.

Hubbard, P. S. (1970). Nonexponential nuclear magnetic relaxation by quadrupole interactions. *The Journal of Chemical Physics*, **53**(3):985–987.

Jaccard, G., Wimperis, S., Bodenhausen, G. (1986). Multiple-quantum NMR spectroscopy of S= 3/2 spins in isotropic phase: A new probe for multiexponential relaxation. *The Journal of chemical physics*, **85**(11):6282–6293.

Jenkinson, M., Bannister, P., Brady, J., Smith, S. (2002). Improved optimisation for the robust and accurate linear registration and motion correction of brain images. *Neuroimage*, **17(2)**:825–841.

Jenkinson, M., Smith, S. (2001). A global optimisation method for robust affine registration of brain images. *Med Image Anal*, **5(2)**:143–156.

Johnson, E. M., Pauly, K. B., Pauly, J. M. (2017). Improved short-T2* estimation with Bloch equation-modeled concurrent excitation and relaxation. In *Proceedings of the ISMRM*, 0774.

Jones, J., Hodgkinson, P., Barker, A., Hore, P. (1996). Optimal sampling strategies for the measurement of spin-spin relaxation times. *Journal of Magnetic Resonance, Series B*, **113**(1):25 – 34.

Konstandin, S., Nagel, A. (2014). Measurement techniques for magnetic resonance imaging of fast relaxing nuclei. *Magn Reson Mater Phys , Biol Med*, **27**(1):5–19.

Konstandin, S., Nagel, A. M. (2013). Performance of sampling density-weighted and postfiltered density-adapted projection reconstruction in sodium magnetic resonance imaging. *Magn Reson Med*, **69**(2):495–502.

Larsson, E. G., Erdogmus, D., Yan, R., Principe, J. C., Fitzsimmons, J. R. (2003). Snr-optimality of sum-of-squares reconstruction for phased-array magnetic resonance imaging. *Journal of Magnetic Resonance*, **163**(1):121–123.

Legendre, A. M. (1805). *Nouvelles méthodes pour la détermination des orbites des comètes*. Didot. Anhang: Sur la Méthode des moindres quarrés.

Liao, J.-R., Pauly, J. M., Brosnan, T. J., Pelc, N. J. (1997). Reduction of motion artifacts in cine MRI using variable-density spiral trajectories. *Magn Reson Med*, **37**(4):569–575.

Linnet, T. E., Teilum, K. (2016). Non-uniform sampling of NMR relaxation data. *J Biomol NMR*, **64**(2):165–173.

Lommen, J., Konstandin, S., Krämer, P., Schad, L. R. (2016a). Enhancing the quantification of tissue sodium content by MRI: time-efficient sodium B1 mapping at clinical field strengths. *NMR Biomed*, **29**(2):129–136.

Lommen, J. M., Resmer, F., Behl, N. G., Sauer, M., Benkhedah, N., Bitz, A. K., Umathum, R., Ladd, M. E., Lanz, T., , Nagel, A. M. (2016b). Comparison of a 30-channel head array with a birdcage for 23na mri at 7 tesla. In *Proceedings of the ISMRM*.

Lu, A., Atkinson, I. C., Thulborn, K. R. (2011). In vivo brain sodium T2* mapping with a multiple-echo flexible TPI sequence. In *Proceedings of the ISMRM*, 3504.

Lustig, M., Donoho, D., Pauly, J. M. (2007). Sparse MRI: The application of compressed sensing for rapid MR imaging. *Magn Reson Med*, **58**(6):1182–1195.

Ma, Y.-J., Zhu, Y., Lu, X., Carl, M., Chang, E. Y., Du, J. (2017). Short T2 imaging using a 3D double adiabatic inversion recovery prepared ultrashort echo time cones (3D DIR-UTE-Cones) sequence. *Magnetic Resonance in Medicine*, S. n/a–n/a.

Madelin, G., Chang, G., Otazo, R., Jerschow, A., Regatte, R. R. (2012). Compressed sensing sodium MRI of cartilage at 7T: Preliminary study. *J Magn Reson*, **214**:360 – 365.

Madelin, G., Kline, R., Walvick, R., Regatte, R. R. (2014). A method for estimating intracellular sodium concentration and extracellular volume fraction in brain in vivo using sodium magnetic resonance imaging. *Sci Rep*, **4**.

Madelin, G., Regatte, R. R. (2013). Biomedical applications of sodium MRI in vivo. *J Magn Reson Imaging*, **38**(3):511–529.

Matthies, C., Nagel, A. M., Schad, L. R., Bachert, P. (2010). Reduction of inhomogeneity effects in triple-quantum-filtered sodium imaging. *J Magn Reson*, **202**(2):239 – 244.

Mirkes, C. C., Hoffmann, J., Shajan, G., Pohmann, R., Scheffler, K. (2015). High-resolution quantitative sodium imaging at 9.4 Tesla. *Magn Reson Med*, **73**(1):342–351.

Monoi, H. (1976). Nuclear magnetic resonance of tissue 23Na correlation time. *Biochimica et Biophysica Acta (BBA) - General Subjects*, **451**(2):604 – 609.

Morrell, G. R. (2008). A phase-sensitive method of flip angle mapping. *Magn Reson Med*, **60**(4):889–894.

Mugler, J. P., Brookeman, J. R. (1990). Three-dimensional magnetization-prepared rapid gradient-echo imaging (3d mp rage). *Magnetic Resonance in Medicine*, **15**(1):152–157.

Müller, N., Bodenhausen, G., Ernst, R. R. (1987). Relaxation-induced violations of coherence transfer selection rules in nuclear magnetic resonance. *Journal of Magnetic Resonance (1969)*, **75**(2):297–334.

Nagel, A. M., Bock, M., Hartmann, C., Gerigk, L., Neumann, J.-O., Weber, M.-A., Bendszus, M., Radbruch, A., Wick, W., Schlemmer, H.-P., Semmler, W., Biller, A. (2011). The potential of relaxation-weighted sodium magnetic resonance imaging as demonstrated on brain tumors. *Invest Radiol*, **46**(9):539–547.

Nagel, A. M., Laun, F. B., Weber, M.-A., Matthies, C., Semmler, W., Schad, L. R. (2009). Sodium MRI using a density-adapted 3D radial acquisition technique. *Magn Reson Med*, **62**(6):1565–1573.

Nagel, A. M., Umathum, R., Rösler, M. B., Ladd, M. E., Litvak, I., Gor'kov, P. L., Brey, W. W., Schepkin, V. D. (2016). 39K and 23Na relaxation times and MRI of rat head at 21.1 T. *NMR Biomed*, **29**(6):759–766.

Narayanan, J., Xiong, J.-Y., Liu, X.-Y. (2006). Determination of agarose gel pore size: Absorbance measurements vis a vis other techniques. *Journal of Physics: Conference Series*, **28**(1):83.

Neubauer, A., Nies, C., Schepkin, V. D., Hu, R., Malzacher, M., Chacón-Caldera, J., Thiele, D., Gottwald, E., Schad, L. R. (2017). Tracking protein function with sodium multi quantum spectroscopy in a 3D-tissue culture based on microcavity arrays. *Sci Rep*, **7**.

Niesporek, S. C., Hoffmann, S. H., Berger, M. C., Benkhedah, N., Kujawa, A., Bachert, P., Nagel, A. M. (2015). Partial volume correction for in vivo 23Na-MRI data of the human brain. *Neuroimage*, **112**:353 – 363.

Niesporek, S. C., Umathum, R., Fiedler, T. M., Bachert, P., Ladd, M. E., Nagel, A. M. (2017). Improved T2* determination in 23Na, 35Cl, and 17O MRI using iterative partial volume correction based on 1H MRI segmentation. *Magn Reson Mater Phys , Biol Med*.

Nordenskiold, L., Chang, D. K., Anderson, C. F., Record, M. T. (1984). Sodium-23 NMR relaxation study of the effects of conformation and base composition on the interactions of counterions with double-helical DNA. *Biochemistry (Mosc)*, **23**(19):4309–4317.

Nyquist, H. (1928). Certain topics in telegraph transmission theory. *Transactions of the American Institute of Electrical Engineers*, **47**(2):617–644.

Papy, J.-M., De Lathauwer, L., Van Huffel, S. (2009). Exponential data fitting using multilinear algebra: the decimative case. *J Chemom*, **23**(7-8):341–351.

Payne, G. S., Styles, P. (1991). Multiple-quantum-filtered 23Na NMR spectroscopy in model systems. *Journal of Magnetic Resonance (1969)*, **95**(2):253 – 266.

Pell, G. S., Briellmann, R. S., Waites, A. B., Abbott, D. F., Lewis, D. P., Jackson, G. D. (2006). Optimized clinical T2 relaxometry with a standard CPMG sequence. *J Magn Reson Imaging*, **23**(2):248–252.

Perman, W. H., Thomasson, D. M., Bernstein, M. A., Turski, P. A. (1989). Multiple short-echo (2.5-ms) quantitation of in vivo sodium T2 relaxation. *Magn Reson Med*, **9**(2):153–160.

Pernodet, N., Maaloum, M., Tinland, B. (1997). Pore size of agarose gels by atomic force microscopy. *ELECTROPHORESIS*, **18**(1):55–58.

Poon, C. S., Henkelman, R. M. (1992). Practical T2 quantitation for clinical applications. *J Magn Reson Imaging*, **2**(5):541–553.

Qian, Y., Panigrahy, A., Laymon, C. M., Lee, V. K., Drappatz, J., Lieberman, F. S., Boada, F. E., Mountz, J. M. (2015). Short-T2 imaging for quantifying concentration of sodium (23Na) of bi-exponential T2 relaxation. *Magn Reson Med*, **74**(1):162–174.

Ra, J. B., Hilal, S. K., Cho, Z. H. (1986). A method for in vivo MR imaging of the short T2 component of sodium-23. *Magn Reson Med*, **3**(2):296–302.

Rabi, I. I., Cohen, V. W. (1934). Measurement of nuclear spin by the method of molecular beams the nuclear spin of sodium. *Phys Rev*, **46**:707–712.

Rahmer, J., Börnert, P., Groen, J., Bos, C. (2006). Three-dimensional radial ultrashort echo-time imaging with T_2 adapted sampling. *Magn Reson Med*, **55**(5):1075–1082.

Rakhmanov, E. A., Saff, E. B., Zhou, Y. M. (1994). Minimal discrete energy on the sphere. *Mathematical Research Letters*, **1**(6):647–662.

Rasche, V., Proksa, R., Sinkus, R., Bornert, P., Eggers, H. (1999). Resampling of data between arbitrary grids using convolution interpolation. *IEEE Transactions on Medical Imaging*, **18**(5):385–392.

Redfield, A. G. (1957). On the theory of relaxation processes. *IBM Journal of Research and Development*, **1**(1):19–31.

Regatte, R. R., Kaufman, J. H., Noyszewski, E. A., Reddy, R. (1999). Sodium and proton MR properties of cartilage during compression. *J Magn Reson Imaging*, **10**(6):961–967.

Robson, P. M., Grant, A. K., Madhuranthakam, A. J., Lattanzi, R., Sodickson, D. K., McKenzie, C. A. (2008). Comprehensive quantification of signal-to-noise ratio and g-factor for image-based and k-space-based parallel imaging reconstructions. *Magn Reson Med*, **60**(4):895â€“907.

Roemer, P. B., Edelstein, W. A., Hayes, C. E., Souza, S. P., Mueller, O. M. (1990). The NMR phased array. *Magn Reson Med*, **16**(2):192–225.

Rooney, W. D., Springer, C. S. (1991a). A comprehensive approach to the analysis and interpretation of the resonances of spins 3/2 from living systems. *NMR Biomed*, **4**(5):209–226.

Rooney, W. D., Springer, C. S. (1991b). The molecular environment of intracellular sodium: 23Na NMR relaxation. *NMR Biomed*, **4**(5):227–245.

Schepkin, V. D., Elumalai, M., Kitchen, J. A., Qian, C., Gorkov, P. L., Brey, W. W. (2014). In vivo chlorine and sodium MRI of rat brain at 21.1 T. *Magn Reson Mater Phys , Biol Med*, **27**(1):63–70.

Shajan, G., Mirkes, C., Buckenmaier, K., Hoffmann, J., Pohmann, R., Scheffler, K. (2016). Three-layered radio frequency coil arrangement for sodium MRI of the human brain at 9.4 Tesla. *Magnetic Resonance in Medicine*, **75**(2):906–916.

Silbernagl, S., Despopoulos, A. (2003). *Color Atlas of Physiology*. Thieme, New York.

Slichter, C. P. (1989). *Principles of Magnetic Resonance*. Springer Verlag, Berlin.

Smith, S. M. (2002). Fast robust automated brain extraction. *Hum Brain Mapp*, **17(3)**:143–155.

Stobbe, R., Beaulieu, C. (2005). In vivo sodium magnetic resonance imaging of the human brain using soft inversion recovery fluid attenuation. *Magn Reson Med*, **54**(5):1305–1310.

Stobbe, R., Beaulieu, C. (2008a). Advantage of sampling density weighted apodization over postacquisition filtering apodization for sodium MRI of the human brain. *Magn Reson Med*, **60**(4):981–986.

Stobbe, R., Beaulieu, C. (2008b). Sodium imaging optimization under specific absorption rate constraint. *Magn Reson Med*, **59**(2):345–355.

Stone, N. (2011). Table of nuclear magnetic dipole and electric quadrupole moments. *IAEA Nuclear Data Section Report INDC (NDS)-0594*.

Tanase, C., Boada, F. E. (2005). Triple-quantum-filtered imaging of sodium in presence of B_0 inhomogeneities. *J Magn Reson*, **174**(2):270–278.

Thulborn, K. R., Davis, D., Adams, H., Gindin, T., Zhou, J. (1999a). Quantitative tissue sodium concentration mapping of the growth of focal cerebral tumors with sodium magnetic resonance imaging. *Magn Reson Med*, **41**(2):351–359.

Thulborn, K. R., Gindin, T. S., Davis, D., Erb, P. (1999b). Comprehensive MR imaging protocol for stroke management: Tissue sodium concentration as a measure of tissue viability in nonhuman primate studies and in clinical studies. *Radiology*, **213**(1):156–166.

Uddin, M. N., Marc Lebel, R., Wilman, A. H. (2013). Transverse relaxometry with reduced echo train lengths via stimulated echo compensation. *Magn Reson Med*, **70**(5):1340–1346.

Ugray, Z., Lasdon, L., Plummer, J., Glover, F., Kelly, J., Martí, R. (2007). Scatter search and local NLP solvers: A multistart framework for global optimization. *INFORMS Journal on Computing*, **19**(3):328–340.

Vaughan, J. T., Hetherington, H. P., Otu, J. O., Pan, J. W., Pohost, G. M. (1994). High frequency volume coils for clinical nmr imaging and spectroscopy. *Magnetic Resonance in Medicine*, **32**(2):206–218.

Vitvitsky, V. M., Garg, S. K., Keep, R. F., Albin, R. L., Banerjee, R. (2012). Na(+) and K(+) ion imbalances in Alzheimer's disease. *Biochim Biophys Acta*, **1822**(11):1671–1681.

Volz, S., Nöth, U., Deichmann, R. (2012). Correction of systematic errors in quantitative proton density mapping. *Magn Reson Med*, **68**(1):74–85.

Walsh, D. O., Gmitro, A. F., Marcellin, M. W. (2000). Adaptive reconstruction of phased array MR imagery. *Magn Reson Med*, **43**(5):682–690.

Werbelow, L. G. (2007). *Relaxation Theory for Quadrupolar Nuclei*. John Wiley & Sons, Ltd.

Winkler, S. S., Thomasson, D. M., Sherwood, K., Perman, W. H. (1989). Regional T2 and sodium concentration estimates in the normal human brain by sodium-23 MR imaging at 1.5 T. *J Comput Assisted Tomogr*, **13**:561–6.

Winter, P. M., Bansal, N. (2001). TmDOTP5−as a 23Na shift reagent for the subcutaneously implanted 9L gliosarcoma in rats. *Magn Reson Med*, **45**(3):436–442.

Zhang, Y., Brady, M., Smith, S. (2001). Segmentation of brain MR images through a hidden Markov random field model and the expectation-maximization algorithm. *IEEE Trans Med Imag*, **20(1)**:45–57.

Zostawa, J., Adamczyk, J., Sowa, P., Adamczyk-Sowa, M. (2016). The influence of sodium on pathophysiology of multiple sclerosis. *Neurol Sci*, **38**(3):389–398.

Bibliography

List of scientific contributions

Parts of this work appear in the following conference contributions:

J.M. Lommen, S. Flassbeck, N.G.R. Behl, M.E. Ladd, A.M. Nagel. *Optimizing the Precision and Accuracy of Sampling Schemes for T2* Quantification of the Fast Biexponential Decay of Sodium MRI.* In Proceedings of the ISMRM 2017

J.M. Lommen, N.G.R. Behl, P. Bachert, M.E. Ladd, A.M. Nagel. *Realistic Simulation of 23Na Brain Data: Understanding the Influence of Acquisition Parameters on the Accuracy of 23Na Concentration Measurement.* In Proceedings of the ISMRM 2017

J.M. Lommen, F. Resmer, N.G.R. Behl, M. Sauer, N. Benkhedah, A.K. Bitz, R. Umathum, M.E. Ladd, T. Lanz, A.M. Nagel. *Comparison of a 30-channel head array with a birdcage for 23Na imaging at 7 Tesla.* In Proceedings of the ISMRM 2016. (*Magna Cum Laude Award*)

F. Resmer, J.M. Lommen, N.G.R. Behl, M. Sauer, N. Benkhedah, A.K. Bitz, R. Umathum, M.E. Ladd, A.M. Nagel, T.E. Lanz. *A 30 Channel Rx Array for 23Na Imaging of the Head at 7 Tesla.* In Proceedings of the ESMRMB 2016.

F. Resmer, J.M. Lommen, N.G.R. Behl, M. Sauer, N. Benkhedah, A.K. Bitz, R. Umathum, M.E. Ladd, A.M. Nagel, T.E. Lanz. *A 30 Channel Rx Array for 23Na Imaging of the Head at 7 Tesla.* UHF Meeting 2016, Berlin

A journal submission is currently under review:

J.M. Lommen, S. Flassbeck, N.G.R. Behl, S. Niesporek, P. Bachert, M.E. Ladd, and A.M. Nagel. *Probing the microscopic environment of 23Na ions in brain tissue by MRI – On the accuracy of different sampling schemes for the determination of rapid, biexponential T2* decay at low SNR.* Magnetic Resonance in Medicine.

Complete list of scientific contributions

Journal contributions

S.C. Niesporek, R. Umathum, J.M. Lommen, N.G.R. Behl, D. Paech, P. Bachert, M.E. Ladd, and A.M. Nagel. *Reproducibility of CMRO2 Determination using Dynamic 17O MRI.* Magnetic Resonance in Medicine (accepted).

K. Rink, N. Benkhedah, M.C. Berger, C. Gnahm, N.G.R. Behl, J.M. Lommen, V. Stahl, P. Bachert, M.E. Ladd, A.M. Nagel. *Iterative reconstruction of radially-sampled 31P bSSFP data using prior information from 1H MRI.* Magnetic Resonance in Medicine 2016.

J.M. Lommen, S. Konstandin, P. Krämer., L.R. Schad. *Enhancing the Quantification of Tissue Sodium Content by MRI – Time-Efficient Sodium B1 Mapping at Clinical Field Strengths.* NMR in Biomedicine 2015.

F.G. Zöllner, S. Konstandin, J.M. Lommen, J. Budjan, S.O. Schönberg, L.R. Schad, S. Haneder. *Quantitative Sodium MRI of Kidney.* NMR in Biomedicine 2015.

Conference contributions

J.M. Lommen, S. Flassbeck, N.G.R. Behl, M.E. Ladd, A.M. Nagel. *Optimizing the Precision and Accuracy of Sampling Schemes for T2* Quantification of the Fast Biexponential Decay of Sodium MRI.* In Proceedings of the ISMRM 2017

J.M. Lommen, N.G.R. Behl, P. Bachert, M.E. Ladd, A.M. Nagel. *Realistic Simulation of 23Na Brain Data: Understanding the Influence of Acquisition Parameters on the Accuracy of 23Na Concentration Measurement.* In Proceedings of the ISMRM 2017

W. Neumann, A. Bitz, L. Schad, F. Zöllner, M.E. Ladd, A.M. Nagel, J.M. Lommen. *Metallic Taste Perception at 7 Tesla: Influences of Jaw Position and Ionic Composition of Saliva.* In Proceedings of the ISMRM 2017 (*Magna cum Laude Award*)

S. Niesporek, R. Umathum, J.M. Lommen, A.M. Nagel. *Direct Partial Volume Corrected CMRO2 Determination: Simulation Assisted Dynamic 17O-MRI.* In Proceedings of the ISMRM 2017

J.M. Lommen, F. Resmer, N.G.R. Behl, M. Sauer, N. Benkhedah, A.K. Bitz, R. Umathum, M.E. Ladd, T. Lanz, A.M. Nagel. *Comparison of a 30-channel head array with a birdcage for 23Na imaging at 7 Tesla.* In Proceedings of the ISMRM 2016. (*Magna Cum Laude Award*)

F. Resmer, J.M. Lommen, N.G.R. Behl, M. Sauer, N. Benkhedah, A.K. Bitz, R. Umathum, M.E. Ladd, A.M. Nagel, T.E. Lanz. *A 30 Channel Rx Array for 23Na Imaging of the Head at 7 Tesla.* In Proceedings of the ESMRMB 2016.

F. Resmer, J.M. Lommen, N.G.R. Behl, M. Sauer, N. Benkhedah, A.K. Bitz, R. Umathum, M.E. Ladd, A.M. Nagel, T.E. Lanz. *A 30 Channel Rx Array for 23Na Imaging of the Head at 7 Tesla.* UHF Meeting 2016, Berlin

J.M. Lommen, S. Konstandin, and L.R. Schad. *Simultaneous B1 Mapping and Tissue Sodium Content Quantification by MRI at 3 Tesla.* In Proceedings of the ISMRM 2015.

N.K. Paschke, J.M. Lommen, L.R. Schad. *Evaluation of tissue sodium quantification accuracy in phantoms and in vivo using sodium MRI with different radiofrequency field correction methods for body stem imaging at 3T.* In Proceedings of the ESMRMB 2015.

J.M. Lommen, S. Konstandin, P. Krämer, L.R. Schad. *Evaluation of radio-frequency field mapping methods for quantitative sodium MRI at 3 Tesla.* In Proceedings of the ISMRM 2014.

List of Figures

List of Tables

Danksagung

An dieser Stelle möchte ich mich bei all denjenigen bedanken, die mich beim Gelingen dieser Arbeit unterstützt haben.

Prof. Dr. Peter Bachert möchte ich zunächst dafür danken, dass er bereit war meine Arbeit vor der Fakultät zu vertreten. Einen besonderen Dank möchte ich auch aussprechen für die zahlreichen Gutachten, die er während meiner Laufbahn geschrieben hat und dafür, dass diese immer gut genug waren um mich bis zu diesen Zeilen zu bringen.

Prof. Dr. Lothar Schad danke ich, dass er das Zweitgutachten übernommen hat.

Prof. Dr. Armin Nagel gilt mein besonderer Dank. Von der Idee auf diesem Gebiet zu promovieren bis zur Weichenstellung für die Zeit nach der Promotion hast du meine letzten Jahre maßgeblich mitbestimmt. Ich bedanke mich für das Vertrauen in meine Arbeit, dass du mich immer hast machen lassen und in schwierigen Momenten weitermotiviert hast. Du schöpfst aus einem mir unerklärlichen Reservoir immerzu Zeit und Kraft um zuzuhören und konstruktive Kritik zu geben. Danke, dass du ein Beispiel bist für ausdauernde Leistung bei genauso anhaltender Menschlichkeit!

Prof. Dr. Mark Ladd danke ich dafür, dass er mich freundlich in seine Abteilung aufgenommen und meine Promotion bis zum Schluss unterstützt hat. Danke auch für das Mitgrübeln in einem Experiment bei dem die meisten nur den Kopf geschüttelt haben.

Mein herzlicher Dank gebührt der ganzen 7T-Arbeitsgruppe für all die schönen, witzigen und unsinnigen Momente von Schneemannbildgebung bis zum Ausbruch aus rätselhaften Kerkern in Mannheim.

Mein großer Dank gebührt Nicolas Behl. Du hast mich vom Anfang meiner Promotion an als Nachbar und Unterstützer begleitet. Ich danke dir für deinen untrübbaren Optimismus, der mir durch so manche Täler geholfen hat! Danke, dass du immer Zeit und ein offenes Ohr hattest!

Sebastian Flassbeck gebührt mein herzlicher Dank für Spaß in und um Forschung herum! Ich danke dir, dass du innerhalb von 2 Sekunden den Kern oder die Lösung eines Problems finden und im folgenden Moment die Sache komplett loslassen kannst um zum Beispiel die Arbeitsumgebung kreativ weiterzuentwickeln. Weite Teile dieser Arbeit wären ohne dich so nicht realisierbar gewesen!

Für fachliche und geschmackliche Weiterentwicklung möchte ich mich bei Mathies Breithaupt bedanken. So manch spontane Serverhilfen haben sich nun bis in diese Arbeit fortgepflanzt. Auch der schottische Export freut sich weiterhin über deine Fähigkeit Menschen zu begeistern und etwas begreifbar zu machen.

Barbara Dillenberger und Christian Kindtner danke ich dafür verlässliche Konstanten in der 7T-Gruppe zu sein.

Danke an Sebastian Schmitter für das Anschaffen der Cubicals und des 7T-Mess-Servers, die beide meine Arbeitseffizienz signifikant verbessert haben.

Danke an jeden, der bei mir Proband war. Die Qualität der Bilder ist in der MRT schließlich proportional zur Wurzel aus der Ausdauer der Probanden mal deren Fähigkeit ruhig zu liegen hoch zwei.

Es gibt zahlreiche weitere Personen, die mir während meiner Promotion in verschiedenster Weise geholfen haben oder die Zeit hier am DKFZ zu etwas besonderem gemacht haben. Sobald ich anfange aufzuzählen, werde ich jemanden vergessen. Von daher danke ich an dieser Stelle jedem mit dem ich während dieser Zeit in Kontakt stand für deren besonderen Beitrag.

Marlene möchte ich an diese Stelle danken, während der Endphase der Dissertation immer ein Stern der Freude und Ausgeglichenheit gewesen zu sein.

Zuletzt möchte ich meiner Mutter danken für all die Unterstützung und liebevollen Zuspruch während des Studiums und der letzten Promotionsjahre.

Erklärung:

Ich versichere, dass ich diese Arbeit selbstständig verfasst habe und keine anderen als die angegebenen Quellen und Hilfsmittel benutzt habe.

Heidelberg, den 3.11.2017 . . . . . .